PROCEEDINGS BOOK

icame@balikesir.edu.tr
https://icame.balikesir.edu.tr
ISBN 978-975-6993-52-1



ICAMΣ'26

The 4th International Conference on Applied Mathematics in Engineering

2-4 September 2026, Cunda/Ayvalık - Türkiye



PROCEEDINGS

ICAMΣ'26

September 2-4, 2026 – Cunda Island, Ayvalık-Balikesir, TÜRKİYE

4th International Conference on Applied Mathematics in Engineering

Proceedings Book

Edited by

Prof. Dr. Ibrahim KUCUKKOC

Prof. Dr. Firat EVIRGEN

November 2026, Balıkesir

Cite articles as follows:

Author, A., Author, B. (2026). Paper Title. In I. Kucukkoc, F. Evirgen (Eds.), Proceedings of the Fourth International Conference on Applied Mathematics in Engineering (ICAME'26), Cunda Island, Ayvalık-Balikesir, Türkiye, September 2-4, Page number.

ISBN: 978-975-6993-52-1

Preface

We are pleased to have organised "The 4th International Conference on Applied Mathematics in Engineering (ICAME'26)", held on 2–4 September 2026 at Cunda Uygulama Oteli on Cunda Island, Ayvalık, Balıkesir, Türkiye. This fourth edition, following ICAME'18, ICAME'21 and ICAME'24, was organised in a hybrid format, with participants attending either on site or online.

The conference gave researchers a place to present their latest work on applied mathematics and its applications in engineering, physics, chemistry, biology and statistics, and to discuss how recent advances in the field bear on engineering and real-life problems. Topics included fractional calculus and its applications, optimization and control in engineering, mathematical modelling with engineering applications, operational research, nonlinear dynamical systems and chaos, stochastic modelling, artificial intelligence in engineering, energy systems modelling and sustainable computing. A total of 133 papers were presented in parallel sessions, held in two onsite halls and three online rooms, by 259 authors and co-authors from 34 countries. More than 150 participants registered for the conference.

Authors of selected high-quality presentations were invited to submit substantially extended versions of their papers to special issues of *Engineering Applications of Artificial Intelligence (Elsevier), Sustainable Computing: Informatics and Systems (Elsevier), An International Journal of Optimization and Control: Theories & Applications (IJOCTA), Jambura Journal of Biomathematics, Bulletin of Biomathematics and Celal Bayar University Journal of Science*, as well as to an international contributed book volume.

This book contains the full-text versions of 14 papers presented at ICAME'26 that were not submitted to the journal special issues. All submissions were peer reviewed in a single-blind process, and the book editors made the final decision on publication.

We would like to thank our plenary speakers *Young Im Cho (Gachon University, Republic of Korea), Dumitru Baleanu (Lebanese American University, Lebanon), Hüseyin Şeker (University of Sharjah, UAE), Maíra Aguiar (Basque Center for Applied Mathematics, Spain), Gerhard-Wilhelm Weber (Poznan University of Technology, Poland) and Jordan Hristov (University of Chemical Technology and Metallurgy, Bulgaria)*. Our thanks also go to the organisers of the special sessions, the authors, and the members of the international scientific committee and the organising committee for their cooperation. We are grateful to *Balıkesir University, Ayvalık Municipality, KZ Mekatronik and Özgün Zeytincilik for their support, and to Elsevier, Springer and AIMS* for their cooperation.

We hope to see you all at the next ICAME conference.

November 2026

Book Editors

Prof. Dr. Ibrahim Kucukkoc
Department of Industrial Engineering
Balikesir University, Türkiye

Prof. Dr. Firat Evirgen
Department of Mathematics
Balikesir University, Türkiye

Committee

Chairs

Dumitru Baleanu, Lebanese American University, Lebanon
Ramazan Yaman, Balikesir University, Turkiye
Jordan Hristov, Univ. of Chemical Tech. and Metallurgy, Bulgaria
Necati Ozdemir, Balikesir University, Turkiye

International Scientific Committee

Abdeljawad, T., Saudi Arabia
Agarwal, P., India
Ahmad, I., Saudi Arabia
Akin, O., Turkiye
Area, I., Spain
Atanackovic, T., Serbia
Atangana, A., South Africa
Ayaz, F., Turkiye
Bagirov, A., Australia
Baskonus, H.M., Turkiye
Baleanu, D., Lebanon
Cho, Y.I., S. Korea
Caputo, M., Italy
Cattani, C., Italy
Dassios, I., Ireland
Debbouche, A., Algeria
Defterli, O., Turkiye
El-Khazali, R., United Arab Emirates
El-Sayed, A., Egypt
Erturk, V.S., Turkiye
Golmankhaneh, A.K., Iran
Gulsu, M., Turkiye
Gurbuz, B., Germany
Holm, S., Norway
Hristov, J., Bulgaria
Jafari, H., South Africa
Jarad, F., Turkiye
Kaya, D., Turkiye
Kazmi, I., Pakistan
Keedwell, E.C., UK
Klimek, M. Poland
Konuralp, A., Turkiye
Kumar, D., India
Leblebicioglu, K., Turkiye
Li, C.P.,China
Liu, F., Australia
Luo, A.C.J, USA
Magin, R. L., USA
Marin, M., Romania
Mandzuka, S., Crotia
Markowski, K.A., Poland
Merdan, H., Turkiye
Momani, S., Jordan
Nigmatullin, R. R., Russia
Ozcan, E., UK
Peron, M., France
Pinto, C.M., Portugal
Podlubny, I., Slovakia
Povstenko, Y., Poland
Prodanov, D., Belgium
Sari, M., Turkiye
Seker, H., UAE & UK
Shams, M., Turkiye
Sing, J., India
Sproessig, W., Germany
Sulaiman, S., Malaysia
Tabucanon, M.T., Thailand
Tarasov, V.E., Russia
Thuto, M.V., Botswana
Torres, D.F.M., Portugal
Townley, S., UK
Trujillo, J.J., Spain
Weber, G.W., Poland
Wu, G.C., China
Yang, X.J., China
Zhang, D.Z., UK

Organizing Committee

Ramazan Yaman, Turkiye
Dumitru Baleanu, Lebanon
Necati Ozdemir, Turkiye
Firat Evirgen, Turkiye
Gerhard Wilhelm Weber, Poland
Ibrahim Kucukkoc, Turkiye
Burcu Gurbuz, Germany
Mehmet Yavuz, Turkiye
Yeliz Karaca, USA

Programme Committee

Ramazan Yaman, Balikesir University, Turkiye
Necati Ozdemir, Balikesir University, Turkiye
Firat Evirgen, Balikesir University, Turkiye
Ibrahim Kucukkoc, Balikesir University, Turkiye

Local Organizing Committee

Akdemir, M., Turkiye
Calgan, H., Turkiye
Demir, T., Turkiye
Demirtas, M., Turkiye
Gökkaya, H., Turkiye
Gucu, S, Turkiye
Inan, D., Turkiye
Karaoglan, A.D., Turkiye
Yaman, G., Turkiye
Yildirim, H.H., Turkiye
Yilmaz, T., Turkiye

ICAME'26 - CONFERENCE PROGRAMME OUTLINE (https://icame.balikesir.edu.tr)					
Day 1: Wednesday, 2 September 2026		**Day 2: Thursday, 3 September 2026**		**Day 3: Friday, 4 September 2026**	
09:00-10:00	**Registration**	09:00-09:30	**Registration**	09:00-09:30	**Registration**
10:00-10:30	**Opening Ceremony (Hall-1)** *Conference Chairs*	09:30-10:10	**Plenary Lecture-4 (Hall-1) Dumitru Baleanu**	09:00-10:40	**Parallel Sessions - 6** *09:00-09:20* *09:20-09:40* *09:40-10:00* *10:00-10:20* *10:20-10:40*
10:30-11:10	**Plenary Lecture-1 (Hall-1) Hüseyin Şeker**	*10:15-10:35*	*Coffee Break*		
11:15-11:35	*Coffee Break*	10:35-12:15	**Parallel Sessions - 4** *10:35-10:55* *10:55-11:15* *11:15-11:35* *11:35-11:55* *11:55-12:15*	10:45-11:25	**Plenary Lecture-5 (Hall-1) Praveen Agarwal *[online]***
11:35-12:15	**Plenary Lecture-2 (Hall-1) Young Im Cho *[online]***			11:30-11:50	**Closing Ceremony (Hall-1)**
12:15-13:25	***LUNCH***	*12:15-13:25*	***LUNCH***	12:00	**Social Tour** **(Ayvalık-Cunda)**
13:30-15:10	**Parallel Sessions - 1** *13:30-13:50* *13:50-14:10* *14:10-14:30* *14:30-14:50* *14:50-15:10*	13:35-14:15	**Plenary Lecture-5 (Hall-1) Maíra Aguiar [online]**		
		14:25-15:05	**Plenary Lecture-6 (Hall-1) Gerhard Wilhelm Weber [online]**		
15:15-15:55	**Plenary Lecture-3 (Hall-1) Jordan Hristov**	*15:05-15:25*	*Coffee Break*		
15:55-16:15	*Coffee Break*	15:30-17:10	**Parallel Sessions - 5** *15:30-15:50* *15:50-16:10* *16:10-16:30* *16:30-16:50* *16:50-17:10*		
16:15-17:35	**Parallel Sessions - 2** 16:15-16:35 16:35-16:55 16:55-17:15 17:15-17:35				
17:35-17:50	*Coffee Break*	*17:10-17:30*	*Coffee Break*		
17:50-19:30	**Parallel Sessions - 3** 17:50-18:10 18:10-18:30 18:30-18:50 18:50-19:10 *19:10-19:30*	17:30-18:15	**Round-table Discussion** *(Hall-1)*		
19:30	***DINNER***	*19:30*	***DINNER***		

Contents

Preface **3**

Committee **4**

Contents **7**

Physics-Informed Neural Networks for Periodic Sturm–Liouville Eigenvalue Problems 8

Advanced Qualitative and Sensitivity Analysis of Deterministic Lanchester-Type Area-Fire Warfare Models 14

Comparing Fuzzy Synergy Encodings in Robust R&D Project Portfolio Selection and Core-Constrained Cost Allocation 20

Rich, Green and Safety Focused Route Optimization 26

Application of E-Bayesian Estimation to the Rayleigh Distribution in Wind Energy 34

Effect of Viscous Dissipation on Pulsating Flow and Heat Transfer for Non-Newtonian Fluid in a Pipe 41

Solutions of 3D MHD Equations using Different Variants of Differential Quadrature Method 49

Temporal Memory Estimation for Multi-Horizon HVAC Load Forecasting 56

Spatial Heterogeneity in Provincial Housing Sales in Türkiye: A Comparative Analysis of OLS, SAR, SEM, and GWR Models 63

QoS-Aware Opportunistic Routing in Wireless Mesh Networks: An Integration-Centric Taxonomy and Mathematical Modeling Perspective 70

Cardinality-Constrained Risk Parity on a Sharpe-Filtered Subset of the BIST-100 Index 78

Mixed Sumudu–Adomian Method for Two-Dimensional Nonlinear Fuzzy Integral Equations 84

Genetic Algorithm and Particle Swarm Optimization for Mass Minimization of a Composite Cylindrical Skirt under Buckling and Strength Constraints 93

Author Index **99**

Physics-Informed Neural Networks for Periodic Sturm–Liouville Eigenvalue Problems

Seza Dinibutun*

Department of Mathematics and Natural Sciences, International University of Science and Technology in Kuwait, Ardiya 92400, Kuwait
seza.dinibutun@iuk.edu.kw

Abstract

This study uses a physics-informed neural network (PINN) to solve a periodic Sturm–Liouville eigenvalue problem with the nonconstant potential $q(x) = 2\cos(2x)$. The network approximates the unknown eigenfunction, while the eigenvalue is trained as a separate scalar parameter. Automatic differentiation provides the first and second derivatives needed to calculate the differential-equation residual. The loss function also enforces the periodic boundary conditions and a discrete mean-square normalization, which prevents convergence to the zero function. The model has three hidden layers with 20 neurons in each layer and was trained at 100 uniformly spaced collocation points using Adam for 6000 epochs. The eigenvalue was initialized at 2.0, and the final estimate was approximately 1.85894656. Compared with the Mathieu reference value of 1.859108072514363, the relative error was approximately 8.69×10^{-5}. The computed eigenfunction is smooth and periodic. This calculation shows that the PINN can recover one low-order periodic eigenpair without labeled eigenfunction data.

Keywords: Physics-informed neural network, PINN, Sturm–Liouville problem, periodic boundary conditions, eigenvalue problem

1. Introduction

Periodic Sturm–Liouville problems arise when separation of variables is applied to differential equations with periodic coefficients or boundary conditions. Their eigenvalues and eigenfunctions appear in vibration and stability analysis, heat and wave problems, quantum mechanics, and the study of periodic media. Over one period, both the function and its derivative must have matching values at the endpoints (Eastham, 1973).

Several numerical methods are available for these problems, including shooting, finite differences, finite elements, and spectral methods. Most of these methods replace the continuous problem with a matrix eigenvalue problem constructed on a mesh or basis. Andrew (1989) studied correction formulas for finite-difference eigenvalues under periodic boundary conditions. Dinibutun and Veliev (2013) derived estimates for small periodic and semiperiodic eigenvalues, while Dinibutun (2021) used a finite-difference method to approximate periodic eigenfunctions.

Neural networks provide another way to approximate solutions of differential equations. Lagaris et al. (1998) trained neural networks by minimizing errors associated with the differential equation and its conditions. In physics-informed neural networks, automatic differentiation is used to calculate the derivatives of the network output, and the differential equation becomes part of the training loss (Raissi et al., 2019; Karniadakis et al., 2021). For eigenvalue problems, Jin et al. (2020) presented an unsupervised neural-network method for finding quantum eigenpairs. Their later PINN formulation included normalization, orthogonality, and symmetry information for computing quantum eigenstates (Jin et al., 2022). More recently, Zhang et al. (2024) proposed an unsupervised deep-learning method

* *Corresponding Author*

for finding eigenpairs of Sturm–Liouville problems. Bi et al. (2025) introduced a PINN formulation for neutron-diffusion eigenvalue problems with interface conditions.

In the present study, the neural network approximates a periodic eigenfunction, and the eigenvalue is trained together with the network parameters. No known eigenfunction values are supplied during training. The computed eigenvalue is compared with a Mathieu characteristic value and independently checked using periodic finite differences. Since the calculation starts from $\lambda = 2.0$ and does not search for the eigenvalues in a prescribed order, the reported result is described as one low-order periodic eigenpair rather than the lowest eigenvalue.

2. Problem Definition

Consider the periodic Sturm–Liouville problem on the interval $[0, 2\pi]$. The unknowns are a nonzero function $y(x)$ and a scalar eigenvalue λ satisfying

$$-y''(x) + q(x)y(x) = \lambda y(x),\ q(x) = 2\cos(2x), \quad 0 \le x \le 2\pi \tag{1}$$

together with the periodic endpoint conditions

$$y(0) = y(2\pi), \quad y'(0) = y'(2\pi). \tag{2}$$

The first boundary condition matches the function values at the endpoints, while the second matches their slopes. We chose $q(x) = 2\cos(2x)$ because it is smooth, periodic, and nonconstant. With this potential, equation (1) is a Mathieu-type equation. It is more interesting than the case $q(x) = 0$, whose solutions reduce to elementary sine and cosine functions, but it is still simple enough for comparison with a classical numerical calculation. A nonzero periodic solution exists only for particular values of λ.

3. Proposed Method

The unknown eigenfunction is approximated by a fully connected neural network $y_\theta(x)$, where θ represents its weights and biases. The network has one input x, three hidden layers with 20 neurons in each layer, and one output. The tanh activation function is applied after each hidden layer, while the output layer is linear. Tanh was selected because it is smooth and allows the first and second derivatives required by equation (1) to be calculated.

The network contains 901 weights and biases. One additional unconstrained scalar parameter α is trained, and the eigenvalue is defined as $\lambda = |\alpha|$. Therefore, the optimization includes 902 trainable quantities in total.

At each collocation point x_i, automatic differentiation is used to calculate $y'_\theta(x_i)$ and $y''_\theta(x_i)$. Substitution into the differential equation gives the residual

$$r(x_i) = -y_\theta''(x_i) + q(x_i)y_\theta(x_i) - |\alpha| y_\theta(x_i). \tag{3}$$

For $N = 100$ uniformly spaced points, including both endpoints of $[0, 2\pi]$, the differential-equation loss is the mean squared residual

$$L_{DE} = \frac{1}{N}\sum_{i=1}^{N} r(x_i)^2. \tag{4}$$

The periodic boundary conditions are included through

$$L_{BC} = [y_\theta(0) - y_\theta(2\pi)]^2 + [y'_\theta(0) - y'_\theta(2\pi)]^2. \tag{5}$$

Because the eigenvalue equation is homogeneous, the zero function would satisfy both the differential equation and the boundary conditions for any value of λ. A discrete mean-square normalization is therefore included to prevent the network from converging to this trivial solution:

$$L_{NORM} = \left[\frac{1}{N}\sum_{i=1}^{N} y_\theta(x_i)^2 - 1\right]^2. \quad (6)$$

This condition fixes the mean squared value of the function at the collocation points. It should not be interpreted as continuous L^2 normalization. The total loss used in the code is

$$L = L_{DE} + 10L_{BC} + 10L_{NORM}. \quad (7)$$

Adam jointly updates the network parameters θ and the scalar parameter α. The eigenvalue is represented by $\lambda = |\alpha|$ throughout the loss calculation, restricting the implementation to nonnegative eigenvalues. Training started from $\lambda = 2.0$ and used a learning rate of 0.001 for 6000 epochs. All 100 collocation points were used in every epoch. The random seed was set to zero so that the initial network parameters could be reproduced. Table 1 lists the main implementation settings.

Table 1. PINN architecture and training settings

Parameter	Value	Parameter	Value
Domain	[0, 2π]	Collocation points	100 uniform points
Hidden layers	3	Neurons per layer	20
Activation	tanh	Trainable quantities	902
Initial λ	2.0	Optimizer	Adam
Learning rate	0.001	Epochs	6000
Loss weights	1 : 10 : 10	Random seed	0

Equation (1) can be written as the Mathieu equation $y'' + [\lambda - 2\cos(2x)]y = 0$. The reference for the reported eigenmode was evaluated using the Mathieu characteristic value $a_1(1)$, obtained with SciPy's scipy.special.mathieu_a(1, 1). This gives $\lambda_{\text{ref}} \approx 1.859108072514363$.
An independent check used a second-order central finite-difference discretization on M uniformly spaced points $x_j = jh$, where $h = 2\pi/M$ and $j = 0, \ldots, M-1$. The second derivative was approximated by $(y_{j+1} - 2y_j + y_{j-1})/h^2$, with indices interpreted periodically. The endpoint 2π was therefore not duplicated. The resulting symmetric matrix eigenvalue problem was solved for the eigenvalue near 1.86. Grid refinement was performed using $M = 100, 200, 400, 800, 1600$, and 3200.

4. Results and Discussion

Training starts with $\lambda = 2.0$ and a randomly initialized network function. Figure 1(a) shows that the estimated eigenvalue first decreases to approximately 1.21 and then increases toward a stable value. This path is not monotonic because the network function and the eigenvalue are changing at the same time. A value of λ that reduces the residual at an early stage may no longer be suitable after the shape of the network function changes. After approximately 4000 epochs, the estimate remains close to 1.8591.

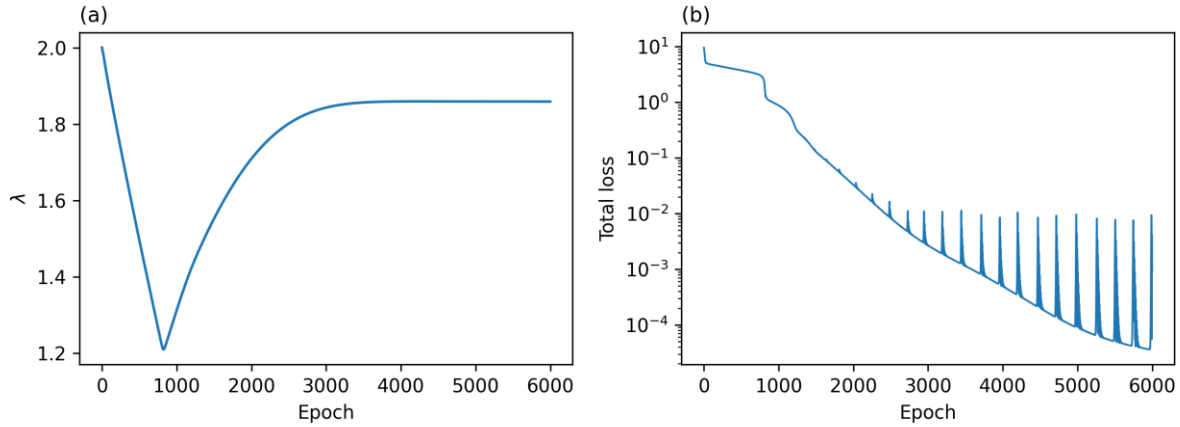


Figure 1. Training histories: (a) learned eigenvalue and (b) total loss on a logarithmic scale.

Figure 1(b) shows that the total loss decreases by several orders of magnitude during training, with some fluctuations during the later epochs. After 6000 Adam updates, the final eigenvalue was approximately 1.85894656. Compared with the Mathieu reference value of 1.859108072514363, the absolute error was 1.6151×10^{-4} and the relative error was 8.6875×10^{-5}, corresponding to approximately 0.00869%.

The computed eigenfunction was checked at 1000 uniformly spaced midpoint locations that were separate from the training points. Using the network output without additional rescaling, the differential-equation residual had a root mean square of 5.6695×10^{-3} and a maximum absolute value of 2.1764×10^{-2}. The absolute differences between the endpoint function values and endpoint derivatives were 2.6309×10^{-4} and 2.1280×10^{-4}, respectively. The discrete mean squared value at the training points was 0.999875, close to the normalization target of 1. These checks provide numerical evidence that the differential equation and periodic boundary conditions are approximately satisfied.

The finite-difference eigenvalues approached the Mathieu reference as the grid was refined. For $M = 800,1600,$ and 3200, the estimates were 1.859094810761, 1.859104757133, and 1.859107243687, respectively. Their absolute errors were approximately 1.33×10^{-5}, 3.32×10^{-6}, and 8.29×10^{-7}. The error decreased by approximately a factor of four when the grid spacing was halved, consistent with the second-order discretization. The additional digits quoted for the reference value come from the Mathieu-function calculation.

Figure 2 shows the learned eigenfunction at 500 evaluation locations on the interval $[0, 2\pi]$. These locations were used to produce a smooth plot, while training used 100 collocation points. The horizontal axis represents the physical coordinate x. The network output is plotted directly, without additional rescaling. Its amplitude is determined by the discrete mean-square normalization included in the training loss. The sign of an eigenfunction is not unique, since multiplying it by -1 gives the same eigenmode.

The method does not recover the complete ordered spectrum. The result is one low-order periodic eigenpair. The absolute-value parameterization prevents the model from finding negative eigenvalues, and a different initial value of λ may lead to a different eigenmode. Computing several modes would require an additional procedure for selecting or separating them, together with tests using different initial values.

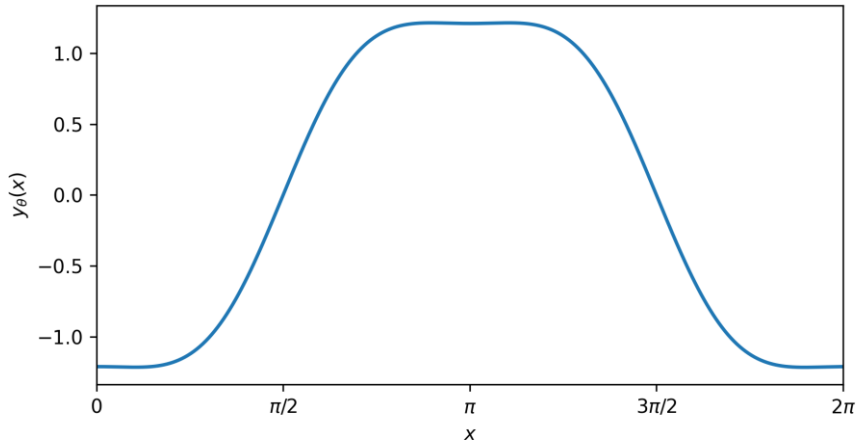


Figure 2. Learned periodic eigenfunction evaluated at 500 locations on [0, 2π], plotted against the physical coordinate x without additional rescaling.

The network size, number of collocation points, loss weights, and number of epochs were kept fixed in this experiment. A sensitivity analysis was not performed. For this one-dimensional example, a classical eigensolver remains simpler and provides an independent numerical check. The PINN is considered here as an alternative formulation in which the eigenfunction and eigenvalue are learned together from the differential equation and boundary conditions.

5. Conclusions

This study applied a physics-informed neural network to a periodic Sturm–Liouville problem with $q(x) = 2\cos(2x)$. The network approximated the eigenfunction, while the eigenvalue was trained as an additional scalar parameter. The loss included the differential-equation residual, the periodic boundary conditions, and a discrete normalization condition. Therefore, no labeled eigenfunction values were required during training.

Using three hidden layers with 20 neurons each, 100 collocation points, and 6000 Adam updates, the model produced a smooth periodic eigenfunction and an eigenvalue of approximately 1.85894656. The relative error compared with the Mathieu reference was approximately 8.69×10^{-5}. Residual checks at separate evaluation points and small endpoint value and derivative differences provided further numerical verification of the computed solution.

The current implementation finds one eigenpair with a nonnegative eigenvalue near the initial value of λ; it does not compute the complete spectrum. Future work will remove the nonnegative restriction on λ and investigate reliable methods for separating different eigenmodes. The effects of network size, collocation points, loss weights, and initialization should also be examined. Comparisons with finite-difference, finite-element, and spectral methods will help determine the types of periodic eigenvalue problems for which a PINN is most useful.

References

Andrew, A. L. (1989). Correction of finite difference eigenvalues of periodic Sturm–Liouville problems. Journal of the Australian Mathematical Society. Series B. Applied Mathematics, 30(4), 460–469. https://doi.org/10.1017/S0334270000006391

Bi, H., Song, M., Zhang, T., & Liu, X. (2025). FC-PINNs: Physics-informed neural networks for solving neutron diffusion eigenvalue problem with interface considerations. Journal of Computational Physics, 541, 114311. https://doi.org/10.1016/j.jcp.2025.114311

Dinibutun, S. (2021). An estimation of the eigenfunctions of periodic Sturm–Liouville problems. Arab Journal of Basic and Applied Sciences, 28(1), 107–112. https://doi.org/10.1080/25765299.2021.1905345

Dinibutun, S., & Veliev, O. A. (2013). On the estimations of the small periodic eigenvalues. Abstract and Applied Analysis, 2013, Article 145967. https://doi.org/10.1155/2013/145967

Eastham, M. S. P. (1973). The spectral theory of periodic differential equations. Scottish Academic Press.

Jin, H., Mattheakis, M., & Protopapas, P. (2020). Unsupervised neural networks for quantum eigenvalue problems. arXiv. https://doi.org/10.48550/arXiv.2010.05075

Jin, H., Mattheakis, M., & Protopapas, P. (2022). Physics-informed neural networks for quantum eigenvalue problems. arXiv. https://doi.org/10.48550/arXiv.2203.00451

Karniadakis, G. E., Kevrekidis, I. G., Lu, L., Perdikaris, P., Wang, S., & Yang, L. (2021). Physics-informed machine learning. Nature Reviews Physics, 3, 422–440. https://doi.org/10.1038/s42254-021-00314-5

Lagaris, I. E., Likas, A., & Fotiadis, D. I. (1998). Artificial neural networks for solving ordinary and partial differential equations. IEEE Transactions on Neural Networks, 9(5), 987–1000. https://doi.org/10.1109/72.712178

Raissi, M., Perdikaris, P., & Karniadakis, G. E. (2019). Physics-informed neural networks: A deep learning framework for solving forward and inverse problems involving nonlinear partial differential equations. Journal of Computational Physics, 378, 686–707. https://doi.org/10.1016/j.jcp.2018.10.045

Zhang, S., Zu, J., & Zhang, J. (2024). Deep learning method for finding eigenpairs in Sturm–Liouville eigenvalue problems. Electronic Journal of Differential Equations, 2024(53), 1–17. https://doi.org/10.58997/ejde.2024.53

Advanced Qualitative and Sensitivity Analysis of Deterministic Lanchester-Type Area-Fire Warfare Models

Ioannis D. Sfikas *

National Technical University of Athens, School of Applied Mathematics & Physical Sciences, Greece
sfikas@hotmail.com

Abstract

This paper presents a rigorous mathematical investigation into the qualitative behavior and parameter estimation framework of the deterministic Lanchester area-fire warfare model. Representing a non-isolated, nonlinear dynamical system, the area-fire model possesses a unique geometric structure where the equilibrium states form a continuous one-dimensional manifold along the coordinate axes rather than isolated points. Due to this inherent non-hyperbolicity and the presence of a zero eigenvalue, classical linearization techniques and the Hartman-Grobman theorem are insufficient to fully characterize the system's asymptotic behavior. To resolve this, we employ invariant manifold theory alongside LaSalle's Invariance Principle, constructing a strict linear Lyapunov function based on the weighted combat capabilities of the opposing forces. This approach rigorously proves the global asymptotic convergence of all admissible trajectories toward the equilibrium manifold, ensuring that military resource dissipation is irreversible and that self-sustained oscillations or limit cycles are structurally impossible. Furthermore, we address the challenge of data-driven parameter identification, which is critical for operational planning and historical battle reconstructions. We formulate a nonlinear inverse problem utilizing a least-squares optimization functional to estimate the combat effectiveness coefficients from discrete battlefield observations. To evaluate the robustness of these estimators, a six-dimensional augmented forward sensitivity system is derived by differentiating the governing state equations using the product and chain rules. Local parameter perturbations reveal a mathematical singularity in relative sensitivity when the forces reach a tactical stalemate, matching real-world military operational experiences where minor non-numerical factors can entirely invert the engagement outcome. Finally, codimension-one bifurcation analysis demonstrates that the spectral properties and topological structure of the phase portrait remain invariant under positive parameter perturbations, establishing the robust structural stability of the model within the admissible positive parameter space.

Keywords: Lanchester equations, nonlinear dynamical systems, invariant manifolds, Lyapunov stability, forward sensitivity equations, bifurcation theory

1. Introduction

The strategy and tactics of opponents constitute the two primary characteristic elements of general combat. Strategy is typically designed to achieve the long-term attrition or exhaustion of the enemy, whereas tactics refer to specific, localized operational approaches aimed at securing immediate objectives that serve the overarching strategic vision. The deterministic mathematical modeling of a battle between heterogeneous forces evaluates attrition rates as real functions of both weapon characteristics and the volume of fire directed at the opposing force. However, classical Lanchester-type formulations alone cannot capture spatial dynamics, such as the physical movement of engaged forces (Ancker, 1995).

* *Corresponding Author*

Geographical location influences the evolution and terminal state of any competitive struggle, whether an entity is engaging in warfare, executing a marketing campaign, or designing public health vaccination programs. Consequently, the capacity to model distinct spatial settings in a consistent and stable manner is crucial when adopting an army strategy (González & Villena, 2011). Heterogeneous forces exhibit distinct attrition rates determined by the specific types of weapon systems deployed, the nature of the enemy targets, and various environmental or operational factors (Lanchester 1914, 1916).

Frederick Lanchester (1868-1946) was a pioneer in the mathematical formalization of combat theory. Modern applications of Lanchester's core ideas to land combat often encounter the challenge that each side comprises multiple types of combat elements, each interacting differently with the opposing forces' various units. There have been numerous attempts to compare historical combat data with the behavior expected from Lanchester's equations, including the landmark empirical studies of Helmbold and Hartley (Hartley, 1995; Hartley & Helmbold, 1995). Hartley (1995) provided a comprehensive review of these historical efforts to validate combat attrition laws through empirical analysis. Beyond deterministic frameworks, alternative scholarly efforts have investigated the distribution of casualties by modeling combat attrition as stochastic processes (Wiper et al. 2000).

In basic Lanchester-type models, highly restrictive operational assumptions are usually enforced (Dolanský, 1964). However, these are not the sole conditions under which such attrition laws can be derived. For instance, Brackney (1959) demonstrated that when the combat area is dynamically varied so that the force density remains constant, attrition rates of the square-law type naturally emerge. Conversely, Helmbold (1964) argued that victory in battle is primarily dictated by qualitative factors rather than mere numerical superiority, challenging the capacity of any pure attrition model to serve as a practically useful operational predictor. Willard (1962, 1990) reached similar conclusions, introducing additional theoretical expansions on variable attrition rates. Because differential equations do not inherently contain explicit information about the spatial distribution or real-time maneuvers of armies, the direct relevance of traditional differential models to modern multi-domain warfare remains a subject of ongoing discussion (Ancker, 1995; Willard, 1990).

2. Problem Definition

Suppose that a Red army and a Blue army engage each other in combat. Both sides deploy area fire, and target acquisition times remain constant, independent of the overall force levels. These two forces possess a continuous density of weapons units denoted by $M = M(t)$ and $K = K(t)$, respectively, as a function of time $t \geq 0$. Under the area-fire assumption, the attrition rate of each side is proportional to the product of both army populations, following the historical baseline formulations (Israel, 1995; Lanchester, 1914, 1916):

$$\frac{dK_t}{dt} = -\mu M(t)K(t), \qquad \frac{dM(t)}{dt} = -\kappa M(t)K(t), \tag{1}$$

where κ and μ correspond to the strictly positive attrition rate coefficients of the armies $M(t)$ and $K(t)$, respectively. The equilibrium conditions between the two armies depend entirely on the initial parameters and obey the classical principle of mass action (Epstein, 1997; Helmbold, 1993). By integrating the area-fire governing equations (1), we obtain Lanchester's linear law:

$$\frac{K_0 - K(t)}{M_0 - M(t)} = \frac{\mu}{\kappa}, \tag{2}$$

for all $t \geq 0$, where $K_0 = K(0) \geq 0$ and $M_0 = M(0) \geq 0$ constitute the initial force levels. If the combat results in a mutual tactical stalemate where neither force secures a victory, the populations

asymptotically satisfy $M(t) \to 0$ and $K(t) \to 0$ as $t \to \infty$. This yields the exact mathematical stalemate boundary condition:

$$\Delta = \kappa K_0 - \mu M_0 = -\mu\left(M_0 - \frac{\kappa}{\mu}K_0\right) = 0. \tag{3}$$

3. Proposed Method

To fully characterize the system's asymptotic behavior and resolve the challenges of non-hyperbolicity induced by the presence of a zero eigenvalue, we employ invariant manifold theory alongside LaSalle's Invariance Principle. We construct a strict linear Lyapunov function based on the weighted combat capabilities of the opposing forces:

$$V(K, M) = \kappa K + \mu M. \tag{4}$$

Differentiating V along the system trajectories yields:

$$\dot{V} = -2\mu\kappa MK \leq 0. \tag{5}$$

Since $V(K, M)$ is bounded below by zero in the first quadrant and is non-increasing along trajectories ($\dot{V} \leq 0$), LaSalle's Invariance Principle ensures that every admissible solution trajectory converges asymptotically to the largest invariant subset contained within the region where $\dot{V} = 0$. This region corresponds exactly to the non-hyperbolic equilibrium manifold:

$$E = \{(K, M) \in \mathbb{R}_+^2 | (K \geq 0, M = 0) \cup (K = 0, M \geq 0)\}. \tag{6}$$

This mathematical framework provides an exact geometric decomposition of the state space without requiring Taylor expansions, asymptotic approximations, or Center Manifold Reduction techniques (Britton et al., 1996; Daras, 2012; Sheeba & Ghose, 2008; Taylor, 1983).

4. Results and Discussion

4.1. Phase Portrait Analysis and Geometry

Theorem 4.1. The trajectories of the Lanchester area-fire model form a family of parallel straight lines in the phase plane.

Proof. Eliminating the time variable t from the system equations yields the differential relationship $\frac{dM}{dK} = \frac{\kappa}{\mu}$. Direct integration with respect to K gives $M = \frac{\kappa}{\mu}K + c$, where the integration constant is uniquely determined by the initial states as $c = M(0) - \frac{\kappa}{\mu}K(0)$. □

Because $K(t)$ and $M(t)$ are strictly non-negative physical quantities, every valid trajectory evolves monotonically from the north-east toward the south-west direction of the phase plane. Since $K(t)$ is strictly decreasing whenever $M(t) > 0$, the state variables cannot return to any previously occupied value, confirming the absolute absence of closed orbits or self-sustained periodic oscillations. Furthermore, the divergence of the vector field $F(K, M)$ is given by $\nabla \cdot F = -\mu M - \kappa K$, which is strictly negative ($\nabla \cdot F < 0$) in the interior of the first quadrant. Consequently, the Bendixson-Dulac criterion rigorously excludes the existence of limit cycles anywhere within the admissible state space.

4.2. Sensitivity Analysis and Singularity

Differentiating the conserved invariant quantity $I(K,M) = \kappa K - \mu M$ yields the state sensitivities with respect to the parameters: $\frac{\partial I}{\partial \mu} = -M$ and $\frac{\partial I}{\partial \kappa} = K$. This implies that the structural influence of parameter uncertainty is maximal during the early phases of combat and monotonically diminishes as the forces undergo attrition. To formalize this relatively, we examine the dimensionless relative sensitivity index of the invariant I with respect to the attrition parameter μ:

$$\Sigma_\mu = \frac{\mu}{I}\frac{\partial I}{\partial \mu} = -\frac{\mu M}{\kappa K - \mu M}. \tag{7}$$

Proposition 4.1. The relative sensitivity index Σ_μ exhibits a mathematical singularity ($\Sigma_\mu \to \pm\infty$) as the system approaches the state threshold where $\kappa K = \mu M$.

Crucial interpretative distinction: It is critical to distinguish between state sensitivity and relative sensitivity at this threshold. The underlying state sensitivities ($\frac{\partial I}{\partial \mu} = -M$) remain perfectly bounded, smooth, and well-behaved. The singularity observed in Σ_μ is purely a mathematical artifact introduced by the zero denominator of the relative index since $I = \kappa K - \mu M = 0$ exactly at the stalemate boundary.

Operationally, however, this relative singularity possesses substantial physical meaning: it corresponds precisely to a perfect tactical stalemate (the bifurcation-like boundary separating a Red victory from a Blue victory). In this critical state, the deterministic macroscopic trajectory is perfectly balanced, meaning that minor, unmodeled non-numerical factors (such as variations in training, micro-logistics, or command efficiency) can completely invert the combat outcome.

4.3. Parameter Identification Framework

We formulate a nonlinear inverse problem utilizing a least-squares optimization functional to extract the true parameter vector $\theta = (\mu, \kappa)^T$ from a set of discrete, noisy battlefield observations $\{K_i^{obs}, M_i^{obs}\}_{i=1}^N$ captured at times t_i:

$$J(\mu,\kappa) = \sum_{i=1}^N \left[K(t_i) - K_i^{obs}\right]^2 + \sum_{i=1}^N \left[M(t_i) - M_i^{obs}\right]^2. \tag{8}$$

By invoking the Weierstrass Extreme Value Theorem, a global minimum for J is guaranteed to exist on any closed and compact parameter domain $\Omega \subset \mathbb{R}^2_{++}$. If the localized sensitivity matrix S_{mat} possesses full column rank ($\mathrm{rank}(S_{mat}) = 2$), the parameters μ and κ are locally identifiable from the available temporal data (Ancker & Gafarian, 1987; Chen, 2007).

4.4. The 6D Augmented Forward Sensitivity System

To track the dynamic propagation and temporal evolution of parameter sensitivity, we differentiate the governing ordinary differential equations (1) directly with respect to the parameters. We define the forward sensitivity state variables as $P = \frac{\partial K}{\partial \mu}$, $Q = \frac{\partial M}{\partial \mu}$, $R = \frac{\partial K}{\partial \kappa}$ and $S = \frac{\partial M}{\partial \kappa}$. This generates a six-dimensional augmented nonlinear dynamical system:

$$\dot{K} = -\mu MK, \qquad \dot{M} = -\kappa MK, \tag{9a}$$

$$\dot{P} = -KM - \mu(MP + KQ), \qquad \dot{Q} = -\kappa(MP + KQ), \tag{9b}$$

$$\dot{R} = -\mu(MR + KS), \qquad \dot{S} = -KM - \kappa(MR + KS), \tag{9c}$$

subject to the unperturbed initial conditions $P(0) = Q(0) = R(0) = S(0) = 0$. This formulation highlights that while the overall coupled system is non-linear, the underlying sensitivity subsystem (9b-9c) remains strictly linear with respect to the sensitivity variables (P, Q, R, S) themselves.

4.5. Bifurcation and Structural Stability

Codimension-one bifurcation analysis shows that the non-zero eigenvalue of the system's Jacobian matrix evaluated along the continuous equilibrium branches (where $\lambda = -\kappa K_e$ or $\lambda = -\mu M_e$) remains strictly negative throughout the entire admissible positive parameter space (μ, $\kappa > 0$). Consequently, the system never satisfies the algebraic or spectral conditions required to trigger saddle-node, transcritical, pitchfork, or Hopf bifurcations.

We clarify that this claim of robust structural stability holds strictly under positive parameter perturbations ($\delta\mu$, $\delta\kappa \in \mathbb{R}$) such that $\mu + \delta\mu > 0$ and $\kappa + \delta\kappa > 0$). Under these variations, the topological structure of the phase portrait and the hyperbolic-like contraction toward the equilibrium manifold remain completely invariant, establishing the structural robustness of the model under realistic operational variations. The baseline parameters and the structural data configuration are summarized in Table 1.

Table 1. Baseline parameters and simulation data structure

Parameter / Metric	Red Force Condition (K)	Blue Force Condition (M)
Initial force size ($t = 0$)	Baseline Red ($K_0 = 100$)	Baseline Blue ($M_0 = 100$)
Attrition coefficient	Vector α component ($\mu = 0.05$)	Vector β component ($\kappa = 0.05$)
Asymptotic state ($t \to \infty$)	Convergence time ($t \to \infty$)	Invariant delta ($\Delta = 0$)
System properties	Sensitivity rank ($\mathrm{rank}(S_{mat}) = 2$)	Zero eigenvalue ($\lambda_1 = 0$)

5. Conclusions

The qualitative analysis of the deterministic Lanchester area-fire model establishes that military resource dissipation is an entirely irreversible thermodynamic-like process. By leveraging invariant manifold theory and executing a strict LaSalle Lyapunov construction, we verified that all admissible state trajectories converge globally to a non-hyperbolic equilibrium manifold. The model exhibits robust structural stability under positive parameter variations, and its relative sensitivity index peaks as a mathematical singularity exactly at the tactical stalemate threshold. This dual sensitivity and stability framework offers a mathematically sound, data-driven optimization layout for parameter identification in historical battle reconstructions and combat attrition simulations.

References

Ancker, C. J., Jr. (1995). A proposed foundation for a theory of combat. Naval Research Logistics (NRL), 42(3), 311-343.

Ancker, C. J., Jr., & Gafarian, A. V. (1987). The validity of assumptions underlying current uses of Lanchester attrition rates. Naval Research Logistics (NRL), 34(4), 505-533.

Brackney, H. (1959). Dynamics of military combat. Operations Research, 7(1), 30-44.

Britton, N. F., Partridge, L. W., & Franks, N. R. (1996). A mathematical model for the population dynamics of army ants. Bulletin of Mathematical Biology, 58(3), 471-492.

Chen, H. M. (2007). A non-linear inverse Lanchester square law problem in estimating the force-dependent attrition coefficients. European Journal of Operational Research, 182(2), 911-922.

Daras, N. J. (2012). Applications of Mathematics and Informatics in Military Science. Springer Science & Business Media.

Dolanský, L. (1964). Present state of the Lanchester theory of combat. Operations Research, 12(2), 344-358.

Epstein, J. M. (1997). Nonlinear dynamics, mathematical biology, and social science. Addison-Wesley Publishing Company.

González, E., & Villena, M. (2011). Spatial Lanchester models. European Journal of Operational Research, 210(3), 706-715.

Hartley, D. S., III. (1995). A mathematical model of attrition data. Naval Research Logistics (NRL), 42(4), 585-607.

Hartley, D. S., III, & Helmbold, R. L. (1995). Validating Lanchester's square law and other attrition models. Naval Research Logistics (NRL), 42(4), 609-633.

Helmbold, R. L. (1964). Some observations on the use of Lanchester's theory for prediction. Operations Research, 12(5), 778-781.

Helmbold, R. L. (1993). Osipov: the 'Russian Lanchester'. European Journal of Operational Research, 65(2), 278-288.

Israel, D. (1995). Lanchester modeling and the biblical account of the battles of Gibeah. Naval Research Logistics (NRL), 42(4), 579-584.

Lanchester, F. W. (1914). Aircraft in warfare: The dawn of the fourth Arm – No. V: The principle of concentration. Engineering, 98, 422-423.

Lanchester, F. W. (1916). Aircraft in warfare: the dawn of the fourth arm. London: Constable and Company Ltd.

Sheeba, P. S., & Ghose, D. (2008). Optimal resource allocation and redistribution strategy in military conflicts with Lanchester square law attrition. Naval Research Logistics (NRL), 55(6), 581-591.

Taylor, J. G. (1983). Lanchester Models of Warfare (Vol. I & II). Operations Research Society of America.

Willard, D. (1962). Lanchester as force in history: an analysis of land battles of the years 1618-1905. Research Analysis Corporation.

Willard, D. (1990). Lanchester attrition of interpenetrating forces. Naval Research Logistics (NRL), 37(1), 31-59.

Wiper, M. P., Pettit, L. I., & Young, K. D. S. (2000). Bayesian inference for a Lanchester type combat model. Naval Research Logistics (NRL), 47(7), 541-558.

Comparing Fuzzy Synergy Encodings in Robust R&D Project Portfolio Selection and Core-Constrained Cost Allocation

Ulviye Savaş[1,3*], Vildan Özkır[1], Selçuk Alp[2]

[1]*Yildiz Technical University, Department of Industrial Engineering, Istanbul, Türkiye*
[2]*Yildiz Technical University, Department of Statistics, Istanbul, Türkiye*
[3]*Turkcell Ödeme ve Elektronik Para Hizmetleri A.Ş/ Paycell R&D Center, İstanbul, Türkiye*
ulviye.savas@std.yildiz.edu.tr

Abstract

This study compares triangular, trapezoidal, and (p,q)-fractional fuzzy encodings of inter-project synergy within a two-layer framework for robust R&D project portfolio selection and core-constrained cost allocation. Layer I converts linguistic assessments of resource sharing, technological complementarity, knowledge transfer, output compatibility, and temporal coordination into coalition-specific savings. Layer II selects a portfolio by minimizing conservative gross cost less synergy savings, subject to budget, strategic benefit, mean–risk, and budgeted workforce and time constraints, and subsequently allocates its net cost through a cooperative cost game. The comparison uses a seven-project synthetic instance with 120 coalitions containing at least two projects. Five scenarios are examined while keeping coalition assessments, criterion weights, and saving caps fixed. All five scenarios select the same portfolio, comprising projects $P1, P2, P5, P6$, and $P7$. Estimated savings range from 2.507 to 2.872 million TL, and net portfolio costs range from 23.958 to 24.323 million TL. The reported allocations satisfy the core constraints in every scenario, with positive minimum coalition slack. These results show that the tested encodings change estimated savings and allocated costs without changing portfolio composition in this instance. Because the scenarios differ in both fuzzy representation and numerical calibration, the observed differences cannot be attributed solely to the fuzzy families.

Keywords: R&D project portfolio selection, fuzzy synergy assessment, robust optimization, budgeted uncertainty, cooperative game theory, core-constrained cost allocation

1. Introduction

R&D projects compete for budgets and specialist resources, but shared infrastructure, knowledge, and compatible outputs can also reduce their joint cost. Portfolio selection must therefore evaluate project combinations rather than individual rankings alone (Archer & Ghasemzadeh, 1999; Ghasemzadeh & Archer, 2000). Synergy and interdependence studies support this perspective (Vieira et al., 2024; Wang et al., 2023). When monetary savings cannot be observed directly, fuzzy representations translate linguistic assessments into numerical inputs (Bhattacharyya et al., 2011; Carlsson et al., 2007). Yet the encoding itself may influence the recommendation.

We compare triangular fuzzy numbers (TFNs), trapezoidal fuzzy numbers (TrFNs), and the membership/non-membership representation of Saifullah et al. (2026). The question is whether changes in estimated savings alter either portfolio composition or core feasibility. Robust optimization protects resource constraints (Bertsimas & Sim, 2004), while cooperative game theory formalizes allocation stability (Narbaev et al., 2022; Young, 1994). Distributionally robust studies (Delage & Ye, 2010; Liu & Liu, 2017) provide related background; the present model instead uses conservative cost inputs and a

* *Corresponding Author*

mean–risk limit. The contribution is a controlled comparison within a common selection and allocation framework.

2. Methods

2.1. Fuzzy Synergy Assessment

Layer I evaluates each coalition C against five criteria: resource sharing, technological complementarity, knowledge transfer, output compatibility, and temporal coordination. Their weights are 0.35, 0.25, 0.20, 0.10, and 0.10. Judgments, weights, and saving caps remain fixed across scenarios. Table 1 specifies the common linguistic inputs and their encodings.

Table 1. Linguistic encodings of synergy

Code	Linguistic term	TFN (l,m,u)	TrFN (a,b,c,d)	p-q (μ,η)
N	None	(0,0,0)	(0,0,0,0)	(0,1.00)
VL	Very low	(0,0,0.10)	(0,0,0.10,0.20)	(0.10,0.90)
L	Low	(0,0.10,0.30)	(0.10,0.20,0.20,0.30)	(0.20,0.80)
ML	Medium-low	(0.10,0.30,0.50)	(0.20,0.30,0.40,0.50)	(0.35,0.70)
M	Medium	(0.30,0.50,0.70)	(0.40,0.50,0.50,0.60)	(0.50,0.55)
MH	Medium-high	(0.50,0.70,0.90)	(0.50,0.60,0.70,0.80)	(0.65,0.40)
H	High	(0.70,0.90,1.00)	(0.70,0.80,0.80,0.90)	(0.80,0.25)
VH	Very high	(0.90,1.00,1.00)	(0.80,0.90,1.00,1.00)	(0.95,0.10)

Equations (1) and (2) aggregate the classical scores using criterion weights w_k. The TrFN expression is a parameter average, not generally the area centroid.

$$g_C^{TFN} = \sum_k w_k \frac{l_{Ck} + m_{Ck} + u_{Ck}}{3} \tag{1}$$

$$g_C^{TrFN} = \sum_k w_k \frac{a_{Ck} + b_{Ck} + c_{Ck} + d_{Ck}}{4} \tag{2}$$

Equation (3) defines the weighted membership components. For positive integers p and q, admissibility follows Eq. (4), with both input components in [0,1]. The score in Eq. (5) follows Saifullah et al. (2026); Eq. (6) maps its range to [0,1]. We use arithmetic aggregation, without adopting the Yager or CODAS procedures of Saifullah et al. (2026).

$$\overline{\mu}_C = \sum_k w_k \mu_{Ck}\,, \quad \overline{\eta}_C = \sum_k w_k \eta_{Ck} \tag{3}$$

$$0 \le \frac{\mu_{Ck}}{p} + \frac{\eta_{Ck}}{q} \le 1, \quad p,q \in \mathbb{N}_{>0}\,, \quad \mu_{Ck}, \eta_{Ck} \in [0,1] \tag{4}$$

$$Sc_C = \frac{\overline{\mu}_C}{p} - \frac{\overline{\eta}_C}{q} \tag{5}$$

$$g_C^{(p,q)} = \frac{Sc_C + 1/q}{1/p + 1/q} \tag{6}$$

The tested (p,q) values are (2,3), (1,4), and (4,1). They are labelled baseline, optimistic, and conservative according to the savings obtained in this instance. Equation (7) bases synergy savings on nominal costs,

whereas Eq. (9) deducts them from conservative gross costs. This modelling assumption retains the full uncertainty allowance by excluding it from the cost base used to calculate savings.

$$r_C^s = R_{max}(|C|)\, g_C^s, \qquad S_C^s = r_C^s \sum_{i\in C} c_i. \tag{7}$$

The caps $R_{max}(n)$ are 10%, 12%, 15%, 16%, 17%, and 18% for n = 2,…,7; singleton savings are zero. Savings in Eq. (7) apply to the exact coalition. Nested subcoalition savings are not added.

2.2. Robust Portfolio Selection

Layer II comprises two sequential optimization models: robust portfolio selection and core-constrained cost allocation. The portfolio selection model is presented first. Let P be the project set, M the managerial units, P_m the projects assigned to unit m, and A all nonempty subsets of P. Equation (8) links project variables x_i to the exact-portfolio variables z_C. Equation (9) minimizes conservative gross cost less synergy savings.

$$\sum_{C\in\mathcal{A}} z_C = 1, \qquad x_i = \sum_{C\in\mathcal{A}: i\in C} z_C\,, \qquad x_i, z_C \in \{0,1\}. \tag{8}$$

$$minZ_s = \sum_{i\in P} c_i^R\, x_i - \sum_{C\in\mathcal{A}} S_C^s\, z_C. \tag{9}$$

Equation (10) imposes the total net budget, local gross budgets, and minimum benefit, where c_i^R and f_i denote conservative cost and strategic benefit. The mean–dispersion risk limit in Eq. (11) uses means μ_i^R, standard deviations σ_i^R, and coefficient λ_R.

$$Z_s \le B_{\text{total}}, \qquad \sum_{i\in P_m} c_i^R\, x_i \le B_m \ (m \in M), \qquad \sum_{i\in P} f_i\, x_i \ge F_{\min}. \tag{10}$$

$$\sum_{i\in P} \mu_i^R\, x_i + \lambda_R \left[\sum_{i\in P} \left(\sigma_i^R\right)^2 x_i\right]^{1/2} \le R_{\max}. \tag{11}$$

Equation (11) assumes zero cross-project covariance. A distributionally robust interpretation would require an explicit ambiguity set and derivation. In Eqs. (12)–(13), $r \in \{H, T\}$ denotes workforce or time, a_i^r nominal use, Δa_i^r its upward deviation, K_m^r capacity, and Γ_m^r the uncertainty budget (Bertsimas & Sim, 2004).

$$\sum_{i\in P_m} a_i^r x_i \;+\; \Gamma_m^r \alpha_m^r \;+\; \sum_{i\in P_m} \beta_{im}^r \;\le\; K_m^r \quad \forall m, r \tag{12}$$

$$\alpha_m^r \;+\; \beta_{im}^r \;\ge\; \Delta a_i^r x_i\,, \quad \alpha_m^r, \beta_{im}^r \;\ge\; 0 \quad \forall i \in P_m \tag{13}$$

The nonnegative auxiliary variables in Eq. (13) implement budgeted uncertainty, with Γ_m^r between zero and the unit's project count. Time measures cumulative workload, not a precedence schedule. The selection problem admits a mixed-integer second-order cone formulation.

2.3. Core-Constrained Cost Allocation

After portfolio selection, the second optimization model in Layer II allocates the net portfolio cost among the selected projects P^*, which form the player set of a cost game. Equation (14) gives the stand-alone cost of each coalition Q; Eq. (15) defines its projects' proportional reference shares in the selected portfolio.

$$v_s(Q) \;=\; \sum_{i\in Q} c_i^R \;-\; S_Q^s \tag{14}$$

$$y_i^0 \;=\; \frac{c_i^R}{\sum_{j\in P*} c_j^R}\, v_s(P*) \tag{15}$$

Equation (16) minimizes absolute deviations from the reference. Equation (17) enforces efficiency and all proper-coalition constraints, including singleton rationality (Young, 1994). Equation (18) linearizes the deviations and requires nonnegative shares.

$$min \sum_{i\in P*} d_i \tag{16}$$
$$\sum_{i\in P*} y_i = v_s(P*), \quad \sum_{i\in Q} y_i \leq v_s(Q) \quad \forall \emptyset \neq Q \subsetneq P* \tag{17}$$
$$-d_i \leq y_i - y_i^0 \leq d_i, \quad y_i, d_i \geq 0 \quad \forall i \in P* \tag{18}$$

Equation (19) measures the smallest proper-coalition slack. A positive value means that every such inequality is strict. An empty core makes this allocation model infeasible; least-core optimization would be a separate extension.

$$\delta_s = min_{\emptyset\neq Q\subsetneq P*} \{ v_s(Q) - \sum_{i\in Q} y_i \} \tag{19}$$

3. Results and Discussion

The synthetic instance contains seven projects in three units (Table 2) and 120 coalitions of at least two projects. Monetary values are million TL. The net budget is 24.5, minimum benefit 395, risk limit 21.5, and $\lambda_R = 1.2$. Local gross budgets are 17.5, 12.0, and 11.5 for $M1 - M3$. In project order $P1 - P7$, nominal workforce requirements are (4, 5, 4, 3, 4, 3, 2), with maximum upward deviations (1.0, 1.2, 0.9, 0.8, 1.0, 0.7, 0.5). Nominal time requirements are (7, 9, 8, 6, 8, 6, 5), with deviations (1.2, 1.5, 1.3, 1.0, 1.2, 0.9, 0.7). Workforce/time capacities are 14.0/24.0, 8.2/15.5, and 7.5/14.5 for $M1 - M3$, respectively. Both uncertainty budgets equal one for every unit. Requirements, deviations, and capacities use consistent illustrative units for each resource; time represents cumulative workload.

Table 2. Candidate-project data

ID	Project	Unit	Nominal cost	Conservative cost	Benefit	Risk mean / s.d.
P1	AI demand forecasting	M1	4.800	5.280	86	3.20 / 0.70
P2	Data lake modernization	M1	6.200	6.940	92	3.80 / 0.80
P3	IoT edge monitoring	M2	5.500	6.100	77	3.50 / 0.80
P4	Zero-trust cybersecurity	M2	4.600	5.060	74	3.00 / 0.60
P5	Cloud ERP integration	M3	5.900	6.550	84	3.40 / 0.70
P6	Mobile customer analytics	M1	3.900	4.290	71	2.70 / 0.50
P7	RPA process automation	M3	3.400	3.770	69	2.40 / 0.40

The reported optimum is $P^* = \{P1, P2, P5, P6, P7\}$ throughout. Its nominal and conservative gross costs are 24.200 and 26.830, benefit is 402, and risk from Eq. (11) is 17.210. Table 3 reports savings from Eq. (7), net costs from Eq. (9), and core slack from Eq. (19).

Following the criterion order in Section 2.1, the linguistic assessments are (MH, H, MH, MH, MH) for P^*, (M, MH, M, MH, M) for $\{P1, P2, P3, P6, P7\}$, and (MH, H, MH, H, MH) for $\{P1, P2, P5, P6\}$. These assessments remain fixed across scenarios, using the linguistic encodings in Table 1.

Table 3. Outcomes for the common selected portfolio

Scenario	(p,q)	Score	Saving rate	Saving	Net cost	Min. core slack
TFN	-	0.742	11.87%	2.872	23.958	0.102
TrFN	-	0.688	11.00%	2.662	24.168	0.096
p-q baseline	2,3	0.668	10.68%	2.585	24.245	0.092

Scenario	(p,q)	Score	Saving rate	Saving	Net cost	Min. core slack
p-q optimistic	1,4	0.678	10.84%	2.623	24.207	0.094
p-q conservative	4,1	0.648	10.36%	2.507	24.323	0.088

The 0.365 net-cost spread is approximately 1.5% of baseline cost. Even the highest cost remains 0.177 below the budget. The second feasible portfolio, $\{P1, P2, P3, P6, P7\}$, has lower conservative gross cost (26.380 versus 26.830 million TL), but P^* achieves lower net cost through greater synergy savings in every scenario. Baseline net costs are 24.245 and 24.352 million TL for P^* and the alternative, respectively. For $M1$, cost/workforce/time use and capacity are 16.510/17.500, 13.20/14.00, and 23.50/24.00. For $M3$ they are 10.320/11.500, 7.00/7.50, and 14.20/14.50; $M2$ selects no project.

Table 4. Baseline cost allocation

Project	Conservative cost	Core share	Allocated saving
P1	5.280	4.771	0.509
P2	6.940	6.271	0.669
P5	6.550	5.919	0.631
P6	4.290	3.877	0.413
P7	3.770	3.407	0.363
Total	26.830	24.245	2.585

The shares in Table 4 follow Eq. (15). The reported core check satisfies Eq. (17), so the deviation objective in Eq. (16) is zero. Minimum slack is 0.088–0.102 across scenarios; $\{P1, P2, P5, P6\}$ is consistently the closest-to-blocking proper coalition. This is stability relative to the specified costs, not a unique fairness ranking.

4. Conclusion

This study examined how different fuzzy representations of synergy affect R&D project portfolio decisions within a two-layer framework: fuzzy synergy assessment in Layer I, followed by robust portfolio selection and core-constrained cost allocation in Layer II. In the seven-project synthetic instance, all five scenarios selected the same portfolio despite variations in estimated savings and net costs, while the reported cost allocations satisfied the core constraints. This finding indicates that, under the conditions examined, differences in synergy estimates were insufficient to alter portfolio composition. However, Table 1 varies both the fuzzy representation and its numerical calibration. A common [0,1] range does not make linguistic scores equivalent; the observed differences therefore cannot be attributed solely to the geometric properties of the fuzzy families.

The findings are limited to a small synthetic instance with fixed criterion weights and saving caps; the portfolio selection stage does not guarantee a feasible core allocation in other instances. Full replication additionally requires the complete linguistic assessment data for all 120 coalitions containing at least two projects. Future research using industrial data, tighter budget and resource constraints, and risk models incorporating cross-project covariance could clarify the conditions under which the observed selection stability persists. Comparisons with least-core and Shapley-value-based allocations could also provide a broader assessment of stability and fairness in cost sharing.

References

Archer, N. P., & Ghasemzadeh, F. (1999). An integrated framework for project portfolio selection. *International Journal of Project Management, 17*(4), 207–216. https://doi.org/10.1016/S0263-7863(98)00032-5

Bertsimas, D., & Sim, M. (2004). The price of robustness. *Operations Research, 52*(1), 35–53. https://doi.org/10.1287/opre.1030.0065

Bhattacharyya, R., Kumar, P., & Kar, S. (2011). Fuzzy R&D portfolio selection of interdependent projects. *Computers & Mathematics with Applications, 62*(10), 3857–3870. https://doi.org/10.1016/j.camwa.2011.09.036

Carlsson, C., Fullér, R., Heikkilä, M., & Majlender, P. (2007). A fuzzy approach to R&D project portfolio selection. *International Journal of Approximate Reasoning, 44*(2), 93–105. https://doi.org/10.1016/j.ijar.2006.07.003

Delage, E., & Ye, Y. (2010). Distributionally robust optimization under moment uncertainty with application to data-driven problems. *Operations Research, 58*(3), 595–612. https://doi.org/10.1287/opre.1090.0741

Ghasemzadeh, F., & Archer, N. P. (2000). Project portfolio selection through decision support. *Decision Support Systems, 29*(1), 73–88. https://doi.org/10.1016/S0167-9236(00)00065-8

Liu, Y., & Liu, Y.-K. (2017). Distributionally robust fuzzy project portfolio optimization problem with interactive returns. *Applied Soft Computing, 56*, 655–668. https://doi.org/10.1016/j.asoc.2016.09.022

Narbaev, T., Hazır, Ö., & Agi, M. (2022). A review of the use of game theory in project management. *Journal of Management in Engineering, 38*(6), Article 03122002. https://doi.org/10.1061/(ASCE)ME.1943-5479.0001092

Saifullah, Abdullah, S., Nawaz, M., & Ahmadzai, H. G. (2026). Multi criteria decision making approach using (p,q)-fractional fuzzy sets and Yager operations. *Discover Analytics, 4*, Article 4. https://doi.org/10.1007/s44257-025-00050-5

Vieira, G. B., Oliveira, H. S., de Almeida, J. A., & Belderrain, M. C. N. (2024). Project portfolio selection considering interdependencies: A review of terminology and approaches. *Project Leadership and Society, 5*, Article 100115. https://doi.org/10.1016/j.plas.2023.100115

Wang, Z., Esangbedo, M. O., & Bai, S. (2023). Project portfolio selection based on multi-project synergy. *Journal of Industrial and Management Optimization, 19*(1), 117–138. https://doi.org/10.3934/jimo.2021177

Young, H. P. (1994). Cost allocation. In R. J. Aumann & S. Hart (Eds.), *Handbook of game theory with economic applications* (Vol. 2, pp. 1193–1235). Elsevier. https://doi.org/10.1016/S1574-0005(05)80066-9

Rich, Green and Safety Focused Route Optimization

Sena Şaylıg*, Ibrahim Kucukkoc

Balikesir University, Department of Industrial Engineering, Balikesir, Türkiye
senasaylig@gmail.com, ikucukkoc@balikesir.edu.tr

Abstract

The Vehicle Routing Problem (VRP) is a cornerstone of logistics management. Since traditional VRP models fall short in reflecting real-world complexities, the "Rich Vehicle Routing Problem" has emerged to incorporate multiple constraints simultaneously. This study develops a heterogeneous "Rich, Green, and Security-Focused Vehicle Routing Problem" model to optimize cash transfer operations in the banking sector. The proposed approach expands the existing literature by simultaneously minimizing operational costs, environmental impacts (carbon emissions), and security risks within the objective function. A mixed-integer linear programming model was developed, coded in Python, and solved using the Gurobi Optimization solver, which yields optimal solutions within reasonable computational times. For large-scale datasets exceeding the exact optimization time limit, the multi-objective NSGA-II Genetic Algorithm is utilized to obtain near-optimal results. To translate this mathematical framework into a functional tool for decision-makers, a Streamlit-based Multi-Objective Route Planning System web application was developed for dynamic scenario analysis. The model's performance was evaluated across 9 distinct scenarios: standard, cost-focused, emissions-focused, safety-focused, fast service, electric vehicle, traffic, carbon tax and fleet-capacity scenarios. Results are analysed through interactive maps and graphs integrated into the web application, and the study contributes to both the academic literature and sector practice.

Keywords: Cash transfer, green logistics, rich vehicle routing, optimization, modeling

1. Introduction

The Vehicle Routing Problem (VRP) has been central to operations research since Dantzig and Ramser (1959). Classical formulations assume a homogeneous fleet and a single objective, so the Rich VRP emerged as a family of models combining several realistic constraints at once (Toth & Vigo, 2014; Lahyani et al., 2015). The Green VRP adds fuel consumption and carbon emissions, usually as a single objective or a penalty term (Asghari & Mirzapour Al-e-hashem, 2021), while cash-in-transit (CIT) routing introduces security as a decisive concern, because the vehicle carries a high-value load (Xu et al., 2019); there security is most often a hard restriction rather than a criterion traded off against the others.

This leaves a gap at the intersection of the three streams. To the best of our knowledge, no published model treats operational cost, carbon emissions and security risk as three simultaneous objectives for ATM cash distribution. This study addresses that gap by formulating a Green and Security-constrained Heterogeneous Rich Vehicle Routing Problem (G&SR-HRVRP) and applying it to the province of Balıkesir, Türkiye, which serves as the pilot region of an ongoing prototype study.

The contribution is threefold: an MILP formulation that minimises the three criteria simultaneously, the Pareto set being generated with the ε-constraint method; parameters derived from verifiable sources (chassis payload data, manufacturer catalogues, and district-level crime and socio-economic data with

* *Corresponding Author*

a neighbourhood modifier); and a working Streamlit-based decision support system that lets a planner run scenario analyses without reading the model.

2. Problem Definition

Banks replenish ATM networks daily or every other day using armoured vehicles. The province-level banking report of the Banks Association of Türkiye (2025) puts Balıkesir at roughly 1,310 ATMs, and a single planning cycle there can span several hundred kilometres, so the operation generates a non-negligible annual carbon footprint while exposing a high-value load to robbery risk. Three concerns act in opposite directions: cost favours the shortest tour; emissions favour electric vehicles, whose payload is considerably smaller; security favours routes avoiding high-risk neighbourhoods, which are seldom the cheapest. A single-objective model cannot express this tension.

2.1. Data Collection

ATM coordinates are real: collected with a Python web-scraping routine, cross-checked against the ATM location data published by the Banks Association of Türkiye (2025), de-duplicated and verified individually on Google Maps. Separate datasets were built for five banks, each record storing latitude, longitude, neighbourhood and district.

Cash demand could not be obtained, since banks do not disclose replenishment volumes, so it was generated from a public Kaggle ATM cash-demand dataset: a value drawn from an exponential distribution fitted to the dataset mean, multiplied by a district weight and a neighbourhood risk weight so that central locations receive higher volumes. A Q-Q plot validated the fit, the weighted mean being 37.53 units against a normalised reference mean of 37.56. Time windows were sampled from a normal distribution truncated to the 480–1080 minute working day and service times have a mean of 20 minutes.

The security index is constructed rather than assumed. A risk coefficient was computed for each of the 1,135 neighbourhoods of Balıkesir as the sum of a district base score, derived from crime records and socio-economic level, and a neighbourhood modifier of +10 for central commercial areas, +8 for busy areas, +5 for standard areas, 0 for ordinary areas and −5 for quiet rural areas. Coefficients lie in the interval [80, 95]. The arc risk r_{ij} is obtained from the coefficients of its endpoints.

2.2. Derivation of Fleet Parameters

Vehicle capacity was derived from the chassis rather than assumed. For the smallest van of the fleet (type A), the gross vehicle weight of 2,365 kg minus the kerb weight of 1,488 kg leaves 877 kg of payload; subtracting a three-person crew (≈250 kg) and B4-level armour with bullet-proof glazing (≈130 kg) yields 495 kg of net cash capacity. With the standardisation constant of 1 demand unit = 2.48 kg of banknotes this is $Q_k = 200$ units; the same procedure gives the other five vehicle types 110–355 units.

The derivation was cross-checked against banknote physics. Central Bank data give a mass of 1.13 g for a 200-lira note and the largest ATMs hold nine to ten million lira, so one demand unit corresponds to roughly 93,000 TL. The weight- and value-based checks agree, leaving a safety margin of about 25 %.

Consumption and emission coefficients come from manufacturer catalogues. For the diesel type-A van, WLTP consumption of 5.9 L/100 km gives $a_k = 0.059$ L/km, the 1,499 cm³ engine is assumed to consume $b_k = 0.7$ L/h at idle, and the diesel factor $ef_k = 2.68$ kg CO_2/L yields about 158 g CO_2/km. Electric variants use the same structure with kWh in place of litres, a charging efficiency of 0.90 and zero tailpipe emissions, the grid factor of 0.42 kg CO_2/kWh applying in well-to-wheel accounting.

3. Proposed Method

3.1. Mathematical Model

Let N be the set of ATMs and 0 the depot (the bank branch serving the instance), $V = \{0\} \cup N$, $A = \{(i, j) : i, j \in V, i \neq j\}$ the arc set and K the heterogeneous vehicle set. D_i is the cash demand of node i ($D_0 = 0$), Q_k the capacity of vehicle k and $Q^{ref} = \max_k Q_k$; d_{ij} and t_{ij} are the distance in km and the travel time in hours of arc (i, j). c_k^{km} [TL/km] and c_k^{time} [TL/h] are the distance and time cost rates and F_k [TL] the fixed dispatch cost of vehicle k. The coefficients a_k [L/km or kWh/km], b_k [L/h or kWh/h] and ef_k [kg CO_2/L or kg CO_2/kWh] describe consumption and emissions, β [TL/kg CO_2] is the carbon tax rate, r_{ij} the dimensionless arc risk, γ the cash-risk weight and R_k^{max} the maximum route risk allowed for vehicle k. Arc cost, fuel use, emissions and carbon cost are $c_{ij}^k = c_k^{km} \cdot d_{ij} + c_k^{time} \cdot t_{ij}$, $f_{k,ij} = a_k\, d_{ij} + b_k\, t_{ij}$, $e_{k,ij} = f_{k,ij} \cdot ef_k$ and $cc_{k,ij} = \beta \cdot e_{k,ij}$.

The decision variables are $x_{k,ij} \in \{0, 1\}$, equal to 1 if vehicle k traverses arc (i, j); $y_{k,ij} \geq 0$, the cash on board of vehicle k while it traverses arc (i, j); and $u_{k,i} \in \mathbb{Z}$, the visiting order of node i for vehicle k. The load variable y, absent from classical formulations, models the money physically on board at every point of the route.

$$\text{Min } Z_1 = \sum_{k\in K} \sum_{(i,j)\in A} \left(c_{ij}^k + cc_{k,ij}\right) \cdot x_{k,ij} + \sum_{k\in K} F_k \sum_{j\in N} x_{k,0j} \tag{1}$$

$$\text{Min } Z_2 = \sum_{k\in K} \sum_{(i,j)\in A} e_{k,ij} \cdot x_{k,ij} \tag{2}$$

$$\text{Min } Z_3 = \sum_{k\in K} \sum_{(i,j)\in A} r_{ij} \cdot \left(x_{k,ij} + \gamma / Q^{ref} \cdot y_{k,ij}\right) \tag{3}$$

$$\min Z_1 \quad \text{subject to} \quad Z_2 \leq \varepsilon_2,\ Z_3 \leq \varepsilon_3 \tag{4}$$

$$\sum_{k\in K} \sum_{i\in V} x_{k,ij} = 1 \qquad \forall j \in N \tag{5}$$

$$\sum_{j\in N} x_{k,0j} \leq 1 \qquad \forall k \in K \tag{6}$$

$$\sum_{i\in N} x_{k,i0} = \sum_{j\in N} x_{k,0j} \qquad \forall k \in K \tag{7}$$

$$\sum_{i\in V} x_{k,ih} - \sum_{j\in V} x_{k,hj} = 0 \qquad \forall h \in N, \forall k \in K \tag{8}$$

$$\sum_{i\in V} y_{k,ih} - \sum_{j\in V} y_{k,hj} = D_h \sum_{i\in V} x_{k,ih} \qquad \forall h \in N, \forall k \in K \tag{9}$$

$$D_j\, x_{k,ij} \leq y_{k,ij} \leq (Q_k - D_i)\, x_{k,ij} \qquad \forall k \in K, (i,j) \in A \tag{10}$$

$$\sum_{j\in N} y_{k,0j} \leq Q_k \qquad \forall k \in K \tag{11}$$

$$\sum_{(i,j)\in A} r_{ij} \cdot x_{k,ij} \leq R_k^{\max} \qquad \forall k \in K \tag{12}$$

$$u_{k,i} - u_{k,j} + |N|\, x_{k,ij} \leq |N| - 1,\quad 1 \leq u_{k,i} \leq |N| \quad \forall k \in K, i \neq j \in N \tag{13}$$

$$x_{k,ij} \in \{0,1\},\quad y_{k,ij} \geq 0,\quad u_{k,i} \in \mathbb{Z} \tag{14}$$

Equations (1)–(3) are the three objectives. Cost (1) contains the distance- and time-based arc cost, the carbon tax on the emissions of each arc and the fixed cost of every dispatched vehicle. Emissions (2) convert the distance-driven ($a_k d_{ij}$) and idling ($b_k t_{ij}$) consumption of each arc into kg CO_2 with the vehicle-specific factor ef_k, separating diesel from electric vehicles. Risk (3) combines exposure and consequence (Erkut & Verter, 1998): an arc contributes r_{ij} for being traversed and a further share proportional to the cash on board, normalised by Q^{ref}, so that crossing a dangerous neighbourhood with a full vehicle counts up to $(1 + \gamma)$ times as much as crossing it empty. (4) is the ε-constraint scalarisation (Mavrotas, 2009), minimising cost with the other two objectives bounded. Constraint (5) visits every ATM exactly once with exactly one vehicle; (6) lets each vehicle leave the depot at most once, so that an unneeded vehicle may stay idle, and (7) returns every dispatched vehicle to the depot; (8) is flow conservation; (9) is the single-commodity load balance: the cash entering an ATM minus the cash leaving it equals its demand if vehicle k serves it, so the load decreases along the route by exactly the amount delivered; (10) forbids load on unused arcs and bounds it, since at least the demand of the next ATM must still be on board and at most the capacity minus what has just been delivered; (11) limits the cash loaded at the depot to the

vehicle capacity; (12) is the security ceiling, capping the cumulative risk of vehicle k at R_k^{max}, set higher for better-protected vehicles; (13) is the Miller–Tucker–Zemlin subtour elimination condition (Miller et al., 1960) with the bounds on the order variable, redundant when all demands are positive since (9) excludes subtours; and (14) gives the variable domains.

The cash term of (3) is the soft counterpart of an operational rule that serves ATMs with a risk coefficient above 93 at the end of the route: instead of fixing a visiting position, it penalises carrying cash across high-risk arcs. The hard form of the rule, which forbids every arc from such an ATM to a lower-risk one, collapsed the feasible region in preliminary runs, so the scenarios use the soft form; Section 4.1 compares the two.

3.2. Solution Approach

The model is solved with the ε-constraint method: cost stays the primary objective while emissions and risk become upper bounds, and a 10 × 10 grid of ε values traces the Pareto set. The weighted sum was rejected because the objectives are measured in incommensurable units (lira, kilograms and a dimensionless index), because it can miss supported efficient points, and because practitioners reason in budgets and ceilings – exactly what an ε-constraint expresses.

One implementation detail proved decisive: the ε ranges are taken from the payoff table – the values the other objectives take at each individual optimum – not from worst-case bounds. Bounds set too wide push most grid points outside the efficient region and the scan repeats the same solution.

Because the Rich VRP is NP-hard, large instances may exceed the time limit, so NSGA-II (Deb et al., 2002) is used as a fallback, with population size and generation count scaled from 100 and 100 below 20 nodes to 500 and 300 above 50. Candidates are evaluated with the same three objective functions, so the exact and heuristic engines remain directly comparable.

3.3. Software Implementation

The model is delivered as a working web application: Python 3.11 with a Streamlit interface, Gurobi for the exact solve, pymoo for the NSGA-II fallback, Folium for the route maps on OpenStreetMap and ReportLab for the report. The interface exposes the model parameters directly: bank and instance size, vehicle type and capacity, cost, fuel and emission coefficients pre-filled from catalogue values, the security settings and the solver settings (ε grid, time budget, MIP gap and objective weights). Results appear as straight-line and real-road route maps (Figure 1), Pareto tables and plots, trade-off curves, a per-vehicle analysis and a PDF report; a scenario manager stores each policy question as a re-runnable scenario, and a route planning assistant answers questions by reading the solver objects directly, delegating free-form questions to a large language model.

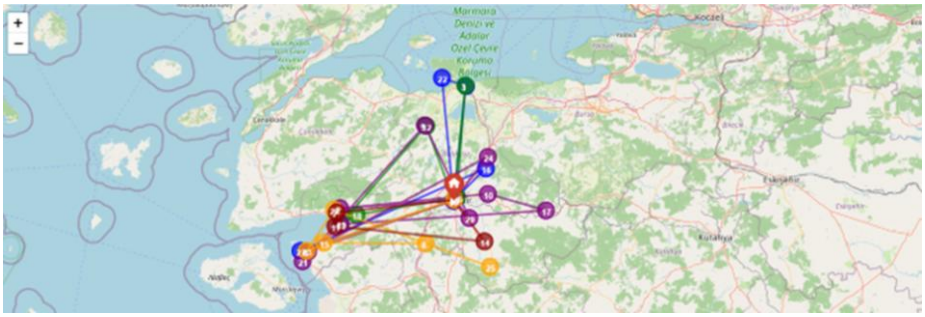


Figure 1. Optimised routes in the decision support system; each colour is one vehicle tour and the house marker is the depot (30-ATM instance of a second bank)

4. Results and Discussion

4.1. Verification Against a Manual Solution

The implementation was first verified against a solution computed by hand, on the smallest instance that still admits a non-trivial answer: three ATMs served by one vehicle, giving six possible routes, each evaluated directly from equations (1)–(2).

With the ordering rule in its hard form, the optimum is 0–5–29–26–0 (807.12 TL, 7.70 kg CO_2, 37.53 km), and Gurobi, solved with the same rule, returns exactly this sequence (Table 1); its values are 0.5 % higher because the implementation uses full-precision haversine distances, to which every term of (1) and (2) is proportional. Under the soft form, 0–5–26–29–0 is both cheaper (788.46 TL) and less risky (Z_3 = 34.29 against 37.18), because ATM 26 holds 16 of the 28 demand units and serving it early empties the vehicle before the long arcs to ATM 29.

Table 1. Verification of the implementation against a manual solution (3 ATMs, 1 vehicle; risk Z_3 from (3) with $\gamma = 1$)

Solution method	Ordering rule	Route	Distance (km)	Cost (TL)	Emissions (kg CO_2)	Risk Z_3
Manual enumeration	Hard	0–5–29–26–0	37.53	807.12	7.70	–
Gurobi (model)	Hard	0–5–29–26–0	37.71	810.79	7.73	37.18
Gurobi (model)	Soft, eq. (3)	0–5–26–29–0	36.67	788.46	7.52	34.29

4.2. Scenario Analysis

Nine scenarios were defined, each isolating a policy question a bank or regulator would realistically ask. All use the same instance — twelve ATMs of the first bank's dataset served by three diesel vans of types A, B and C (200, 250 and 355 units); Table 2 also reports total distance and Z_3 ($\gamma = 1$, no night factor) on a common basis. Scenario 1 is the baseline. Scenario 2 applies 14 TL/km and 300 TL/h to all vehicles; scenario 3 gives all vehicles the type-A consumption coefficients, isolating distance-driven emissions; scenario 4 minimises risk alone with a night risk factor of 1.3 and a cash weight of 0.1 per unit. Scenario 5 switches to the electric variants (337, 322 and 348 km of range, 30–45 minute charging, two charging stations, 2.5 TL/kWh). Scenario 6 is the traffic case: live traffic with hourly speed factors falling to 0.70 at the morning peak, congestion delays of 5, 10 and 12 minutes per vehicle, an 08:00 departure and 8 g CO_2 per idling minute. Scenario 7 prices carbon at 0.08 TL/kg CO_2, scenario 8 raises cruising speeds to 60, 60 and 40 km/h, and scenario 9 replaces the mixed fleet with three identical 250-unit vehicles. The solver used a 60-second limit per grid point, a zero MIP gap and a 300-second budget for the Pareto scan.

Table 2. Results of the nine scenario analyses
(first bank, 12 ATMs, 3 vehicles; distance and Z_3 on a common basis)

Scenario	Cost (TL)	Emissions (kg CO_2)	Distance (km)	Risk Z_3 ($\gamma = 1$)	Same tours as 1	Pareto scan (s)
1 · Standard optimisation	11,222	93.9	410.3	472.0	–	308
2 · Cost focused	9,314	93.9	410.3	472.1	yes	224
3 · Emissions focused	11,222	84.9	410.3	472.0	yes	245
4 · Safety focused	11,609	97.4	426.7	472.4[a]	no	10
5 · Electric vehicle	4,473[b]	44.2[c]	410.3	472.0	yes	307
6 · Traffic	12,152	99.5	410.3	472.0	yes	302
7 · Carbon tax	11,234	93.9	410.5	469.6	no	153
8 · Fast service	10,107	87.1	410.3	472.0	yes	302
9 · Fleet and capacity	11,765	108.1	521.7	739.1	no	315

[a] 401.7 with the scenario's own cash weight. [b] Energy-only per-kilometre rate. [c] Includes grid emissions (0.42 kg CO_2/kWh).

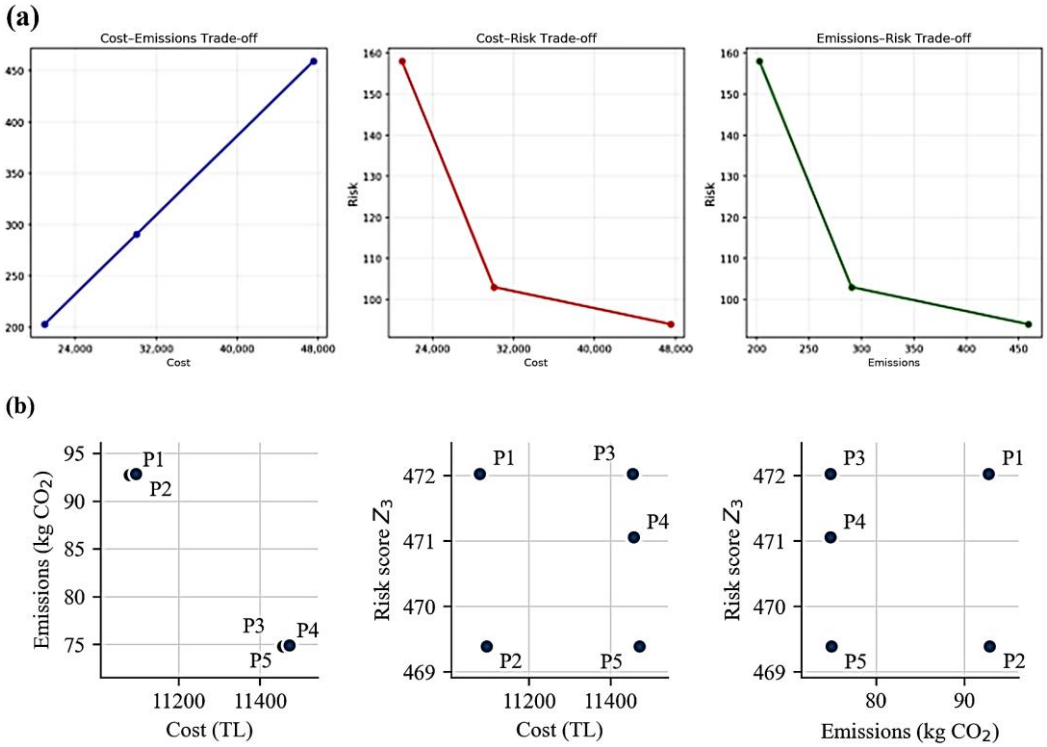


Figure 2. Trade-off curves: (a) application output for the run of Figure 1; (b) the same projections for the 12-ATM mixed-fleet Pareto set of Figure 3

Several observations follow from Table 2. First, scenarios 2, 3, 5, 6 and 8 return the same tours as the baseline; their figures differ only through the pricing coefficients, and only scenarios 4, 7 and 9 change the routing.

Second, the safety-focused plan of scenario 4 leaves total risk on the common basis unchanged (472.4 against 472.0) but redistributes it: the cash carried across risky arcs falls by 12.7 % and the exposure of the riskiest route by 9.8 %, at 3.5 % more cost and 3.8 % more emissions. Security in CIT routing has traditionally been discussed qualitatively; the model attaches a price to it.

Third, electrification halves emissions on identical tours (44.2 against 93.9 kg CO_2, grid factor included for electric vehicles); its 60 % cost advantage is an upper bound, since the per-kilometre rate covers only energy for electric vehicles but full operating cost for diesel ones. It must be read together with Section 2.2, since the binding constraint for electric variants is payload and range. Fourth, congestion is the costliest disturbance tested: the traffic case of scenario 6 is the most expensive of the nine at 12,152 TL, about 8 % above the baseline, because reduced speeds and idling lengthen travel time and raise both the time-based cost and the idle emissions, while the tours themselves are unchanged. Carbon pricing (scenario 7) shifts total cost by only 0.1 %, although it tilts the comparison towards electric vehicles, and faster cruising (scenario 8) cuts cost by about 10 %. Fleet heterogeneity generates the gains: the uniform fleet of scenario 9 raises total distance from 410.3 km to 521.7 km and the risk score to 739.1.

Each single-objective optimum is solved in under 20 seconds for this instance. The mixed diesel-and-electric run behind Figure 3 returns five non-dominated solutions out of 51 feasible ones (cost 11,080–11,471 TL, emissions 74.8–92.9 kg CO_2, risk 469.4–472.0). The front is thin because cost and emissions are both largely proportional to distance. Genuine trade-offs appear only once the fleet mixes propulsion types, because the cheaper vehicle is then also the more polluting one while the cleaner one carries less.

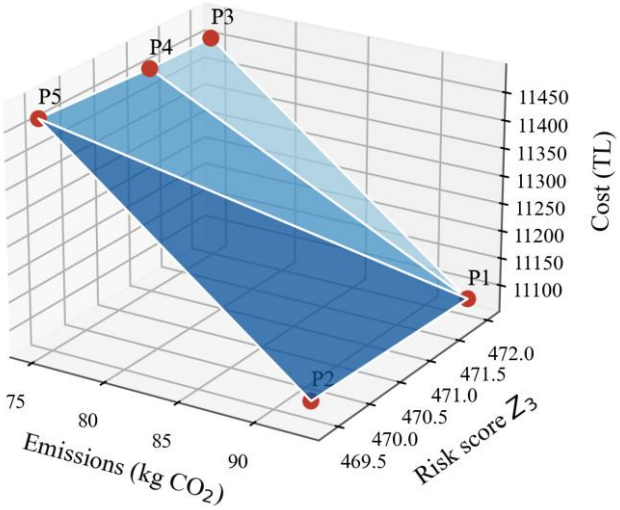


Figure 3. Pareto surface: Delaunay triangulation of the five non-dominated solutions, each face a distinct trade-off region

5. Conclusion

This study formulated a Green and Security-constrained Heterogeneous Rich Vehicle Routing Problem for ATM cash distribution, solved with the ε-constraint method in Gurobi (NSGA-II as fallback) and delivered as a Streamlit-based decision support system. To the best of our knowledge this is the first model treating the three criteria as simultaneous objectives in CIT routing; the security index is constructed and reproducible, and every fleet parameter is derived from catalogue and physical data.

The numerical results quantify relationships previously discussed only qualitatively: a safety-focused plan cuts the cash carried across risky arcs by 12.7 % for 3.5 % more money, an electric fleet halves emissions on the same tours with a cost advantage that depends mainly on the per-kilometre rate assumed, congestion is the costliest disturbance tested, and a uniform fleet increases distance by roughly a quarter. The deliverable is the Pareto set rather than a single route.

The limitations are acknowledged: demand and risk are treated as known, real demand data could not be obtained and the MILP grows difficult with instance size. Future work includes stochastic programming, a stronger metaheuristic, field validation with a CIT operator and extending the Balıkesir pilot study to other provinces.

Acknowledgements

This work was supported by the Scientific and Technological Research Council of Türkiye (TÜBİTAK) under the '2209-A Research Project Support Programme for Undergraduate Students' conducted by the Science Fellowships and Grant Programmes Directorate (BIDEB) with the project number 1919B012520102. We extend our sincere gratitude to TÜBİTAK for their invaluable support.

References

Asghari, M., & Mirzapour Al-e-hashem, S. M. J. (2021). Green vehicle routing problem: A state-of-the- art review. *International Journal of Production Economics, 231*, 107899. https://doi.org/10.1016/j.ijpe.2020.107899

Banks Association of Türkiye. (2025). *Banking system in Türkiye: Province-level statistics*. Banks Association of Türkiye.

Dantzig, G. B., & Ramser, J. H. (1959). The truck dispatching problem. *Management Science, 6*(1), 80–91. https://doi.org/10.1287/mnsc.6.1.80

Deb, K., Pratap, A., Agarwal, S., & Meyarivan, T. (2002). A fast and elitist multiobjective genetic algorithm: NSGA-II. *IEEE Transactions on Evolutionary Computation, 6*(2), 182–197. https://doi.org/10.1109/4235.996017

Erkut, E., & Verter, V. (1998). Modeling of transport risk for hazardous materials. *Operations Research, 46*(5), 625–642. https://doi.org/10.1287/opre.46.5.625

Lahyani, R., Khemakhem, M., & Semet, F. (2015). Rich vehicle routing problems: From a taxonomy to a definition. *European Journal of Operational Research, 241*(1), 1–14. https://doi.org/10.1016/j.ejor.2014.07.048

Mavrotas, G. (2009). Effective implementation of the ε-constraint method in multi-objective mathematical programming problems. *Applied Mathematics and Computation, 213*(2), 455–465. https://doi.org/10.1016/j.amc.2009.03.037

Miller, C. E., Tucker, A. W., & Zemlin, R. A. (1960). Integer programming formulation of traveling salesman problems. *Journal of the ACM, 7*(4), 326–329. https://doi.org/10.1145/321043.321046

Toth, P., & Vigo, D. (Eds.). (2014). *Vehicle routing: Problems, methods, and applications* (2nd ed.). SIAM. https://doi.org/10.1137/1.9781611973594

Xu, G., Li, Y., Szeto, W. Y., & Li, J. (2019). A cash transportation vehicle routing problem with combinations of different cash denominations. *International Transactions in Operational Research, 26*(6), 2179–2198. https://doi.org/10.1111/itor.12640

Application of E-Bayesian Estimation to the Rayleigh Distribution in Wind Energy

İlhan Usta[1*], Hanefi Gezer[1], İbrahim Arık[2], Yeliz Mert Kantar[1]

[1] *Eskişehir Technical University, Department of Statistics, Eskişehir, Türkiye*
[2] *Kütahya Dumlupınar University, Department of Business Administration, Kütahya, Türkiye*
iusta@eskisehir.edu.tr, hgezer@eskisehir.edu.tr, ibrahim.arik@dpu.edu.tr, ymert@eskisehir.edu.tr

Abstract

In wind energy assessment, the Rayleigh distribution is widely used to describe the wind speed regime, since its single scale parameter can be estimated directly from the mean wind speed. In this study, an E-Bayesian estimator was obtained for the parameter of the Rayleigh distribution by averaging the ordinary Bayes estimator over a hyperprior placed on the prior hyperparameters; closed-form expressions were obtained under three hyperpriors and three loss functions. The estimator was applied to wind speed data from the Şile meteorological station, Türkiye. The E-Bayesian estimator yielded results close to those of the maximum likelihood, method of moments, graphical, power density, and ordinary Bayes estimators across all months considered. The results show that E-Bayesian estimation provides closed-form estimators for the Rayleigh distribution, with performance comparable to that of classical estimation methods in the considered wind energy applications.

Keywords: Rayleigh distribution, wind speed, wind energy, classical estimation, E-Bayes estimation

1. Introduction

Wind energy is one of the most important renewable energy sources, and the accurate characterization of wind speed is central to power generation planning (Celik, 2004). Because wind speed is a random variable, its probability distribution plays a key role in describing wind regimes and in estimating the mean wind power density available at a site (Shi et al., 2021). Among the distributions used for this purpose, the Rayleigh distribution (RD) is particularly attractive: it is the Weibull distribution with the shape parameter fixed at 2, so that a single parameter, estimated from the mean wind speed alone, describes the whole wind regime (Shi et al., 2021; Celik, 2004).

The parameter of RD is traditionally estimated by maximum likelihood, the method of moments, the graphical (least-squares) method, and the power-density method (Seguro & Lambert, 2000; Akdağ & Dinler, 2009; Bulut & Bingöl, 2024). Alternative and improved classical estimators have also been proposed for the closely related Weibull family (Usta, 2016; Usta et al., 2018), reflecting a continuing effort to improve on the four estimators above.

In contrast, Bayesian estimation is still rarely used in wind energy: a recent review of wind speed distributions does not mention Bayesian estimation among the methods examined (Shi et al., 2021), and a dedicated review of Bayesian estimation in wind energy applications concludes that its use in this field remains limited (Chiodo et al., 2023); existing Bayesian applications, meanwhile, focus instead on the Weibull distribution (Erto et al., 2010).

E-Bayesian estimation, introduced by Han (2009) for the failure rate in reliability theory and developed further by Han (2019, 2020), addresses a specific weakness of ordinary Bayesian estimation: the Bayes estimator is conditional on prior hyperparameters that are treated as fixed and known, even though in practice they must themselves be elicited from data. E-Bayesian estimation instead averages the Bayes

[*] *Corresponding Author*

estimator over a hyperprior placed on the hyperparameters, and remains closed form. Several studies have extended E-Bayesian estimation to the Rayleigh distribution (EL-Sagheer, 2017; Panda & Bhoi, 2025). The Rayleigh distribution has also recently been revisited under censored-sampling schemes by the present authors (Gezer & Usta, 2026). However, these studies focus exclusively on censored lifetime data. To the best of our knowledge, no published study has applied E-Bayesian estimation to wind-speed data.

This paper proposes an E-Bayesian estimator for the rate parameter of RD in wind-energy applications and compares it with the classical and ordinary Bayesian estimators through an application to wind-speed records from a Turkish meteorological station.

2. Estimation Methods

2.1. The Rayleigh Distribution Model

Wind-energy studies commonly express the RD using a scale parameter c. By introducing the rate parameter $\lambda = 1/c^2$, the density can be written in the form used throughout this paper,

$$f(v \mid \lambda) = 2\lambda v e^{-\lambda v^2}, \qquad v > 0, \qquad \lambda > 0 \tag{1}$$

for a sample of n wind speeds $v_1, \ldots, v_n$, with sufficient statistic

$$S = \sum_{i=1}^{n} v_i^2. \tag{2}$$

The mean wind power density, the quantity ultimately of interest for power-generation planning, follows directly from the moments of RD as

$$\frac{P}{A} = \frac{1}{2}\rho\, E[V^3] = \frac{1}{2}\rho\, \Gamma\left(\frac{5}{2}\right)\lambda^{-3/2} \tag{3}$$

where ρ is the air density. Accurate estimation of λ is therefore a prerequisite for reliable wind-power assessment.

2.2. Classical Estimation

Four classical estimators of λ are commonly used in wind-energy applications: the maximum-likelihood (MLE) and method-of-moments (MOM), and graphical (GM) estimators are due to Seguro & Lambert (2000), while the power-density estimator (PDM), which matches the third sample moment entering the wind-power density directly, is due to Akdağ & Dinler (2009).

The graphical estimator is obtained by regressing $Y_i = \ln[-\ln(1 - F_i)]$ on $X_i = \ln v_{(i)}$, where $v_{(i)}$ denotes the ith order statistic and F_i is its median-rank plotting position. Since the Rayleigh distribution is a Weibull distribution with shape parameter 2, the slope of this regression is fixed at 2, and only the intercept (β_0) is estimated by ordinary least squares. Table 1 collects the resulting formulas for each of the four estimators.

Table 1. Classical estimators of λ

Estimator	Formula		Estimator	Formula
MLE	$\hat{\lambda}_{MLE} = \frac{n}{S} = \frac{n}{\sum_{i=1}^{n} v_i^2}$		GM	$\hat{\lambda}_{GM} = \exp(\beta_0)$
MOM	$\hat{\lambda}_{MOM} = \left(\frac{\Gamma(3/2)}{\bar{v}}\right)^2 = \frac{\pi}{4\bar{v}^2}$		PDM	$\hat{\lambda}_{PDM} = \left(\frac{\Gamma(5/2)}{\frac{1}{n}\sum_{i=1}^{n} v_i^3}\right)^{2/3}$

2.3. Bayesian Estimation

In the Bayesian framework, the unknown parameter λ is regarded as a random variable, and the prior knowledge about it is expressed through a prior distribution $\pi(\lambda)$. Bayes' theorem combines this prior distribution with the information in the observed data, carried by the likelihood function $L(\mathbf{v} \mid \lambda)$. The result is the posterior distribution of λ:

$$\pi(\lambda \mid \mathbf{v}) = \frac{L(\mathbf{v} \mid \lambda)\pi(\lambda)}{\int_0^\infty L(\mathbf{v} \mid \lambda)\pi(\lambda)d\lambda} \tag{4}$$

For the Rayleigh rate parameter, we adopt a Gamma prior, $\lambda \sim \text{Gamma}(a, b)$, with density

$$\pi(\lambda \mid a, b) = \frac{b^a}{\Gamma(a)}\lambda^{a-1}e^{-b\lambda}, \qquad \lambda > 0, a, b > 0 \tag{5}$$

The Gamma family is chosen because it is conjugate to the Rayleigh likelihood, so the posterior stays in the same family. The hyperparameters a and b reflect the prior belief about λ.

Given a random sample $\mathbf{v} = (v_1, \ldots, v_n)$ from the Rayleigh distribution, the likelihood function, up to a multiplicative constant that does not depend on λ, is

$$L(\mathbf{v} \mid \lambda) \propto \lambda^n e^{-\lambda S} \tag{6}$$

Substituting (5) and (6) into (4), the kernel of the posterior is

$$\pi(\lambda \mid \mathbf{v}) \propto \lambda^{a+n-1}e^{-(b+S)\lambda} \tag{7}$$

Normalising this kernel gives the posterior density of λ:

$$\pi(\lambda \mid \mathbf{v}) = \frac{(b+S)^{a+n}}{\Gamma(a+n)}\lambda^{a+n-1}e^{-(b+S)\lambda}, \quad \lambda > 0 \tag{8}$$

which is the probability density function of a Gamma distribution. Hence the posterior distribution of λ is $\lambda \mid \mathbf{v} \sim \text{Gamma}(a + n,\ b + \text{S})$.

A Bayes estimator is the value that minimises the posterior expected loss, rather than the posterior density itself, and different loss functions therefore lead to different point estimates from the same posterior. The Bayes estimators of λ ($\hat{\lambda}_{B,L}$) under the three loss functions considered in this study are summarized in Table 2. The squared error loss function (SELF) is the usual symmetric choice and returns the posterior mean as the optimal Bayes estimator, while the quadratic (QLF) and DeGroot (DLF) loss functions penalise the relative error between the estimator and the true parameter.

Table 2. Bayes estimators of λ under three loss functions

Loss function	Bayes estimator
SELF – squared error	$\hat{\lambda}_{B,SELF} = E(\lambda) = \frac{n+a}{S+b}$
QLF – quadratic	$\hat{\lambda}_{B,QLF} = \frac{E(\lambda^{-1})}{E(\lambda^{-2})} = \frac{n+a-2}{S+b}$
DLF – DeGroot	$\hat{\lambda}_{B,DLF} = \frac{E(\lambda^2)}{E(\lambda)} = \frac{n+a+1}{S+b}$

2.4. E-Bayesian Estimation

The Bayes estimators in Table 2 are conditional on hyperparameters (a, b) that are themselves treated as fixed and known, even though in practice they must be elicited from the data. E-Bayesian estimation (Han, 2009) instead takes the expectation of the Bayes estimator over a hyperprior $\pi(a, b)$ placed jointly on the hyperparameters, over their joint support set D,

$$\hat{\lambda}_{EB} = E_{\pi}\left[\hat{\lambda}_{B,L}(a,b)\right] = \iint_{D} \hat{\lambda}_{B,L}\,(a,b)\pi(a,b)dadb \tag{9}$$

Following Han (2009), the hyperparameters are chosen such that the gamma prior $\pi(\lambda \mid a, b)$ is a decreasing function of λ, which holds if and only if

$$\frac{\partial}{\partial\lambda}\pi(\lambda \mid a,b) = \frac{\partial}{\partial\lambda}\left(\frac{b^{a}}{\Gamma(a)}\lambda^{a-1}e^{-b\lambda}\right) < 0 \quad \Leftrightarrow \quad 0 < a < 1, \qquad b > 0. \tag{10}$$

This condition restricts a to the interval $(0,1)$ irrespective of b. Throughout this study, a is treated as known and fixed, whereas the uncertainty in b is modelled by a hyperprior distribution $\pi_j(b)$ defined on $(0, k)$, with $k > 0$. Under these assumptions, the general definition of the E-Bayesian estimator reduces to

$$\hat{\lambda}_{EB} = \int_{0}^{k} \hat{\lambda}_{B}\,(b)\pi_j(b)db \tag{11}$$

where $\hat{\lambda}_{B,L}(b)$ is the Bayes estimator of λ under a given loss function, as reported in Table 2.
Three hyperpriors are considered for b in this study: decreasing, uniform, and increasing (Table 3). They represent different prior beliefs about the location of b within $(0, k)$. π_1 puts more weight on values of b close to zero, π_3 favours values close to k, and π_2 assigns equal weight to the whole interval. As π_2 is non-informative within $(0, k)$, it is adopted as the baseline specification of this study.

Table 3. Hyperprior distributions for b

Hyperprior	Density	$E[b]$
$\pi_1(b)$–decreasing	$\pi_1(b) = \frac{2(k-b)}{k^2}, 0 < b < k$	$E_{\pi_1}[b] = \frac{k}{3}$
$\pi_2(b)$–uniform	$\pi_2(b) = \frac{1}{k}, 0 < b < k$	$E_{\pi_2}[b] = \frac{k}{2}$
$\pi_3(b)$–increasing	$\pi_3(b) = \frac{2b}{k^2}, 0 < b < k$	$E_{\pi_3}[b] = \frac{2k}{3}$

The Bayes estimators in Table 2 can be written in the unified form $\hat{\lambda}_{B,L}(b) = \alpha_L/(b + S)$, where $\alpha_L = n + a + \delta_L$ and $\delta_L = 0, -2$ and $+1$ under the SELF, QLF and DLF, respectively. The case of the QLF requires $n + a > 2$. Substituting $\hat{\lambda}_{B,L}(b)$ into (11) and integrating with respect to each hyperprior in Table 3 yields the following E-Bayesian estimators of λ under loss function $L \in \{\text{SELF}, \text{QLF}, \text{DLF}\}$:

$$\hat{\lambda}_{EB,L}^{(\pi_1)} = \frac{2\alpha_L}{k^2}\left[(S+k)\ln\left(\frac{S+k}{S}\right) - k\right] \tag{12}$$

$$\hat{\lambda}_{EB,L}^{(\pi_2)} = \frac{\alpha_L}{k}\ln\left(\frac{S+k}{S}\right) \tag{13}$$

$$\hat{\lambda}_{EB,L}^{(\pi_3)} = \frac{2\alpha_L}{k^2}\left[k - S\ln\left(\frac{S+k}{S}\right)\right] \tag{14}$$

Equations (12)–(14) therefore give nine E-Bayesian estimators: one for each combination of loss function and hyperprior. All of them are available in closed form, so neither numerical integration nor MCMC sampling is required.

3. Application to Real Wind-Speed Data

The estimators were applied to the hourly wind speeds recorded at the Şile meteorological station in March, April and May 2005, for which complete records are available ($n = 744$, 720 and 744, respectively). In accordance with Section 2.4, the hyperparameter a was fixed at 0.5, the midpoint of $(0,1)$. The hyperparameter b was elicited from the hourly records of the same month in 1999–2004: the yearly estimates $\hat{\lambda}_j = n_j / \sum_{i=1}^{n_j} v_{ji}^2$ were computed, and $\hat{b} = a/\bar{\lambda}$ was chosen, where $\bar{\lambda}$ is the mean of $\hat{\lambda}_j$, so that the prior mean $a/\hat{b}$ equals the average historical rate. The upper bound of the hyperprior was set to $k = 2\hat{b}$, so that the main hyperprior π_2 is centred at the elicited value, i.e. $E(b) = \hat{b}$. The resulting values are given in Table 4.

Since the Rayleigh distribution is a Weibull distribution with shape parameter 2, it was tested against the two-parameter Weibull distribution by a likelihood-ratio (LR) test. As shown in Table 4, the estimated Weibull shape parameters (1.95–2.06) are close to 2, and the LR test does not reject the Rayleigh model at the 5% level in any month. The Kolmogorov–Smirnov (KS) statistics are also small (0.042–0.071), indicating close agreement between the empirical and fitted Rayleigh distribution functions. Since the KS test is highly sensitive for samples of this size ($n > 700$), even minor deviations can be statistically significant (Stephens, 1974); therefore, the KS values are interpreted together with the LR test and the goodness-of-fit criteria in Table 5, which jointly support the adequacy of the Rayleigh model for all three months.

Table 4. Rayleigh goodness of fit and hyperparameters for the Şile station, 2005

Month	n	Weibull $\hat{k}$	KS D	LR p-value	$\hat{b}$	k
March	744	1.967	0.0714	0.562	6.532	13.065
April	720	1.948	0.0651	0.354	4.384	8.768
May	744	2.058	0.0420	0.309	3.854	7.707

Table 5 compares the classical estimators (MLE, MOM, GM and PDM), the Bayes estimator under the SELF (B-SELF) and the E-Bayesian estimator under the QLF with the main hyperprior π_2 (EB-QLF). Owing to space limitations, the results for the remaining estimators and hyperpriors are available from the corresponding author upon request. The goodness of fit was evaluated by comparing the observed relative frequencies f_j with the relative frequencies $\hat{f}_j$ estimated from the fitted Rayleigh distribution in N wind-speed classes of width 1 m/s. R^2 is the squared correlation coefficient between f_j and $\hat{f}_j$, and

$$\mathrm{RMSE} = \left[\frac{1}{N}\sum_{j=1}^{N}\left(f_j - \hat{f}_j\right)^2\right]^{1/2}, \qquad \mathrm{MAE} = \frac{1}{N}\sum_{j=1}^{N}\left|f_j - \hat{f}_j\right| \tag{15}$$

For further details on these criteria, see Usta et al. (2018).

Table 5. Comparison of classical, Bayes and E-Bayesian estimators of λ for the Şile station, 2005

Estimator	March				April				May			
	$\hat{\lambda}$	R^2	RMSE	MAE	$\hat{\lambda}$	R^2	RMSE	MAE	$\hat{\lambda}$	R^2	RMSE	MAE
MLE ($\hat{\lambda}_{MLE}$)	0.0695	0.9418	0.0192	0.0114	0.0844	0.9048	0.0276	0.0209	0.1883	0.9973	0.0070	0.0057
MOM ($\hat{\lambda}_{MOM}$)	0.0703	0.9430	0.0191	0.0115	0.0860	0.9077	0.0273	0.0211	0.1869	0.9973	0.0071	0.0057
GM ($\hat{\lambda}_{GM}$)	0.0698	0.9424	0.0192	0.0114	0.0852	0.9064	0.0274	0.0210	0.1803	0.9963	0.0090	0.0059
PDM ($\hat{\lambda}_{PDM}$)	0.0688	0.9406	0.0194	0.0113	0.0832	0.9022	0.0280	0.0206	0.1879	0.9973	0.0070	0.0057
B-SELF ($\hat{\lambda}_{B,SELF}$)	0.0695	0.9419	0.0192	0.0114	0.0844	0.9048	0.0276	0.0209	0.1882	0.9973	0.0070	0.0057
EB-QLF ($\hat{\lambda}_{EB,QLF}^{(\pi_2)}$)	0.0693	0.9415	0.0193	0.0114	0.0842	0.9043	0.0277	0.0208	0.1877	0.9973	0.0070	0.0057

In March and April, all estimators give very similar results; MOM attains the highest R^2 and the lowest RMSE, while PDM gives the lowest MAE. In May, all estimators except GM yield practically identical values ($R^2 = 0.9973$). The EB-QLF estimator is competitive with the classical estimators in all three months: its R^2, RMSE and MAE values differ from those of the best estimator by at most 0.0034, 0.0004 and 0.0002, respectively, and in May it outperforms GM in all three criteria. Owing to the large sample size, the EB-QLF estimates are very close to the MLE, with differences below 0.5%. An important advantage of the E-Bayesian approach is that b need not be fixed at a single value; instead, the uncertainty about b is averaged over the hyperprior, while the estimator remains in closed form. Hence, the E-Bayesian estimator incorporates both the historical prior information and the uncertainty about the hyperparameter without any loss in goodness of fit.

4. Conclusion

To the best of our knowledge, this is the first application of E-Bayesian estimation to wind-speed data. The E-Bayesian estimators of the Rayleigh rate parameter have closed forms under all three loss functions and require no iterative optimisation or numerical integration. Applied to three months of Şile station data, the E-Bayesian estimator stays close to the classical and ordinary Bayes estimators. No estimator dominates uniformly, but the E-Bayesian estimator remains competitive throughout. Therefore, it is a practical, closed-form alternative to classical and ordinary Bayesian estimators.

Acknowledgements

This study was supported by Eskişehir Technical University Scientific Research Projects Commission under grant no: 25ADP219.

References

Akdağ, S. A., & Dinler, A. (2009). A new method to estimate Weibull parameters for wind energy applications. Energy Conversion and Management, 50(7), 1761–1766. https://doi.org/10.1016/j.enconman.2009.03.020

Bulut, A., & Bingöl, O. (2024). Weibull parameter estimation methods on wind energy applications- a review of recent developments. Theoretical and Applied Climatology, 155, 9157–9184. https://doi.org/10.1007/s00704-024-05184-2

Celik, A. N. (2004). A statistical analysis of wind power density based on the Weibull and Rayleigh models at the southern region of Turkey. Renewable Energy, 29(4), 593–604. https://doi.org/10.1016/j.renene.2003.07.002

Chiodo, E., Diban, B., Mazzanti, G., & De Angelis, F. (2023). A review on wind speed extreme values modeling and Bayes estimation for wind power plant design and construction. Energies, 16(14), 5456. https://doi.org/10.3390/en16145456

EL-Sagheer, R. M. (2017). E-Bayesian estimation for Rayleigh model using progressive Type-II censoring data. Journal of Statistical Theory and Applications, 16(2), 239–247. https://doi.org/10.2991/jsta.2017.16.2.8

Erto, P., Lanzotti, A., & Lepore, A. (2010). Wind speed parameter estimation from one-month sample via Bayesian approach. Quality and Reliability Engineering International, 26(8), 853–862. https://doi.org/10.1002/qre.1184

Gezer, H., & Usta, I. (2026). Parameter and reliability estimation for the Rayleigh distribution under improved adaptive Type-II progressive censoring scheme with binomial removals. Cumhuriyet Science Journal, 47(1), 182–193. https://doi.org/10.17776/csj.1728252

Han, M. (2009). E-Bayesian estimation and hierarchical Bayesian estimation of failure rate. Applied Mathematical Modelling, 33(4), 1915–1922. https://doi.org/10.1016/j.apm.2008.03.019

Han, M. (2019). E-Bayesian estimation and its E-MSE under the scaled squared error loss function, for exponential distribution as example. Communications in Statistics – Simulation and Computation, 48(6), 1880–1890. https://doi.org/10.1080/03610918.2018.1425444

Han, M. (2020). E-Bayesian estimation and its E-posterior risk of the exponential distribution parameter based on complete and type I censored samples. Communications in Statistics – Theory and Methods, 49(8), 1858–1872. https://doi.org/10.1080/03610926.2019.1565837

Panda, M. K., & Bhoi, L. R. (2025). E-Bayesian estimation of Rayleigh distribution and its evaluation standards: E-posterior risks and E-MSEs under progressive type-II censoring. Austrian Journal of Statistics, 54(4), 82–116. https://doi.org/10.17713/ajs.v54i4.2047

Seguro, J. V., & Lambert, T. W. (2000). Modern estimation of the parameters of the Weibull wind speed distribution for wind energy analysis. Journal of Wind Engineering and Industrial Aerodynamics, 85(1), 75–84. https://doi.org/10.1016/S0167-6105(99)00122-1

Shi, H., Dong, Z., Xiao, N., & Huang, Q. (2021). Wind speed distributions used in wind energy assessment: A review. Frontiers in Energy Research, 9, 769920. https://doi.org/10.3389/fenrg.2021.769920

Stephens, M. A. (1974). EDF statistics for goodness of fit and some comparisons. Journal of the American Statistical Association, 69(347), 730–737. https://doi.org/10.1080/01621459.1974.10480196

Usta, I. (2016). An innovative estimation method regarding Weibull parameters for wind energy applications. Energy, 106, 301–314. https://doi.org/10.1016/j.energy.2016.03.068

Usta, I., Arık, I., Yenilmez, I., & Mert Kantar, Y. (2018). A new estimation approach based on moments for estimating Weibull parameters in wind power applications. Energy Conversion and Management, 164, 570–578. https://doi.org/10.1016/j.enconman.2018.03.033

Effect of Viscous Dissipation on Pulsating Flow and Heat Transfer for Non-Newtonian Fluid in a Pipe

Ayse Nur Altunkaya*

Recep Tayyip Erdogan University, Mechanical Engineering Department, Rize, Türkiye
aysenur.altunkaya@erdogan.edu.tr

Abstract

In this study, a semi-analytical investigation of heat transfer in pulsating flow of non-Newtonian fluid in a pipe with uniform heat flux at the wall, including viscous dissipation effect, is presented. It is assumed that the flow is fully developed both hydrodynamically and thermally. The maximum instantaneous Nusselt number, temperature profiles, and the amplitude and phase angle of the oscillatory Nusselt number response are obtained for pseudoplastic, Newtonian, and dilatant fluids under different values of nondimensional frequency (F), amplitude (ε), and Brinkman number (Br) by considering the power-law model and a series expansion approach based on the perturbation method. The results indicate that F, Br, ε and the power-law index are interactively effective on heat transfer.

Keywords: Pulsating flow, viscous dissipation, power-law fluid, perturbation method, heat transfer

1. Introduction

Pulsating flow and heat transfer are encountered in engineering and biomedical applications where effective thermal management is essential. Although pulsating Newtonian flows have been extensively investigated (Nield and Kuznetsov, 2007; Yin and Ma, 2013; Yuan et al., 2016; Blythman et al., 2019), studies on non-Newtonian fluids remain relatively limited and have mainly focused on hydrodynamic characteristics (Dapra and Scarpi, 2006; Nandakumar et al., 2015; Afrouzi et al., 2019; Yu et al., 2020). Recent studies by our research group investigated pulsating flow and heat transfer of power-law fluids in circular pipes, plane ducts, and annular geometries using perturbation method based on a series expansion (Altunkaya et al., 2023, 2024a, 2024b), demonstrating significant effects of pulsating parameters and the power-law index on flow and heat transfer. However, viscous dissipation, which can modify the temperature field and heat transfer characteristics of power-law fluids, has not been considered in these studies. The present study semi-analytically investigates pulsating heat transfer of a power-law fluid in a circular pipe by accounting for viscous dissipation. A perturbation series method is employed to examine the effects of the dimensionless frequency, amplitude, Brinkman number, and power-law index on the maximum instantaneous Nusselt number, as well as the amplitude and phase of its oscillatory response.

2. Problem Definition and Proposed Method

Pulsating laminar flow of a power-law fluid is studied in circular pipe held at uniform heat flux, considering the effect of viscous dissipation, as shown in Figure 1.

* *Corresponding Author*

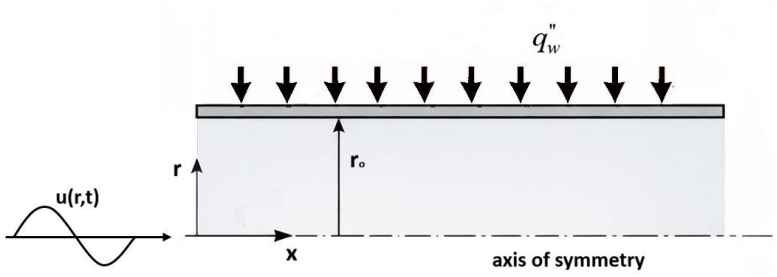


Figure 1. The schematic of the problem geometry

The flow is driven by the pressure gradient $-\partial p/\partial x = P_0(1+\varepsilon e^{i\omega t})$, that oscillates with time, where P_0 is the pressure gradient, ε is the dimensionless amplitude, ω is the angular frequency, and t is the time. The shear stress is $\tau_{rx} = \eta\left(-\partial u/\partial r\right)^n$ for power-law fluid, where u is the axial velocity, r is the radial coordinate, η is the consistency index of the fluid and n is the power-law index. The steady (U_0) and oscillating (U_1) component of the dimensionless velocity $U\left(=u/\bar{u}_0,\ \ \bar{u}_0=(n/(3n+1))\left((P_0\, r_o^{n+1})/2\eta\right)^{\frac{1}{n}}\right)$ are obtained as (see details in Altunkaya et al., 2023)

$$U_0(\mathrm{R}) = \frac{3n+1}{n+1}\left[1-R^{\frac{n+1}{n}}\right],\ U_1(\mathrm{R}) = -\frac{2i\left(6+\frac{2}{n}\right)^n}{F}\left[1-\frac{R^{\frac{1-n}{2n}}J_v\left[icR^{\frac{1+n}{2n}}\right]}{J_v\left[ic\right]}\right];\ v=\frac{n-1}{1+n},\ c^2=\frac{4Fi(1+3n)}{(1+\mathrm{n})^2}\left(\frac{n}{2+6n}\right)^n \quad (1)$$

where $R\ (=r/r_o)$ is the dimensionless radial coordinate, r_o is the radius of the pipe, F is the dimensionless frequency $\left(=\mathrm{Re}\, r_o\omega/\bar{u}_0,\ \ \mathrm{Re}=\rho\bar{u}_0^{\,2-n}\,\mathrm{D}_h^{\,n}/\eta\right)$, Re is the Reynolds number, $D_h\ (=2r_o)$ is the hydraulic diameter, ρ is the fluid density. The governing equation of energy can be written as

$$\frac{\partial T}{\partial t}+u\frac{\partial T}{\partial x}=\alpha\frac{1}{r}\frac{\partial}{\partial r}\left(r\frac{\partial T}{\partial r}\right)+\frac{\tau_{rx}}{\rho c_p}\left(-\frac{\partial u}{\partial r}\right);\qquad \frac{\partial T}{\partial x}=\left(1+2\frac{\eta\bar{u}_0^{n+1}}{2q_w''r_o^n}\left(\frac{3n+1}{n}\right)^n\right)\frac{2q_w''}{\rho c_p\bar{u}(\mathrm{t})\,\mathrm{r_o}} \quad (2)$$

where T, c_p, and α are the temperature, specific heat at constant pressure, and thermal diffusivity, respectively, and the second term in the right-hand side represents the viscous dissipation term. By introducing dimensionless temperature $\theta\ \left(=(T-T_w)/((q_w''D_h)/k)\right)$, the Brinkman number Br $\left(=\eta\bar{u}_0^{n+1}/2q_w''r_o^n\right)$ and the Prandtl number $Pr\left(=(\eta c_p/k)\left(\bar{u}_0/r_o\right)^{n-1}\right)$, Eq. (2) is rearranged as follows

$$\frac{F\,\mathrm{Pr}}{2^n}\frac{\partial\theta}{\partial t^*}+\left(1+2Br\left(\frac{3n+1}{n}\right)^n\right)\frac{U(\mathrm{R},t^*)}{\bar{U}(t^*)}=\frac{1}{R}\frac{\partial}{\partial R}\left(R\frac{\partial\theta}{\partial R}\right)+Br\left(-\frac{\partial U}{\partial R}\right)^{n+1} \quad (3)$$

where $t^*(=\omega t)$ is the dimensionless period of oscillation, $\bar{U}(t^*)\left(=1+\varepsilon\beta e^{it^*}\right)$ is the spatial average of $U(R,t^*)$. For the solution of Eq. (3), the corresponding boundary conditions can be written as

$$R=0:\ \ \partial\theta/\partial R=0,\ \ R=1:\ \ \theta=0 \quad (4)$$

The perturbation solution is

$$\theta(R,t^*)=\theta_0(R)+\varepsilon\theta_1(R)\,\mathrm{e}^{it^*}+O(\varepsilon^2) \quad (5)$$

Here, higher-order terms are neglected under the assumption of sufficiently small pulsating amplitudes. The physical quantities are obtained by taking the real parts of the corresponding complex expressions. The second term right-hand side in Eq. (3) using binomial expansion can be written as follows:

$$\left(-\frac{\partial U}{\partial R}\right)^{n+1}=\left(-\frac{dU_0}{dR}\right)^{n+1}-\varepsilon(n+1)\left(-\frac{dU_0}{dR}\right)^{n}\frac{dU_1}{dR}e^{it^*}+O(\varepsilon^2) \tag{6}$$

By substituting Eqs. (5) and (6) into Eq. (3) and equating powers of ε, following equations are expressed as

$$\frac{1}{R}\frac{d}{dR}\left(R\frac{d\theta_0}{dR}\right)=U_0^*+Br\left(2\left(\frac{3n+1}{n}\right)^n U_0^*-\left(-\frac{dU_0}{dR}\right)^{n+1}\right) \tag{7a}$$

$$\frac{1}{R}\frac{d}{dR}\left(R\frac{d\theta_1}{dR}\right)-\frac{F\,\mathrm{Pr}}{2^n}i\theta_1=\Gamma(R),\qquad \Gamma(R)=U_1^*+Br\left(2\left(\frac{3n+1}{n}\right)^n U_1^*+(n+1)\left(-\frac{dU_0}{dR}\right)^{n}\frac{dU_1}{dR}\right) \tag{7b}$$

where $U_0^*(\mathrm{R})$ and $U_1^*(\mathrm{R})$ are the components of the ratio of dimensionless velocity to $\bar{U}(t^*)$, which is determined from

$$U_0^*(\mathrm{R})=U_0(\mathrm{R}),\quad U_1^*(\mathrm{R})=-\beta U_0^*(\mathrm{R})+\mathrm{U}_1(\mathrm{R});\qquad \beta=-\frac{2i\left(6+\frac{2}{n}\right)^n}{F}\left[1-\frac{4nI_{v+1}[c]}{c(1+\mathrm{n})I_v[c]}\right] \tag{8}$$

When viscous dissipation is eliminated ($Br = 0$) from Eq. (3), it is seen that it agrees with the results obtained in our previous studies (Altunkaya et al., 2023). If viscous dissipation is included ($Br \neq 0$), the solution of Eqs. (7a) and (7b) can be obtained as

$$\theta_0(R)=-\frac{1+5n+2Br\left(3+\frac{1}{n}\right)^n\left(1+n\left(3+2R^{3+\frac{1}{n}}\right)\right)}{4(1+3n)}-\frac{\left(1+2Br\left(3+\frac{1}{n}\right)^n\right)R^2\left(-1+n\left(-6+n\left(-9+4R^{1+\frac{1}{n}}\right)\right)\right)}{4(1+3n)(1+n)} \tag{9}$$

However, Eq. (7b) is solved using Green's function approach. Boundary value problems involving non-homogeneous ordinary differential equations are solved effectively with this function.

$$\theta_1(R)=J_0(AR)\left(I_1(R)+I_3(R)\right)+Y_0(AR)I_2(R) \tag{10}$$

where

$$\begin{aligned}&\mathrm{A}^2=-\frac{F\,\mathrm{Pr}\,i}{2^n},\qquad I_1(\mathrm{R})=\int_0^R-\frac{\pi}{2}\frac{J_0(\mathrm{A}\,\xi)\,\mathrm{Y}_0(\mathrm{A})}{J_0(\mathrm{A})}\xi\,\Gamma(\xi)\,\mathrm{d}\,\xi,\\ &I_2(\mathrm{R})=\int_0^R\frac{\pi}{2}J_0(\mathrm{A}\,\xi)\xi\Gamma(\xi)\,\mathrm{d}\,\xi,\quad I_3(\mathrm{R})=\int_R^1-\frac{\pi}{2}\left(\frac{J_0(\mathrm{A}\,\xi)\,\mathrm{Y}_0(\mathrm{A})-J_0(\mathrm{A})\,\mathrm{Y}_0(\mathrm{A}\,\xi)}{J_0(\mathrm{A})}\right)\xi\Gamma(\xi)\,\mathrm{d}\,\xi\end{aligned} \tag{11}$$

The first-order dimensionless bulk temperature θ_b is given in the form as

$$\theta_b=\frac{T_b-T_w}{\frac{q_w''D_h}{k}}=\frac{\int_0^1 U\theta R\,dR}{\int_0^1 UR\,dR}\quad\rightarrow\quad\theta_b=\frac{\int_0^1(U_0\theta_0+\varepsilon(U_0\theta_1+U_1\theta_0)\,\mathrm{e}^{it^*})R\,dR}{\frac{1}{2}(1+\varepsilon\beta\,\mathrm{e}^{it^*})} \tag{12}$$

The Nusselt number can be expressed in the form as follows to determine the effect of oscillating flow on heat transfer rate:

$$Nu = \frac{hD_h}{k} = \frac{1}{\dfrac{T_w - T_b}{\dfrac{q_w'' D_h}{k}}} = Nu_0 + \varepsilon Nu_1 e^{it^*} + O(\varepsilon^2);$$

$$Nu_0 = -\frac{1/2}{\int_0^1 U_0\theta_0 R dR}, \quad Nu_1 = -\frac{(\beta/2) + Nu_0 \int_0^1 (U_0\theta_1 + U_1\theta_0) R dR}{\int_0^1 U_0\theta_0 R dR} \tag{13}$$

where Nu_o and Nu_1 denote the steady and complex oscillatory components of the Nusselt number, respectively. Eq. (13) is used to determine the maximum instantaneous Nusselt number over a period, which is expressed as

$$Nu_{\max} = Nu_0 + \varepsilon |Nu_1| \tag{14}$$

Furthermore, the normalized amplitude and phase angle of the oscillatory Nusselt number are obtained as

$$A_{Nu} = \left| \frac{Nu_1}{Nu_0} \right| \tag{15a}$$

$$\phi_{Nu} = \arg\left(\frac{Nu_1}{Nu_0} \right) \tag{15b}$$

respectively. These quantities characterize the relative magnitude and phase shift of the oscillatory Nusselt number response with respect to the imposed pressure pulsation.

3. Results and Discussion

Heat transfer in a circular pipe for laminar pulsating flow is examined by considering viscous dissipation effect and power-law model. The present results are validated against the results of Shojaeian et al. (2015) for non-Newtonian fluids. As shown in Figure 2, good agreement is observed between the present results and those reported by Shojaeian et al. (2015) for the variation of the Nusselt number with the Brinkman number.

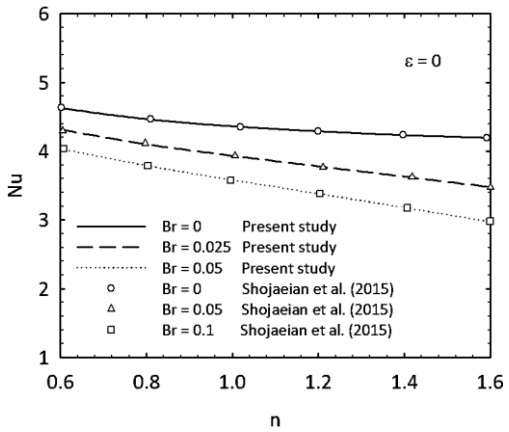


Figure 2. The comparison of the results with Shojaeian et al. (2015) for circular pipe

To understand the effects of F and Br on heat transfer, dimensionless bulk temperatures are plotted first. Figure 3 illustrates the change in θ_b over a period for pseudoplastic fluid (n = 0.6), Newtonian fluid (n = 1) and dilatant fluid (n = 1.2), respectively, at different values of F and Br. Increasing Br shifts θ_b toward more negative values, indicating a decrease in the temperature difference (T_b - T_w) according to Eq. (12). This behavior results from viscous heat generation near the wall, which increases the wall temperature. Furthermore, as Br increases, the maximum oscillation amplitude for all three fluid types occurs at lower frequencies, which is attributed to the dominance of viscous forces at low frequencies.

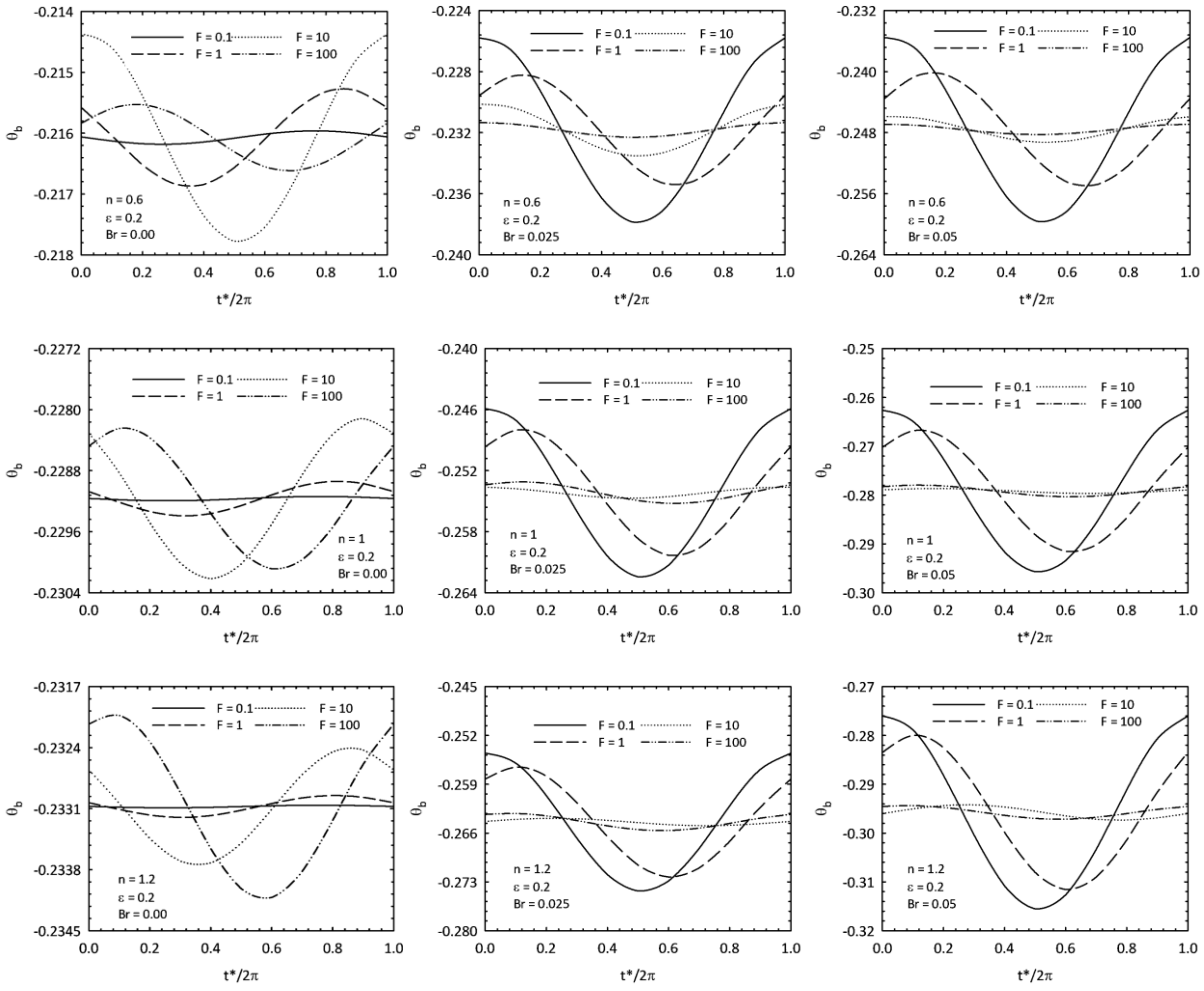
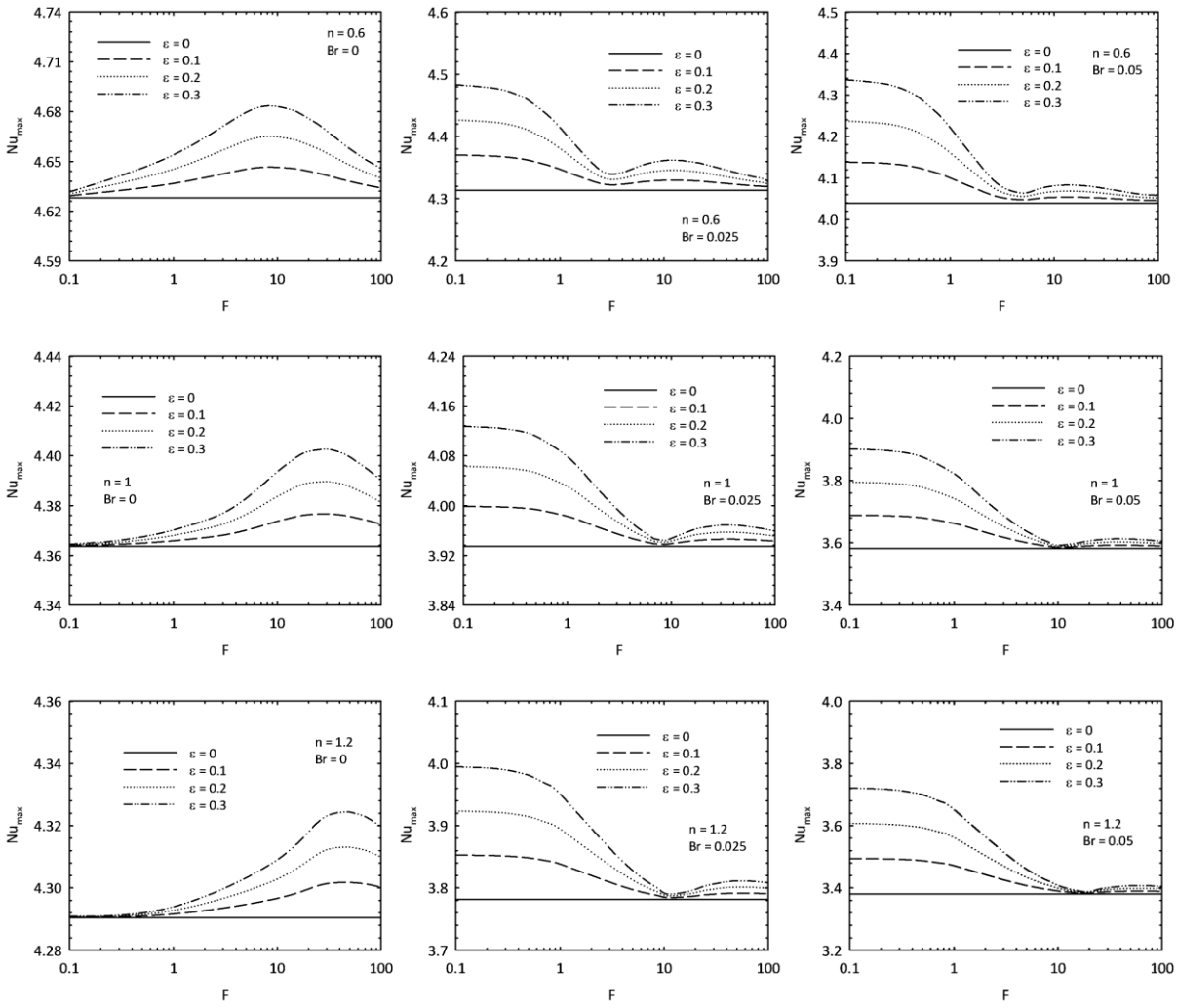


Figure 3. Variation of θ_b over a period for n = 0.6, 1 and 1.2 at Pr = 10; Br = 0.00 (a), Br = 0.025 (b), and Br = 0.05 (c)

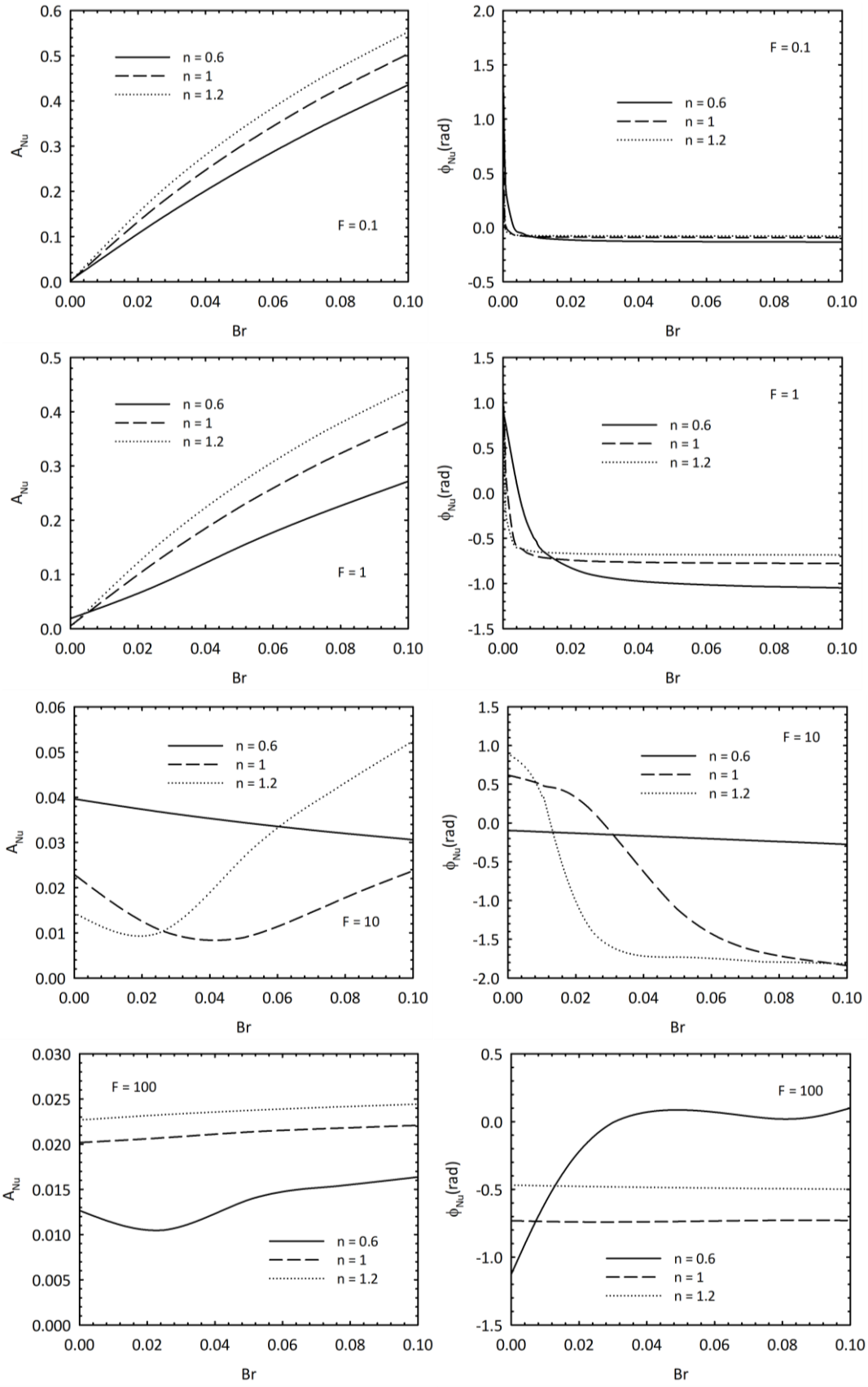
The variation in the maximum instantaneous Nusselt number (Nu_{max}), obtained over a period, as a function of F at different Br values is presented in Figure 4, respectively. For all fluid types, Nu_{max} increases with ε, whereas increasing Br decreases Nu_{max} due to increased viscous heating near the wall, which increases (T_w -T_b) according to Eq. (13). At Br =0, Nu_{max} reaches a maximum at intermediate frequencies; with increasing Br, the highest values of Nu_{max} shift toward lower frequencies. This behavior is associated with the frequency-dependent variation of the bulk temperature. Furthermore, Nu_{max} decreases with increasing power-law index while for Br>0, the minimum Nu_{max} shifts toward higher frequencies.



(a) (b) (c)

Figure 4. Variation of the Nu_{max} with F for n = 0.6, 1, and 1.2 at Pr = 10; Br = 0.00 (a), Br = 0.025 (b), and Br = 0.05 (c)

Figure 5 shows the variation of the normalized amplitude and phase angle of the oscillatory Nusselt number with the Brinkman number at different dimensionless frequencies. As shown in Figure 5a, the normalized amplitude increases with the Brinkman number for all three fluid behaviors at low frequencies (F = 0.1 and 1), with the dilatant fluid exhibiting the highest values. However, at F = 10, the amplitude exhibits different trends depending on the power-law index, while at F = 100, its magnitude is considerably reduced, and its variation with increasing Brinkman number becomes negligible. In contrast, Figure 5b shows that the phase angle generally decreases with increasing Brinkman number at low and intermediate frequencies, changing from positive to negative values and indicating a phase lag relative to the imposed pressure pulsation. At higher frequencies, the phase response becomes more dependent on fluid rheology.



(a) (b)

Figure 5. Variation of normalized amplitude (a) and phase angle (b) of the oscillatory Nusselt number with *Br* for different values of *n*

4. Conclusions

A semi-analytical study is conducted on heat transfer in power-law fluids under fully developed laminar pulsating flow in a circular pipe, accounting for viscous dissipation. Increasing the Brinkman number decreases the maximum instantaneous Nusselt number and shifts its highest values to lower frequencies. The Nu_{max} also decreases with increasing power-law index. Furthermore, the normalized Nusselt amplitude increases with the Brinkman number at low frequencies, particularly for dilatant fluids, whereas it diminishes at high frequencies. The phase angle generally shifts from positive to negative values with increasing Brinkman number, indicating a phase lag.

References

Afrouzi, H. H., Ahmadian, M., Moshfegh, A., Toghraie, D., & Javadzadegan, A. (2019). Statistical analysis of pulsating non-Newtonian flow in a corrugated channel using Lattice-Boltzmann method. *Physica A*, 535, 122486. https://doi.org/10.1016/j.physa.2019.122486

Altunkaya, A. N., Aydin, O., & Avci, M. (2023). Pulsating flow and heat transfer of power-law fluid in a circular pipe. *Nonlinear Analysis: Modelling and Control*, 28(1), 56-73. https://doi.org/10.15388/namc.2023.28.29734

Altunkaya, A. N., Aydin, O., & Avci, M. (2024a). Non-Newtonian laminar pulsating heat and fluid flow in plane duct. *Heat Transfer*, 53(2), 805–825. https://doi.org/10.1002/htj.22976

Altunkaya, A. N., Aydin, O., & Avci, M. (2024b). Pulsating non-Newtonian heat and fluid flow in a concentric annular duct: An analysis using perturbation series method. *International Communications in Heat and Mass Transfer*, 154, 107417. https://doi.org/10.1016/j.icheatmasstransfer.2024.107417

Blythman, R., Persoons, T., Jeffers, N., & Murray, D. B. (2019). Heat transfer of laminar pulsating flow in a rectangular channel. *International Journal of Heat and Mass Transfer*, 128, 279–289. https://doi.org/10.1016/j.ijheatmasstransfer.2018.08.109

Daprà, I., & Scarpi, G. (2006). Pulsatile pipe flow of pseudoplastic fluids. *Meccanica*, 41, 501–508. https://doi.org/10.1007/s11012-006-0007-6

Nandakumar, N., Sahu, K. C., & Anand, M. (2015). Pulsatile flow of a shear-thinning model for blood through a two-dimensional stenosed channel. *European Journal of Mechanics–B/Fluids*, 49, 29–35. https://doi.org/10.1016/j.euromechflu.2014.07.005

Nield, D. A., & Kuznetsov, A. V. (2007). Forced convection with laminar pulsating flow in a channel or tube. *International Journal of Thermal Sciences*, 46, 551–560. https://doi.org/10.1016/j.ijthermalsci.2006.07.011

Shojaeian, M., Yildiz, M., & Koşar, A. (2015). Convective heat transfer and second law analysis of non-Newtonian fluid flows with variable thermophysical properties in circular channels. *International Communications in Heat and Mass Transfer*, 60, 21–31. https://doi.org/10.1016/j.icheatmasstransfer.2014.12.002

Yin, D., & Ma, H. B. (2013). Analytical solution of oscillating flow in a capillary tube. *International Journal of Heat and Mass Transfer*, 66, 699–705. https://doi.org/10.1016/j.ijheatmasstransfer.2013.07.073

Yu, L., Bian, Y., Liu, Y., & Xu, X. (2020). Experimental analysis on fluid flow and mass transfer characteristics of CMC solutions in wavy-walled tubes for steady and pulsating flow by PIV. *Applied Thermal Engineering*, 171, 115098. https://doi.org/10.1016/j.applthermaleng.2020.115098

Yuan, H., Tan, S., Wen, J., & Zhuang, N. (2016). Heat transfer of pulsating laminar flow in pipes with wall thermal inertia. *International Journal of Thermal Sciences*, 99, 152–160. https://doi.org/10.1016/j.ijthermalsci.2015.08.014

Solutions of 3D MHD Equations using Different Variants of Differential Quadrature Method

Selçuk Han Aydın*
Karadeniz Technical University, Department of Mathematics, Trabzon, Türkiye
shaydin@ktu.edu.tr

Abstract

It is known that the Differential Quadrature Method (DQM) is well known and mostly used numerical scheme due to the it's simple formulation and computational efficiency. Even the method is firstly proposed by Bellman for the rapid solution of nonlinear partial differential equations using polynomial based approximation, many authors considered and developed the different version of the method such as Chebyshev-Gauss-Lobatto points approximation, Fourier series expansion based approximation, cubic-modified cubic-quadratic-quartic B-spline based approximations (and some others) in order to simulate the many problems in engineering and physical sciences. In the first part of this study, we compared some of well-known these approaches in terms of L_2 norm and maximum norm over different test problems having exact solutions. Then we extended these numerical schemes in order to obtain the approximated solution of both 2D and 3D MagnetoHydroDynamic (MHD) duct equations defined on square and cubic domains, respectively. Obtained solutions are displayed in terms of a table and figures, and compared with the previous literature results.

Keywords: DQM, MHD, 3D

1. Introduction

Differential Quadrature Method (DQM) is one of the most popular numerical method which was firstly introduced by Bellman in 1972 (Bellman et al., 1972, 1975). It is one of the most efficient and easiest (in the sense of implementation) numerical method to solve ordinary or partial differential equations. Due to its popularity, different versions of DQM (polynomial based, Fourier expansion based, Cosine expansion based, Legendre polynomials based, Chebyshev-Gauss-Lobotto points approximations, Spline, B-spline, cubic B-splines, modified cubic B-spline, quadratic-quartic B-spline, etc.) have been developed by many researchers.

Hartmann firstly investigated the MagnetoHydroDynamic(MHD) flow of viscous, incompressible flow between two plates. The MHD flow has many important applications in different area in engineering and biomedical applications as MHD generators, MHD pumps,flow meters for measuring the blood pressure. Therefore, MHD has great importance for the researchers. However, due to the coupled partial differential equations, most the solutions are obtained using some numerical methods. In this study, we consider the MHD flow of an electrically conducting fluid in 2D or 3D domains in the direction of external magnetic field of intensity B_0 with different angles using DQM.

2. Problem Definition

MagnetoHydroDynamic (MHD) equations are obtained from Navier-Stokes equations of continuum mechanics and Maxwell's equations of electromagnetic field through Ohm's law which as coupled system of governing partial differential equations. The fluid is flowing through the pipe due to a pressure gradient. Then, MHD equations are written as (Hartmann, 1937; Shercliff, 1956)

* *Corresponding Author*

$$\begin{aligned} \nabla^2 V + \boldsymbol{M}\cdot\nabla B &= -1 \\ \nabla^2 B + \boldsymbol{M}\cdot\nabla V &= 0 \end{aligned} \tag{1}$$

on the domain $\Omega \subseteq \mathbb{R}^n$ $(n = 2, 3)$ for the Hartmann number Ha which is defined in terms of characteristic length L, dynamic viscosity η, electric conductivity parameter σ and intensity of the externally applied magnetic field B_0 as $Ha = B_0 L\sqrt{\frac{\sigma}{\eta}}$ and with the boundary conditions $V=B=0$ on $\Gamma=\partial\Omega$. The constant vector $\boldsymbol{M}$ is defined in 2D case as $\boldsymbol{M} = \begin{bmatrix} M_x \\ M_y \end{bmatrix} = \begin{bmatrix} Ha\ \cos(\alpha) \\ Ha\ \sin(\alpha) \end{bmatrix}$ and for 3D case as $\boldsymbol{M} = \begin{bmatrix} M_x \\ M_y \\ M_z \end{bmatrix} = \begin{bmatrix} Ha\ \cos(\alpha)\ \sin(\beta) \\ Ha\ \sin(\alpha)\ \sin(\beta) \\ Ha\ \cos(\beta) \end{bmatrix}$

where α and β are the direction angles of the B_0 with x-axis and z-axis, respectively.

3. Proposed Method

The idea of the DQM (Chang, 2000) is an approximation to a derivative of a function at a certain discrete points $x_1 < x_2 < \cdots < x_N$ using the linear sum of the functional values at certain discrete points such that $U_x(x_i) = \sum_{j=1}^{N} w_{ij}^{(1)} U(x_j) = \sum_{j=1}^{N} a_{ij} U(x_j)$ and $U_{xx}(x_i) = \sum_{j=1}^{N} w_{ij}^{(2)} U(x_j) = \sum_{j=1}^{N} b_{ij} U(x_j)$, in general for the r$^{\text{th}}$ order derivative $U_x^{(r)}(x_i) = \sum_{j=1}^{N} w_{ij}^{(r)} U(x_j)$.

In Shu's general approach the discretization points are selected uniformly. However, for the Chebyshev approach the location of the points are $x_i = a + (b-a)(1-\cos(\pi(i-1)/(N-1)))/2,\ i = 1\cdots N$ on the interval $[a,b]$. Then the derivative coefficients are calculated as

$$a_{ij} = \frac{M^{(1)}(x_i)}{(x_i - x_j) M^{(1)}(x_j)} \text{ and } b_{ij} = 2a_{ij}\left(a_{ij} - \frac{1}{x_i - x_j}\right), i \neq j;\ \ a_{ii} = -\sum_{i=1, i\neq j}^{N} a_{ij} \text{ and } b_{ii} - \sum_{i=1, i\neq j}^{N} b_{ij} \tag{2}$$

where $M^{(1)}(x_i) = \prod_{k=1, k\neq i}^{N} (x_i - x_k)$.

In Fourier based approach (Meirikim & Roshan., 2024)

$$a_{ij} = \frac{\pi}{2(b-a)} \frac{G^{(1)}(x_i)}{\sin\left(\frac{\pi(x_i - x_j)}{2(b-a)}\right) G^{(1)}(x_j)},\ b_{ij} = a_{ij}\left(2a_{ij} - \frac{\pi}{(b-a)} \cot\left(\frac{\pi(x_i - x_j)}{2(b-a)}\right)\right),\ \text{for } i \neq j \tag{3}$$

Finally, cubic B-spline coefficients are calculated using the following systems given as (Korkmaz & Dağ, 2012)

$$\begin{bmatrix} 3 & 0 & -3 & & & & \\ 1 & 4 & 1 & & & & \\ & 1 & 4 & 1 & & & \\ & & \ddots & \ddots & \ddots & & \\ & & & 1 & 4 & 1 & \\ & & & & 1 & 4 & 1 \\ & & & & 3 & 0 & -3 \end{bmatrix} \begin{bmatrix} a_{1,-1} \\ a_{1,0} \\ \vdots \\ a_{1,N} \\ a_{1,N+1} \end{bmatrix} = \begin{bmatrix} 6/h \\ -3/h \\ 0 \\ 3/h \\ 0 \\ \vdots \\ 0 \end{bmatrix}, \quad [A] \begin{bmatrix} a_{N,-1} \\ a_{N,0} \\ \vdots \\ a_{N,N} \\ a_{N,N+1} \end{bmatrix} = \begin{bmatrix} 0 \\ \vdots \\ 0 \\ -3/h \\ 0 \\ 3/h \\ 6/h \end{bmatrix} \tag{4}$$

$$[A] \begin{bmatrix} a_{2,-1} \\ a_{2,0} \\ \vdots \\ a_{2,N} \\ a_{2,N+1} \end{bmatrix} = \begin{bmatrix} 0 \\ 0 \\ -3/h \\ 0 \\ 3/h \\ 0 \\ \vdots \\ 0 \end{bmatrix}, \quad [A] \begin{bmatrix} a_{3,-1} \\ a_{3,0} \\ \vdots \\ a_{3,N} \\ a_{3,N+1} \end{bmatrix} = \begin{bmatrix} 0 \\ 0 \\ 0 \\ -3/h \\ 0 \\ 3/h \\ 0 \\ \vdots \\ 0 \end{bmatrix}, \cdots, [A] \begin{bmatrix} a_{N-1,-1} \\ a_{N-1,0} \\ \vdots \\ a_{N-1,N} \\ a_{N-1,N+1} \end{bmatrix} = \begin{bmatrix} 0 \\ \vdots \\ 0 \\ -3/h \\ 0 \\ 3/h \\ 0 \\ 0 \end{bmatrix} \tag{5}$$

and similarly, the modified cubic B-spline functions (Geeta & Brajesh., 2013) as

$$\begin{bmatrix} 6 & 1 & & & & & \\ 0 & 4 & 1 & & & & \\ & 1 & 4 & 1 & & & \\ & & \ddots & \ddots & \ddots & & \\ & & & 1 & 4 & 1 & \\ & & & & 1 & 4 & 0 \\ & & & & & 1 & 6 \end{bmatrix} \begin{bmatrix} a_{1,1} \\ a_{1,2} \\ \vdots \\ a_{1,N-1} \\ a_{1,N} \end{bmatrix} = \begin{bmatrix} -6/h \\ 6/h \\ 0 \\ \vdots \\ 0 \\ 0 \end{bmatrix}, \quad [A] \begin{bmatrix} a_{N,1} \\ a_{N,2} \\ \vdots \\ a_{N,N-1} \\ a_{N,N} \end{bmatrix} = \begin{bmatrix} 0 \\ \vdots \\ 0 \\ -6/h \\ 6/h \end{bmatrix} \tag{6}$$

$$[A] \begin{bmatrix} a_{2,1} \\ a_{2,2} \\ \vdots \\ a_{2,N-1} \\ a_{2,N} \end{bmatrix} = \begin{bmatrix} -3/h \\ 0 \\ 3/h \\ 0 \\ \vdots \\ 0 \end{bmatrix}, \quad [A] \begin{bmatrix} a_{3,1} \\ a_{3,2} \\ \vdots \\ a_{3,N-1} \\ a_{3,N} \end{bmatrix} = \begin{bmatrix} 0 \\ -3/h \\ 0 \\ 3/h \\ 0 \\ \vdots \\ 0 \end{bmatrix}, \cdots, [A] \begin{bmatrix} a_{N-1,1} \\ a_{N-1,1} \\ \vdots \\ a_{N-1,N-1} \\ a_{N-1,N} \end{bmatrix} = \begin{bmatrix} 0 \\ \vdots \\ 0 \\ -3/h \\ 0 \\ 3/h \end{bmatrix} \tag{7}$$

4. Results and Discussion

In this section, we will perform some numerical test in order to compare and indicate the accuracy of the proposed variants of the DQM. We compared the exact solution and numerical results for the

different approaches in terms of L_2 norm (as average) as $\| L_2 \| = \frac{1}{N}\left[\sum_{i=1}^{N}\left(u_e(x_i)-u_n(x_i)\right)^2\right]^{1/2}$ and maximum absolute error as $|Error|_{\max} = \max|u_e(x_i)-u_n(x_i)|,\ 1 \le i \le N$ where N is the total number of discretization points and, $u_e(x_i)$ and $u_n(x_i)$ are the exact and numerical results, respectively.

4.1. Test problem 1

As a first test problem, we consider a second order non-homogenous ODE $-(1+x)u''-u=-x^2-3,\ 0 \le x \le 1$ having exact solution $u(x)=x^2-2x+1$ with boundary conditions either $u(0)=1, u(1)=0$ or $u'(0)=-2, u(1)=0$.

Table 1. Comparison of different approaches for the Test Problem 1

Method (N=11)	Dirichlet BC		Neumann BC	
	$\| L_2 \|$ norm	|Error max|	$\| L_2 \|$ norm	|Error max|
Shu's approach	2.16×10^{-16}	1.88×10^{-15}	9.14×10^{-14}	4.87×10^{-13}
Chebyshev	8.51×10^{-17}	5.55×10^{-16}	7.79×10^{-15}	3.95×10^{-14}
Fourier	5.85×10^{-6}	3.19×10^{-5}	2.35×10^{-4}	1.22×10^{-3}
Cubic B-spline	6.30×10^{-3}	4.03×10^{-2}	2.23×10^{-1}	1.22×10^{0}
Modified cubic	1.96×10^{-4}	7.46×10^{-4}	1.66×10^{-2}	8.82×10^{-2}

It is seen that from Table 1 that the accurate version of DQM is Chebyshev one and Dirichlet type boundary condition cases give more efficient results compared to Neumann one due the imposing of the derivative boundary conditions also numerically.

4.2. Test problem 2

In the second test problem, we take a constant coefficient homogenous differential equation $u''-2u'-3u=0,\ 0 \le x \le 1$. Similar to the previous case we consider both Dirichlet and Neumann type boundary conditions taken from the exact solution $u(x)=2e^{3x}-e^{-x}$. Noticed that the previous case comments are also valid for this test problem (see Table 2).

Table 2. Comparison of different approaches for the Test Problem 2

Method (N=11)	Dirichlet BC		Neumann BC	
	$\| L_2 \|$ norm	|Error max|	$\| L_2 \|$ norm	|Error max|
Shu's approach	1.36×10^{-7}	8.15×10^{-7}	7.03×10^{-6}	3.81×10^{-5}
Chebyshev	1.46×10^{-9}	8.80×10^{-9}	1.50×10^{-7}	7.96×10^{-7}
Fourier	5.00×10^{-4}	3.45×10^{-3}	1.11×10^{-2}	5.87×10^{-2}
Cubic B-spline	1.46×10^{-1}	1.25×10^{0}	1.50×10^{-1}	1.20×10^{0}
Modified cubic	1.26×10^{-2}	8.96×10^{-2}	1.05×10^{-1}	5.43×10^{-1}

4.3. 2D and 3D Laplace equations

Another benchmark test is performed for the 2D and 3D versions of the Laplace equation and results are displayed in Table 3 and Table 4, respectively. The mesh is uniform (11 nodes on each directions) and for the Neumann BC case, $\frac{\partial u}{\partial n}$ is specified on all boundaries except the top ones.

Table 3. Comparison of different approaches for the 2D Laplace Equation

Method (N=M=11)	Dirichlet BC		Neumann BC	
	$\|\| L_2 \|\|$ norm	|Error max|	$\|\| L_2 \|\|$ norm	|Error max|
Shu's approach	2.98×10^{-12}	7.40×10^{-11}	1.68×10^{-10}	4.05×10^{-9}
Chebyshev	3.19×10^{-14}	1.12×10^{-12}	3.52×10^{-12}	8.07×10^{-11}
Fourier	2.98×10^{-6}	1.16×10^{-4}	8.35×10^{-5}	1.65×10^{-3}
Cubic B-spline	1.44×10^{-3}	5.82×10^{-2}	5.51×10^{-2}	3.46×10^{0}
Modified cubic	3.12×10^{-5}	1.21×10^{-3}	1.97×10^{-3}	4.23×10^{-2}

Table 4. Comparison of different approaches for the 3D Laplace Equation

Method (N=M=L=11)	Dirichlet BC		Neumann BC	
	$\|\| L_2 \|\|$ norm	|Error max|	$\|\| L_2 \|\|$ norm	|Error max|
Shu's approach	3.33×10^{-11}	2.33×10^{-9}	2.15×10^{-9}	3.85×10^{-8}
Chebyshev	5.42×10^{-14}	1.02×10^{-12}	1.06×10^{-11}	7.61×10^{-11}
Fourier	1.37×10^{-5}	3.28×10^{-4}	3.58×10^{-4}	1.97×10^{-3}
Cubic B-spline	7.36×10^{-3}	1.16×10^{-1}	8.96×10^{-1}	2.76×10^{1}
Modified cubic	1.08×10^{-4}	1.48×10^{-3}	2.41×10^{-2}	1.55×10^{-1}

From the tables, one can conclude that DQM method gives accurate results even in 3D case especially Chebyshev and Shu's approach.

4.4. MHD Equations

Finally we solved the 2D and 3D versions of the MHD problems using the considered versions of DQM. Noticed that in 2D, $\alpha=\pi/2$ case has an exact solutions.

Table 5. Comparison of different approaches for the MHD Problem 2-D case for Ha=100 and $\alpha=\pi/2$.

Method (N=M=11)	Dirichlet BC		Neumann BC	
	$\|\| L_2 \|\|$ norm	|Error max|	$\|\| L_2 \|\|$ norm	|Error max|
Shu's approach	5.59×10^{-4}	1.51×10^{-2}	1.72×10^{-5}	1.26×10^{-3}
Chebyshev	3.46×10^{-5}	1.33×10^{-3}	9.03×10^{-7}	6.29×10^{-5}
Fourier	2.67×10^{-4}	1.44×10^{-2}	1.59×10^{-6}	9.51×10^{-5}
Cubic B-spline	8.67×10^{-5}	3.57×10^{-3}	7.48×10^{-5}	3.48×10^{-3}
Modified cubic	5.86×10^{-5}	2.65×10^{-3}	4.97×10^{-5}	2.31×10^{-3}

In Table 5, we obtained numerical solutions for Ha=100. Noticed the numerical method gives very accurate results even for large values of the Hartmann number.

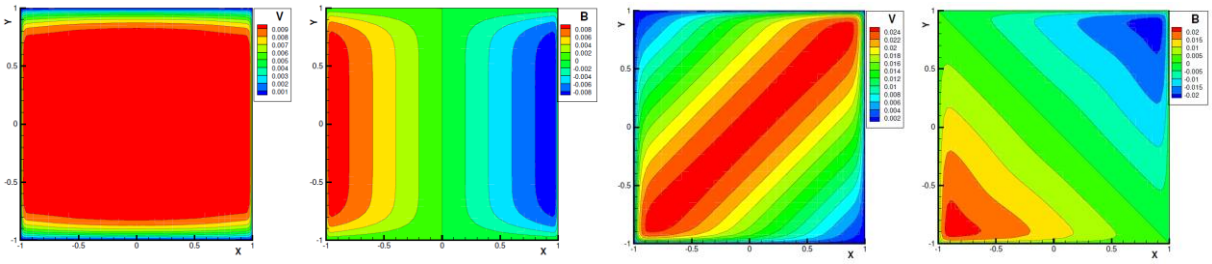


Figure 1. Velocity and induced magnetic 2D case for Ha=100(left), α=π/2 and Ha=50, α=π/4 (right)

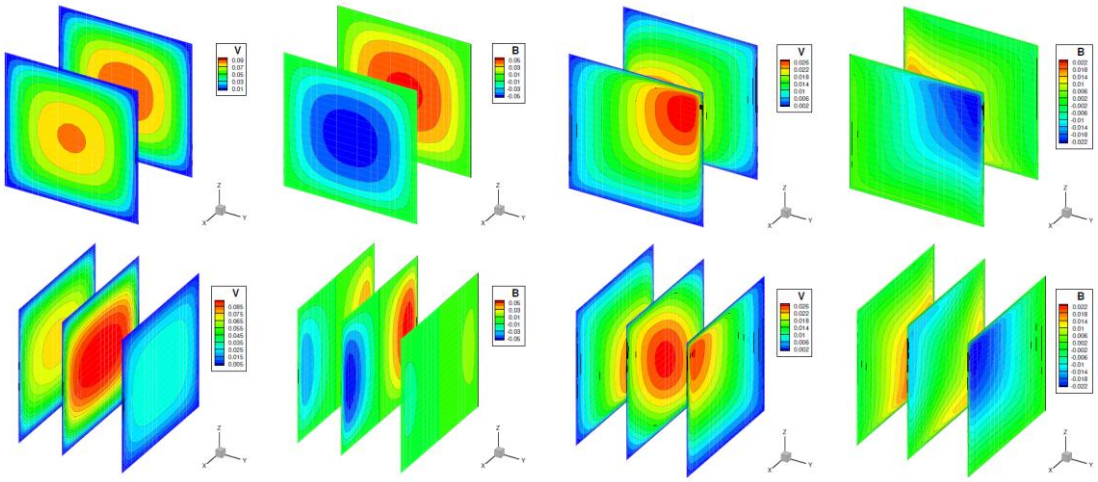


Figure 2. Velocity and induced magnetic contour lines for Ha=10, α=β=π/2 (left) and Ha=50, α=π/2, β=π/3 (right)

Finally, we displayed the obtained solutions in terms of contour lines in 2D case of the problem and 2D slices of 3D case for different values of the Hartmann number and different direction of the externally applied external magnetic field. It is seen that the graphs are smooth, display the well-known behaviors of the MHD flow problem and they are in good aggreement with the previous literature results in the sense of maximum and minimum values V and B (Tezer-Sezgin, 2004; Aydin & Erdoğan, 2023).

5. Conclusion

In the present study, we considered the different variants of the DQM solution to some test problems and MHD flow problem both in 2D and 3D cases. The comparison of the versions are displayed in terms of tables over some test problems. For the MHD flow problem, different flow behaviors are obtained for the different angles of the applied external magnetic field. The simulated solutions visualize the well known behaviour the the flow becomes flattend as the Hartmann number increases. The findings confirm that DQM serves as a robust, computationally inexpensive framework for simulating multi-physical MHD phenomena.

References

Aydin, S.H., & Erdoğan, M.C. (2023). Stabilization in 3-D FEM and solution of the MHD equations. Mathematical Methods in the Applied Sciences, 46(12), 13395–13410. https://doi.org/10.1002/mma.9259

Bellman, R., Kashef, B.G., & Casti, J. (1972). Differential quadrature: a tecnique for the rapid solution of nonlinear differential equations. Journal of Computational Physics, 10, 40–52. https://doi.org/10.1016/0021-9991(72)90089-7

Bellman, R., Kashef, B., Lee, E.S., & Vasudevan, R. (1975). Differential Quadrature and Splines. Computers and Mathematics with Applications, Pergamon, Oxford, 1(3-4), 371–376. https://doi.org/10.1016/0898-1221(75)90038-3

Chang, S. (2000). Differential Quadrature and Its Application in Engineering. Springer-Verlag, London.

Geeta, A., & Brajesh, K.S. (2013). Numerical solution of Burgers' equation with modified cubic B-spline differential quadrature method. Applied Mathematics and Computation, 224, 166–177. https://doi.org/10.1016/j.amc.2013.08.071

Hartmann, J., (1937). Theory of the laminar flow of an electrically conductive liquid in a homogeneous magnetic field. K. Dan. Vidensk. Selsk. Mat. Fys. Medd., 15(6), 1-28.

Korkmaz, A., & Dağ, İ. (2012). Cubic B-spline differential quadrature methods for the advection-diffusion equation. International Journal of Numerical Methods for Heat & Fluid Flow, 22(8), 1021–1036. https://doi.org/10.1108/09615531211271844

Meirikim, P., & Roshan, T. (2024). A local differential quadrature method for the generalized nonlinear Schrödinger (GNLS) equation. An International Journal of Optimization and Control: Theories & Applications, 14(4), 394–403. https://doi.org/10.11121/ijocta.1546

Shercliff, J. A. (1956). The flow of conducting fluids in circular pipes under transverse magnetic fields. Journal of Fluid Mechanics, 1(6), 644–666. https://doi:10.1017/S0022112056000421

Tezer-Sezgin, M. (2004). Solution of magnetohydrodynamic flow in a rectangular duct by differential quadrature method. Computers & Fluids, 33(4), 533–547. https://doi.org/10.1016/S0045-7930(03)00072-0

Temporal Memory Estimation for Multi-Horizon HVAC Load Forecasting

Seda Ermiş*

Osmaniye Korkut Ata University, Electrical - Electronics Engineering Department, Osmaniye, Türkiye
sedaermis@osmaniye.edu.tr

Abstract

Accurate multi-horizon HVAC load forecasting requires an effective representation of historical information, whose optimal extent may vary with prediction horizon. This study investigates the relationship between forecast horizon, temporal-memory length, and memory representation to empirically estimate effective memory requirements for HVAC load forecasting. Using hourly PLEIAData Building A data, five forecast horizons (1, 3, 6, 12, and 24 h) and five memory lengths (1, 3, 6, 12, and 24 h) are evaluated. Three strategies are compared: a no-memory baseline using contemporaneous predictors, explicit memory using autoregressive load information and window-averaged statistics, and implicit memory learned from historical sequences. XGBoost, LSTM, and GRU models are evaluated under a chronological, leakage-safe train–validation–test protocol. Results show that temporal memory substantially improves forecasting performance, with explicit memory achieving higher predictive accuracy at the 1-, 3-, 6-, and 12-h horizons. For 1-h forecasting, only 3 h of explicit memory achieves near-optimal performance (R^2 = 0.819), compared with R^2 = 0.820 using the nominally best 24-h memory window and 0.556 for the no-memory baseline. Longer horizons increasingly benefit from 12–24 h memory windows, suggesting greater relevance of recurring daily temporal structure. At 24 h, a 12-h implicit-memory sequence marginally outperforms the best explicit configuration (R^2 = 0.638 versus 0.631). These findings demonstrate that the effective temporal-memory requirement is horizon-dependent and cannot be treated as a fixed modeling choice. Forecast horizon, memory representation, and the temporal characteristics of the underlying load series should therefore be considered jointly when designing multi-horizon HVAC forecasting systems.

Keywords: HVAC load forecasting, temporal memory, multi-horizon forecasting, feature engineering, building energy forecasting.

1. Introduction

Accurate forecasting of building energy demand is an important component of intelligent energy management, supporting operational planning, demand-side management, and more efficient control of heating, ventilation, and air-conditioning (HVAC) systems. With the increasing availability of building monitoring data, data-driven approaches have become widely used for energy and HVAC load prediction because of their ability to capture complex relationships among environmental, operational, and temporal variables (Amasyali & El-Gohary, 2018; Li et al., 2025; Liu et al., 2023). Machine-learning and deep-learning methods have consequently been applied to a broad range of forecasting problems, from short-term load prediction to more complex temporal modeling tasks.

An important aspect of data-driven load forecasting is the representation of temporal information. Building and electricity loads exhibit temporal dependencies arising from operating schedules, weather conditions, occupancy patterns, and recurring daily or weekly behavior. Accordingly, lagged observations and other temporal features can provide substantial predictive information beyond

* *Corresponding Author*

contemporaneous input variables. Previous studies have demonstrated the usefulness of historical load information and multi-lag feature engineering for improving load forecasting performance (Incremona et al., 2021; Shafiuzzaman et al., 2025). In our previous study on the PLEIAData building dataset (Ermis, 2026), temporal feature engineering was systematically investigated for short-term HVAC load forecasting, showing that the inclusion of autoregressive and rolling features produced substantially larger performance improvements than changes in the underlying prediction architecture alone. However, that study was limited to one-step-ahead forecasting and therefore did not examine whether the required historical context changes with forecast horizon.

This issue becomes particularly relevant in multi-horizon forecasting. Recent studies have investigated building load prediction across multiple future horizons using both conventional machine-learning and deep-learning architectures. Akter et al. (2025) developed a hybrid deep-learning framework for multi-horizon power-load forecasting in academic buildings, while Chalapathy et al. (2021) compared shallow and deep-learning approaches for multi-step-ahead building cooling-load prediction. These studies demonstrate that forecasting performance and model behavior vary as the prediction horizon increases. Nevertheless, the relationship between forecast horizon and the amount of historical information supplied to the model has received comparatively less systematic attention. In particular, temporal memory is often embedded within a selected feature set or learned implicitly by sequential architectures, rather than being treated as an experimental variable whose length can be controlled across forecast horizons. This raises a practical question: does the amount and representation of useful temporal memory change with the intended forecast horizon?

To address this question, this study investigates HVAC load forecasting for PLEIAData Building A using a controlled multi-horizon and multi-memory framework. Forecast horizons of 1, 3, 6, 12, and 24 h are evaluated with historical memory lengths of 1, 3, 6, 12, and 24 h. Three temporal representations are compared: a no-memory configuration based on contemporaneous predictors, explicit memory constructed from autoregressive load information and window-averaged features, and implicit memory learned from historical sequences. XGBoost, LSTM, and GRU models are evaluated using a chronological, leakage-safe protocol. Rather than seeking a single optimal forecasting model, the analysis examines how the amount and representation of useful historical information vary with forecast horizon, enabling the effective temporal-memory requirement to be empirically estimated across prediction horizons. This extends our previous single-horizon investigation (Ermis, 2026) toward horizon-dependent temporal-memory estimation for multi-horizon HVAC load forecasting.

2. Materials and Methods

2.1. Dataset and Preprocessing

The experiments used Building A of the PLEIAData dataset, comprising building energy consumption, HVAC operation, indoor conditions, and meteorological measurements (Ibarra et al., 2023). The processed dataset contained 8,077 complete hourly records spanning January 1–December 17, 2021 (UTC), with incomplete intervals excluded without interpolation. The forecasting target was hourly HVAC energy consumption (dif_cons_real, kWh).

Seven contemporaneous predictors were retained from our previous study (Ermis, 2026): outdoor temperature ($tmed$, °C), number of active HVAC devices ($V4$), HVAC setpoint-related control ($V12$, °C), indoor temperature ($V2$, °C), solar radiation ($radmed$, W/m²), dew point temperature ($dewpt$, °C), and a binary seasonal indicator ($Season_3$). This predictor set remained fixed across all experiments, with historical load lags and window-averaged features added according to the memory configuration. Following horizon-specific eligibility checks, 6,143–6,203 training and 1,466–1,514 test samples were retained across the five forecast horizons.

2.2. Multi-Horizon Temporal Memory Design

Let y_t denote the HVAC energy consumption observed at the prediction origin t, and let $\boldsymbol{x}_t$ represent the contemporaneous exogenous and operational variables available at the same time. The forecasting problem is formulated as

$$\hat{y}_{t+H} = f\left(\boldsymbol{x}_t, \mathcal{M}_t^{(M)}\right), \tag{1}$$

where H represents the forecast horizon and $\mathcal{M}_t^{(M)}$ denotes the historical information available within a memory window of length M. Five forecast horizons and five memory lengths were investigated: $H, M \in \{1, 3, 6, 12, 24\}$ h. Forecast horizon and memory length were varied independently, with historical information always terminating at the prediction origin t. Thus, each forecast horizon was evaluated with all five memory lengths, resulting in 25 horizon–memory combinations.

Three temporal-memory representations were investigated. In the no-memory configuration, forecasting was performed using only the contemporaneous core predictor vector:

$$\hat{y}_{t+H} = f(\boldsymbol{x}_t). \tag{2}$$

In the explicit-memory configuration, historical HVAC load information was introduced directly into the predictor space. For a memory length M, the autoregressive load-history vector was defined as

$$\boldsymbol{\mathcal{L}}_t^{(M)} = \{y_t, y_{t-1}, \dots, y_{t-M+1}\}. \tag{3}$$

For $M > 1$, the representation was further augmented by the mean value of each core predictor and the HVAC load over the same M-hour historical window:

$$\bar{x}_{j,t}^{(M)} = \frac{1}{M}\sum_{i=0}^{M-1} x_{j,t-i}, \tag{4}$$

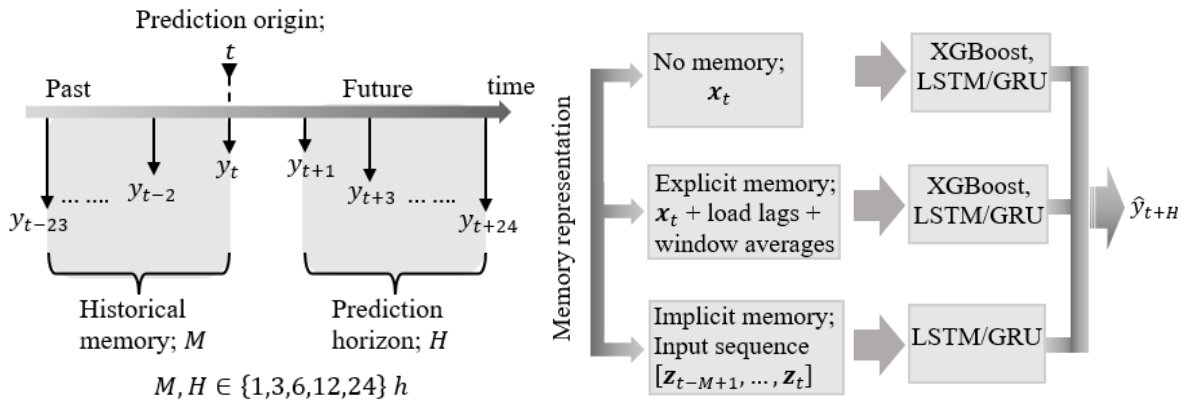
$$\bar{y}_t{}^{(M)} = \frac{1}{M}\sum_{i=0}^{M-1} y_{t-i}. \tag{5}$$

Accordingly, explicit memory combines the contemporaneous core predictors, individual historical load lags, and window-averaged representations of the core variables and HVAC load. For $M = 1$, window averages were omitted because they duplicate the current observations.

In the implicit-memory configuration, historical information was supplied directly as a multivariate sequence rather than through manually engineered features. Defining $\boldsymbol{z}_t = [\boldsymbol{x}_t, y_t]$, the input sequence for a memory window M was

$$\boldsymbol{S}_t^{(M)} = \{\boldsymbol{z}_{t-M+1}, \dots, \boldsymbol{z}_t\}, \tag{6}$$

These sequences were provided directly to the LSTM and GRU models, allowing the temporal representation to be learned internally. The overall definitions of forecast horizon, historical memory, and the three memory representations are illustrated in Figure 1.



(a) (b)

Figure 1. Multi-horizon temporal-memory forecasting framework. (a) Historical memory length M and forecast horizon H relative to the prediction origin t, where $M, H \in \{1, 3, 6, 12, 24\}$ h. (b) Memory representations and corresponding forecasting architectures: no memory using contemporaneous predictors, explicit memory using load lags and window-averaged features, and implicit memory using historical input sequences.

2.3. Forecasting Models and Experimental Setup

Three forecasting architectures were employed to compare feature-based explicit memory with sequence-based implicit memory. XGBoost, LSTM, and GRU were evaluated for the no-memory and explicit-memory configurations, while implicit memory was evaluated using LSTM and GRU. Model settings were kept fixed across forecast horizons and memory lengths, as summarized in Table 1.

All experiments followed a chronological, leakage-safe evaluation protocol with a fixed temporal cutoff at 80% of the canonical hourly dataset. For each forecast horizon H, training origins were retained only when both the prediction origin t and target $t + H$ occurred before the cutoff; origins whose targets crossed the cutoff were purged. Test origins were restricted to the period at or after the cutoff. To preserve actual hourly spacing, load lags and memory windows were constructed using exact timestamps rather than consecutive row positions. Only origins with a complete 24-h historical window and a target at exactly $t + H$ were retained, ensuring identical forecast origins across memory lengths within each horizon.

For LSTM and GRU, the final 10% of the outer training period was chronologically reserved for epoch selection, with an additional horizon-dependent purge preventing sub-training targets from crossing the validation cutoff. Early stopping determined the best epoch, after which each recurrent model was rebuilt and refitted on the complete outer training set for the selected number of epochs. MinMax scaling was fitted exclusively on the corresponding training partition. XGBoost was fitted directly on the complete outer training set using the fixed settings in Table 1.

Performance was evaluated on the held-out test set using R^2, RMSE, and MAE. The best-performing model–memory configurations were identified retrospectively based on test RMSE and are reported as observed comparisons rather than independently validated optima. A fixed random state of 42 was used for reproducibility.

Table 1. Hyperparameter settings used for the forecasting models.

Model	Hyperparameter	Value
XGBoost	Number of trees (n_estimators)	300
	Maximum tree depth (max_depth)	5
	Learning rate	0.05
	Subsample ratio	0.9
	Column sampling (colsample_bytree)	0.9
	Objective function	reg:squarederror
LSTM / GRU	Recurrent units	64
	Dropout rate	0.2
	Dense layer units	32
	Dense activation	ReLU
	Optimizer	Adam
	Loss function	MSE
	Maximum epochs	150
	Early-stopping patience	15 epochs
	Batch size	32
	Output layer	1 neuron

3. Results and Discussion

The results demonstrate the benefit of incorporating historical information into HVAC load forecasting. As shown in Fig. 2, explicit memory outperformed the no-memory baseline across all forecast horizons. At H = 1 h, the best explicit configuration achieved $R^2 = 0.820$ with M = 24 h, compared with 0.556 for the baseline. However, M = 3 h achieved nearly identical performance ($R^2 = 0.819$; RMSE = 0.780 versus 0.778 for M = 24 h). In contrast, extending memory from 3 to 24 h reduced RMSE by 7.6% and 16.8% at H = 3 and 6 h, respectively. The best explicit-memory R^2 decreased to 0.717, 0.609, and 0.577 at H = 3, 6, and 12 h. At H = 24 h, performance partially recovered, with implicit and explicit configurations reaching $R^2 = 0.638$ and 0.631, respectively, compared with 0.433 for the baseline. This non-monotonic pattern may reflect recurring temporal structure in the HVAC load series. Table 2 summarizes the best configurations with R^2, RMSE, and MAE.

The effectiveness of historical information depended on both forecast horizon and memory representation. Explicit memory achieved higher R^2 at H = 1–12 h, benefiting from load lags and window-averaged load and predictor features. Implicit memory learned directly from historical sequences and showed greater variation across horizon–memory combinations. At H = 24 h, a 12-h implicit LSTM sequence slightly exceeded the best explicit configuration in R^2 (0.638 versus 0.631) and RMSE (1.051 versus 1.061), although its MAE was higher (0.846 versus 0.780). Thus, neither longer memory nor sequential representation consistently improved all performance metrics.

Overall, the results suggest that effective temporal-memory requirements are horizon-dependent. A 3-h memory was nearly as effective as 24 h at H = 1 h, whereas longer windows offered greater benefits at intermediate horizons. The partial recovery at H = 24 h may be associated with daily load patterns. These findings support evaluating memory length jointly with forecast horizon and representation rather than assuming that longer historical windows always improve accuracy. As the experiments used a single fixed random seed, the observed differences should be interpreted descriptively rather than as evidence of statistical robustness.

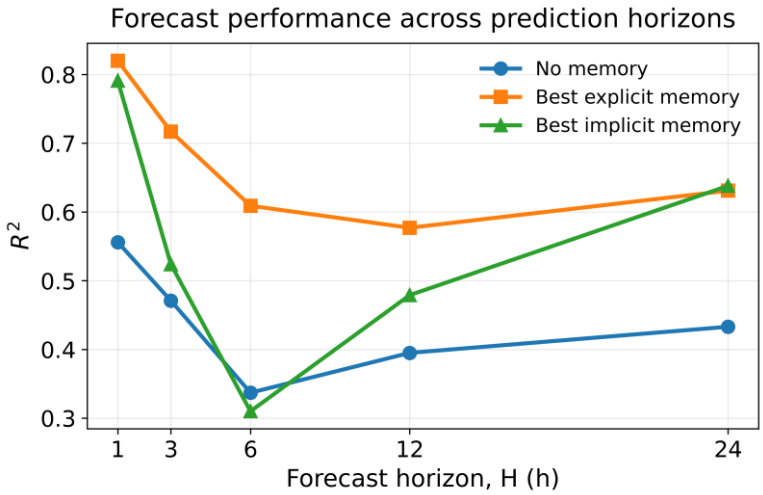


Figure 2. Forecasting performance across prediction horizons for the best no-memory, explicit-memory, and implicit-memory configurations.

Table 2. Best explicit- and implicit-memory forecasting configurations across forecast horizons. RMSE and MAE are expressed in kWh.

H (h)	Explicit	M (h)	R^2	RMSE	MAE	Implicit	M (h)	R^2	RMSE	MAE
1	XGBoost	24	.820	.778	.576	GRU	3	.791	.839	.663
3	XGBoost	24	.717	.964	.696	LSTM	24	.524	1.249	1.055
6	XGBoost	24	.609	1.117	.826	LSTM	24	.310	1.485	1.258
12	XGBoost	12	.577	1.142	.914	GRU	12	.479	1.268	1.050
24	XGBoost	24	.631	1.061	.780	LSTM	12	.638	1.051	.846

4. Conclusion

This study investigated horizon-dependent temporal-memory requirements for multi-horizon HVAC load forecasting using hourly PLEIAData Building A data. Five forecast horizons and five memory lengths were systematically evaluated using no-memory, explicit-memory, and implicit-memory representations with XGBoost, LSTM, and GRU models.

Temporal memory substantially improved forecasting performance, with explicit memory achieving higher R^2 at the 1–12 h horizons. At H = 1 h, only 3 h of explicit memory achieved $R^2 = 0.819$, nearly matching the 24-h configuration ($R^2 = 0.820$). Longer memory windows provided greater benefits at intermediate horizons, while a 12-h implicit-memory sequence achieved slightly higher R^2 than the best explicit configuration at H = 24 h (0.638 versus 0.631). The partial recovery in forecasting accuracy at 24 h may reflect recurring temporal structure in the load series.

Overall, effective temporal-memory requirements depend jointly on forecast horizon, memory representation, and load-series characteristics rather than simply on the amount of historical information available. The findings motivate further evaluation across buildings with different temporal and forecastability characteristics to determine the generalizability of the observed memory–horizon relationships.

References

Akter, R., Shirkoohi, M. G., Wang, J., & Mérida, W. (2025). An efficient hybrid deep neural network model for multi-horizon forecasting of power loads in academic buildings. *Energy and Buildings, 329*, 115217. https://doi.org/10.1016/j.enbuild.2024.115217

Amasyali, K., & El-Gohary, N. M. (2018). A review of data-driven building energy consumption prediction studies. *Renewable and Sustainable Energy Reviews, 81*, 1192–1205. https://doi.org/10.1016/j.rser.2017.04.095

Chalapathy, R., Khoa, N. L. D., & Sethuvenkatraman, S. (2021). Comparing multi-step ahead building cooling load prediction using shallow machine learning and deep learning models. *Sustainable Energy, Grids and Networks, 28*, 100543. https://doi.org/10.1016/j.segan.2021.100543

Ermis, S. (2026). Improving short-term HVAC load forecasting via temporal feature engineering: Insights from the PLEIAData building dataset. *Energy Informatics, 9*, 69. https://doi.org/10.1186/s42162-026-00670-5

Ibarra, A. M., González-Vidal, A., & Skarmeta, A. (2023). PLEIAData: Consumption, HVAC, temperature, weather and motion sensor data for smart buildings applications. *Scientific Data, 10*, 118. https://doi.org/10.1038/s41597-023-02023-3

Incremona, A., De Nicolao, G., Fusco, F., Eck, B. J., & Tirupathi, S. (2021). Aggregation of nonlinearly enhanced experts with application to electricity load forecasting. *Applied Soft Computing, 112*, 107857. https://doi.org/10.1016/j.asoc.2021.107857

Li, Y., Arellano-Espitia, F., Aler, R., Igualada, L., & Corchero, C. (2025). Data-driven methods and their applications to building HVAC energy consumption prediction: A review. *Journal of Building Engineering, 116*, 114612. https://doi.org/10.1016/j.jobe.2025.114612

Liu, H., Liang, J., Liu, Y., & Wu, H. (2023). A review of data-driven building energy prediction. *Buildings, 13*(2), 532. https://doi.org/10.3390/buildings13020532

Shafiuzzaman, M., Islam, M. S., Bashar, T. M. R., Munem, M., Nahiduzzaman, M., Ahsan, M., & Haider, J. (2025). Enhanced very short-term load forecasting with multi-lag feature engineering and Prophet-XGBoost-CatBoost architecture. *Energy, 335*, 137981. https://doi.org/10.1016/j.energy.2025.137981

Spatial Heterogeneity in Provincial Housing Sales in Türkiye: A Comparative Analysis of OLS, SAR, SEM, and GWR Models

İbrahim Arık[1], İlhan Usta[2], Yeliz Mert Kantar [2*]

[1] *Kütahya Dumlupınar University, Business Department, Kütahya, Türkiye*
[2] *Eskisehir Technical University, Department of Statistics, Eskişehir, Türkiye*
ymert@eskisehir.edu.tr

Abstract

This study examines spatial heterogeneity in provincial housing sales across Türkiye's 81 provinces, drawing on 2024 cross-sectional data. To correct for the scale effect introduced by provincial population size, the outcome variable is specified as the log of housing sales per 1,000 inhabitants. Four modelling frameworks are compared: Ordinary Least Squares (OLS), the Spatial Autoregressive Model (SAR), the Spatial Error Model (SEM), and Geographically Weighted Regression (GWR). Based on variance inflation factor (VIF) diagnostics, net migration rate, urbanization rate, log-transformed building occupancy permits per capita, and youth population ratio are retained as predictors, with a maximum VIF of 2.76 confirming the absence of problematic multicollinearity. Global Moran's I reveals pronounced spatial clustering in per-capita housing sales ($I = 0.372$, $p<0.001$), and, notably, spatial autocorrelation persists in the OLS residuals ($I = 0.123$, $p = 0.029$), signalling that the conventional model fails to fully capture the underlying spatial structure and thereby justifying a spatial econometric approach. Of the two global spatial specifications, SEM offers the better fit, returning the lowest AICc (7.13) alongside a significant spatial error term ($\lambda = 0.306$, $p = 0.032$). The strongest overall performance, however, comes from GWR (AICc = 3.32; Adj. $R^2 = 0.644$), which uncovers substantial spatial non-stationarity in the net migration–housing sales relationship, including a reversal of sign across provinces, whereas the associations for urbanization rate, building occupancy permits, and youth population ratio remain comparatively stable across space. These results collectively suggest that jointly modelling spatial dependence and spatially varying coefficients yields a richer and more accurate picture of provincial housing sales dynamics than OLS can provide on its own.

Keywords: Geographically weighted regression, spatial econometrics, housing sales, Türkiye, spatial heterogeneity, per-capita normalization, multicollinearity

1. Introduction

Housing markets are inherently spatial phenomena. The determinants of housing sales activity are not uniformly distributed across geographic space; rather, they vary according to local demographic, economic, and infrastructural conditions (Fotheringham et al., 2002). Conventional regression methods such as Ordinary Least Squares (OLS) assume parameter stationarity – that is, the relationship between explanatory variables and the outcome does not vary across geographic locations. When applied to spatially structured data, this assumption frequently leads to biased estimates and misleading inference (Anselin, 1988; LeSage & Pace, 2009).

Türkiye presents a compelling case for spatially disaggregated housing market analysis. The country exhibits pronounced regional disparities in urbanization, demographic dynamics, and economic

* *Corresponding Author*

development, translating into substantial variation in housing market activity across its 81 provinces (Turkstat, 2024a).

A fundamental challenge in province-level housing sales analysis is scale: raw sales counts are mechanically correlated with provincial population size, inflating apparent explanatory power and obscuring the true relationships between predictors and housing market activity. The present study addresses this by normalizing housing sales per 1,000 inhabitants, removing the population size effect and allowing variation in housing sales intensity to be assessed independently of provincial population size. This normalization increases Moran's I from 0.281 to 0.372, confirming more pronounced geographic clustering (Section 5.1).

Despite the growing body of spatial econometric methods applicable to housing markets (Anselin, 1995; Can, 1992; Bitter et al., 2007), province-level studies in Türkiye employing comparative spatial regression frameworks remain scarce. The present study addresses this gap by estimating and comparing OLS, SAR, SEM, and GWR models using 2024 provincial data compiled from official Turkstat sources, with particular attention to variable selection and multicollinearity control.

2. Literature Review

2.1. Spatial Approaches to Housing Markets

Spatial econometric methods for housing markets have grown substantially since Anselin's (1988) foundational work: Can (1992) showed that spatial autocorrelation yields inefficient OLS estimates, and Pace and Gilley (1997) confirmed that ignoring spatial dependence distorts coefficient estimates and standard errors. GWR, introduced by Brunsdon et al. (1996) and formalized by Fotheringham et al. (2002), extends local regression to allow parameters to vary continuously over space, revealing significant spatial non-stationarity in housing price and demand determinants (Bitter et al., 2007; Lu et al., 2014). Studies comparing GWR with global models find it better captures local variation in specific settings, while SAR and SEM offer targeted corrections for specific forms of spatial dependence (Páez et al., 2011; Sisman & Aydinoglu, 2022).

2.2. Determinants of Provincial Housing Sales

The theoretical framework for housing demand draws from life-cycle models of housing tenure (Muth, 1969; DiPasquale & Wheaton, 1994). Migration inflows, which respond to regional amenities and economic opportunity (Rappaport, 2007), directly increase household formation and housing demand in receiving provinces. Urbanization concentrates population in urban cores, shaping local housing market activity. Building occupancy permits per capita are used here as this study's operational measure of completed housing supply entering the market. Youth population share (ages 15–34) captures the cohort with peak housing demand (Mankiw & Weil, 1989).

At the sub-provincial level, Sisman and Aydinoglu (2022) demonstrated that GWR captured spatial variation in Istanbul housing prices that global models could not recover. The present study extends this literature to the full national set of 81 provinces using per-capita normalized outcomes and a rigorous variable selection procedure.

3. Data and Variables

All data are obtained from the Turkish Statistical Institute (Turkstat) for 2024. The dependent variable is the natural logarithm of housing sales per 1,000 provincial inhabitants, derived from the December 2024 Housing Sales Statistics bulletin (Turkstat, 2024a) and 2024 ADNKS population estimates (Turkstat, 2024b).

Independent variables are selected in two stages. A theoretically motivated initial set of six variables was considered: net migration rate, population growth rate, urbanization rate, log-transformed building occupancy permits per capita, average household size, and youth population ratio. Net migration data

are drawn from Internal Migration Statistics (Turkstat, 2024c) and building occupancy permits from Building Construction Statistics (Turkstat, 2024d). VIF analysis revealed severe multicollinearity between net migration rate and population growth rate ($r = 0.907$, VIF > 14) and between average household size and youth population ratio ($r = 0.867$, VIF > 6). Following standard practice, for each highly correlated pair, one variable was retained based on its stronger theoretical relevance: net migration rate over population growth rate, as migration more directly reflects housing-relevant relocation decisions, and youth population ratio over household size, as the 15–34 age cohort is most directly tied to household formation and housing tenure decisions (Mankiw & Weil, 1989); its expected sign is treated as ambiguous a priori, since a larger young-adult share may reflect either elevated demand or constrained purchasing power. The final four-variable model yields maximum VIF = 2.76, well below the conventional threshold of 5. Table 1 summarizes the final variable set.

Table 1. Final variable set after VIF-based selection. All variables are measured at the provincial level for 2024.

Variable	Code	Expected Sign	Source
Net migration rate (‰)	*X1*	+	Turkstat – Internal Migration Statistics 2024
Urbanization rate (%)	*X3*	+	Turkstat – ADNKS 2024 (DEGURBA)
ln(Building occupancy permits per 1,000)	*X4*	+	Turkstat – Building Construction Statistics 2024
Youth population ratio (%, ages 15–34)	*X6*	+/−	Turkstat – ADNKS 2024

4. Methodology

4.1. Spatial Autocorrelation Test

Global Moran's I (Moran, 1950) is first used to assess the overall spatial clustering of log-transformed per-capita housing sales. A row-standardized Queen contiguity spatial weights matrix is used to define neighbouring provinces. Moran's I is subsequently applied to the OLS residuals to assess whether spatial dependence remains after accounting for the explanatory variables; significant residual spatial autocorrelation motivates the estimation of spatial regression models.

4.2. OLS, SAR and SEM

The baseline OLS model assumes parameter stationarity and spatially independent errors. The SAR model augments OLS with a spatially lagged dependent variable: $\ln(Y)=\rho W\cdot\ln(Y)+X\beta+\varepsilon$, where ρ captures housing market spillover effects among neighbouring provinces (LeSage & Pace, 2009); because of this multiplier, SAR β are not direct marginal effects, and direct/indirect impact decomposition (LeSage & Pace, 2009) is left for future work. The SEM accounts for spatial dependence in the error process: $\ln(Y)=X\beta+u$, $u=\lambda Wu+\varepsilon$, where λ captures spatially correlated unobservables (Anselin, 1988). Lagrange Multiplier (LM) diagnostics are examined to assess the form of residual spatial dependence, while SAR and SEM are compared using model fit and residual diagnostics (Anselin et al., 1996).

4.3. Geographically Weighted Regression

GWR extends the global regression framework by allowing all parameters to vary continuously across geographic space (Brunsdon et al., 1996; Fotheringham et al., 2002): $\ln(Y)_i=\beta_0(u_i,v_i)+\Sigma_k\beta_k(u_i,v_i)X_{ki}+\varepsilon_i$, where (u_i,v_i) are the coordinates of province i and $\beta_k(u_i,v_i)$ is the locally estimated coefficient at that location. Local estimates are obtained by weighted least squares using an adaptive bisquare kernel, with

bandwidth selected via *AICc* minimization. The optimal bandwidth of 62 nearest neighbours reflects the trade-off between local flexibility and estimation stability given the 81-province sample size.

5. Results and Discussion

5.1. Spatial Autocorrelation

Global Moran's I on log per-capita housing sales is I = 0.372 ($p < 0.001$), indicating significant positive spatial clustering: provinces with high per-capita sales tend to cluster geographically, as do low-sales provinces. This value exceeds Moran's I computed on raw log sales counts (I = 0.281), indicating a more pronounced geographical clustering pattern when housing sales are expressed relative to population size. Moran's I on OLS residuals is 0.123 ($p = 0.029$), indicating statistically significant residual spatial dependence. However, the robust LM-error ($p = 0.386$) and robust LM-lag ($p = 0.758$) tests are both non-significant and therefore do not provide a decisive basis for distinguishing between spatial error and spatial lag mechanisms. SAR and SEM are consequently evaluated using comparative model fit and residual diagnostics.

5.2. Model Results and Comparison

Table 2 presents coefficient estimates and p-values for all four models. Table 3 summarizes model fit diagnostics.

Table 2. Coefficient estimates and p-values across models

Variable	OLS β(p)	SAR β(p)	SEM β(p)	GWR Median β
Intercept	2.289 (<0.001***)	1.644 (<0.001***)	2.142 (<0.001***)	2.028
Net migration rate (*X1*)	−0.003 (0.489)	−0.002 (0.496)	−0.002 (0.669)	−0.006
Urbanization rate (*X3*)	0.009 (0.005**)	0.008 (0.007**)	0.009 (0.002**)	0.007
ln(Bldg permits) (*X4*)	0.445 (<0.001***)	0.423 (<0.001***)	0.447 (<0.001***)	0.403
Youth pop. ratio (*X6*)	−0.034 (<0.001***)	−0.027 (0.003**)	−0.030 (0.003**)	−0.021
Spatial param. (ρ/λ)	—	0.194 (p=0.095)	0.306 (p=0.032*)	—

*Significance codes: *** p < 0.001 ** p < 0.01 * p < 0.05. GWR median local coefficients reported; individual p-values are not globally defined for GWR.*

Table 3. Model fit diagnostics

Model	AICc	Adj. R^2	Residual Moran's I	p-value	Interpretation
OLS	9.44	0.591	0.123	0.029*	Spatial dependence remains
SAR	8.50	0.608	0.044	0.216	ρ not significant (p=0.095)
SEM	7.13	0.614	0.008	0.390	Best global model
GWR	3.32	0.644	0.037	0.244	Best overall model

** indicates significant residual spatial autocorrelation (p < 0.05). AICc differences > 2 units indicate meaningful improvement in model fit.*

OLS achieves moderate explanatory power (Adj. $R^2 = 0.591$) with urbanization rate, building permits per capita, and youth population ratio reaching significance. Net migration rate is not significant at the global level ($p = 0.489$), while the GWR results presented below indicate opposing local associations across provinces that may offset one another in the global estimate.

SAR estimates a spatial autoregressive parameter of $\rho = 0.194$ ($p = 0.095$), falling short of conventional significance; its modest AICc gain over OLS (Table 3) is not a decisive improvement.

SEM estimates $\lambda = 0.306$ ($p = 0.032$), indicating spatially structured unobserved factors in the error process. SEM achieves the lowest AICc among global models (Table 3) and residuals with no statistically significant spatial autocorrelation. Coefficient estimates remain stable relative to OLS, with urbanization rate ($\beta \approx 0.009$), building permits ($\beta \approx 0.445$), and youth population ratio ($\beta \approx -0.030$) remaining stable across specifications.

GWR achieves the best overall model fit (Table 3): AICc = 3.32, Adj. $R^2 = 0.644$; the residual sum of squares falls by 24.5% relative to OLS (3.419 vs. 4.531), with no significant residual spatial autocorrelation (Moran's $I = 0.037$, $p = 0.244$). This AICc improvement exceeds the threshold conventionally associated with meaningful model improvement (Fotheringham et al., 2002).

5.3. GWR local coefficient maps

Figure 1 displays the spatial distribution of locally estimated GWR coefficients across Türkiye's 81 provinces. The maps illustrate geographical variation in local coefficients that is not represented by a single global coefficient estimate.

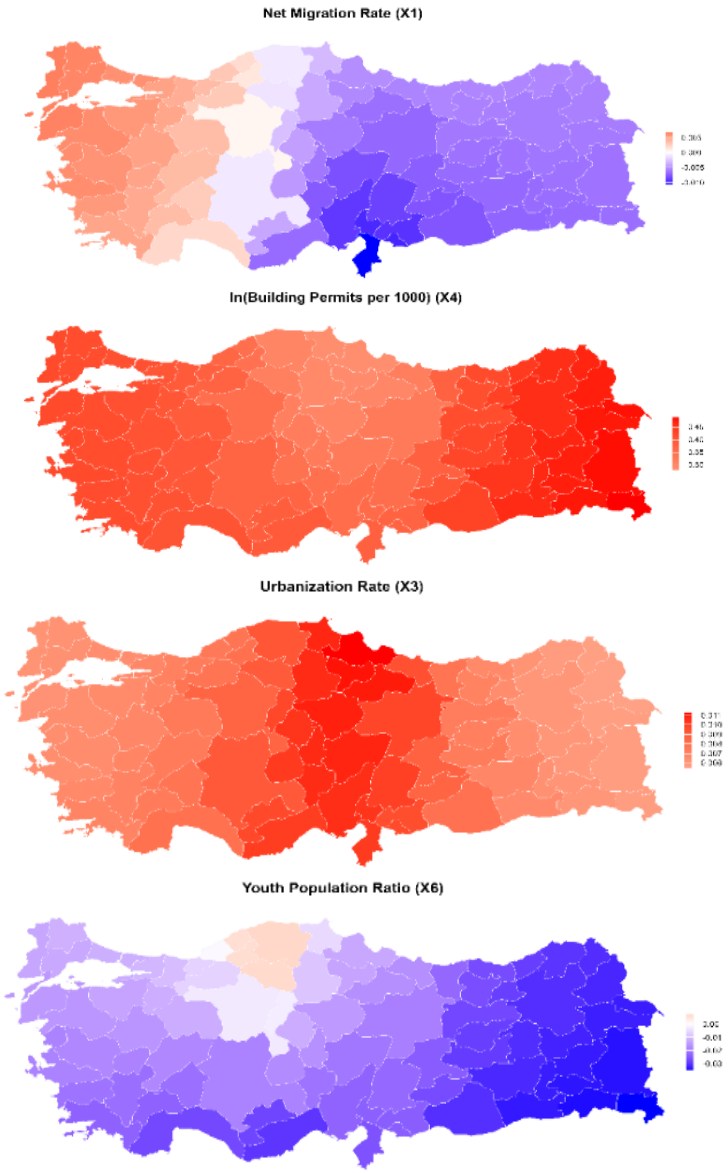


Figure 1. GWR local coefficient maps for housing sales determinants across 81 provinces of Türkiye (2024). Warm colours (red) indicate positive local coefficients; cool colours (blue) indicate negative local coefficients. Adaptive bisquare kernel, bandwidth = 62 nearest neighbours.

Net migration rate (*X1*) shows the most pronounced geographical variation among the predictors. Its local coefficient ranges from −0.011 in eastern provinces to +0.007 in parts of western and central Anatolia, indicating a clear sign reversal across the national territory. These offsetting local associations help explain why the global OLS coefficient is close to zero and non-significant ($\beta = -0.003$, $p = 0.489$). Urbanization rate (X3) and building permits (X4) show consistently positive local coefficients (0.005–0.011 and 0.280–0.487, respectively) with limited geographical variation. Youth population ratio (X6) is negative across most provinces (−0.035 to +0.007), turning marginally positive only in a small minority at the upper end of the distribution, consistent with higher young-adult shares concentrating in provinces where constrained incomes and limited access to housing finance restrain transactions rather than elevate demand. A formal Leung et al. (2000) test confirms this: overall F1 (0.86, $p = 0.152$) and F4 (0.75, $p = 0.120$) do not reject global stationarity, consistent with the large bandwidth, but the coefficient-specific F3 test is highly significant for net migration rate ($F3 = 3.86$, $p < 0.001$) and non-significant for the other predictors ($p > 0.68$), so non-stationarity is concentrated in that coefficient.

6. Conclusion

This study compares OLS, SAR, SEM, and GWR models for per-capita housing sales across Türkiye's 81 provinces in 2024. A VIF-based variable selection procedure yielded a parsimonious four-variable model with a maximum VIF of 2.76, indicating no evidence of problematic multicollinearity. Three principal findings emerge.

First, per-capita housing sales exhibit significant positive spatial autocorrelation, and OLS residuals retain significant spatial dependence (Table 3), supporting the use of spatial regression models.

Second, among global spatial models, SEM provides the strongest fit (Table 3); its significant spatial error parameter suggests that spatially structured unobserved factors remain in the error process. SAR performs comparably to OLS, with a non-significant autoregressive parameter offering limited evidence of a dominant spatial lag mechanism.

Third, GWR achieves the best overall fit (Table 3) and reveals pronounced geographical variation in the net migration–housing sales association, including sign reversals between eastern and western Türkiye that help explain the non-significant global OLS coefficient for net migration. Urbanization rate, building permits, and youth population ratio show comparatively stable local coefficients.

Limitations include the cross-sectional design, the exclusion of income and housing price data, and the relatively large GWR bandwidth (62 of 81 provinces). Future research should incorporate MGWR, extend the framework to panel data, and integrate provincial income proxies.

Acknowledgements

This study was supported by Eskişehir Technical University Scientific Research Projects Commission under grant no: 25ADP219.

References

Anselin, L. (1988). Spatial econometrics: Methods and models. Kluwer Academic Publishers.

Anselin, L. (1995). Local indicators of spatial association — LISA. Geographical Analysis, 27(2), 93–115. https://doi.org/10.1111/j.1538-4632.1995.tb00338.x

Anselin, L., Bera, A. K., Florax, R., & Yoon, M. J. (1996). Simple diagnostic tests for spatial dependence. Regional Science and Urban Economics, 26(1), 77–104. 10.1016/0166-0462(95)02111-6

Bitter, C., Mulligan, G. F., & Dall'erba, S. (2007). Incorporating spatial variation in housing attribute prices: A comparison of geographically weighted regression and the spatial expansion method. Journal of Geographical Systems, 9, 7–27. https://doi.org/10.1007/s10109-006-0028-7

Brunsdon, C., Fotheringham, A. S., & Charlton, M. E. (1996). Geographically weighted regression: A method for exploring spatial nonstationarity. Geographical Analysis, 28(4), 281–298. https://doi.org/10.1111/j.1538-4632.1996.tb00936.x

Can, A. (1992). Specification and estimation of hedonic housing price models. Regional Science and Urban Economics, 22, 453–474. https://doi.org/10.1016/0166-0462(92)90039-4

DiPasquale, D., & Wheaton, W. C. (1994). Housing market dynamics and the future of housing prices. Journal of Urban Economics, 35(1), 1–27. https://doi.org/10.1006/juec.1994.1001

Fotheringham, A. S., Brunsdon, C., & Charlton, M. (2002). Geographically weighted regression: The analysis of spatially varying relationships. John Wiley & Sons.

LeSage, J., & Pace, R. K. (2009). Introduction to spatial econometrics. CRC Press.

Leung, Y., Mei, C.-L., & Zhang, W.-X. (2000). Statistical tests for spatial nonstationarity based on the geographically weighted regression model. Environment and Planning A: Economy and Space, 32(1), 9–32. https://doi.org/10.1068/a3162

Lu, B., Charlton, M., Harris, P., & Fotheringham, A. S. (2014). Geographically weighted regression with a non-Euclidean distance metric. International Journal of Geographical Information Science, 28(4), 660–681. https://doi.org/10.1080/13658816.2013.865739

Mankiw, N. G., & Weil, D. N. (1989). The baby boom, the baby bust, and the housing market. Regional Science and Urban Economics, 19(2), 235–258. https://doi.org/10.1016/0166-0462(89)90005-7

Moran, P. A. P. (1950). Notes on continuous stochastic phenomena. Biometrika, 37(1–2), 17–23. https://doi.org/10.2307/2332142

Muth, R. F. (1969). Cities and housing: The spatial pattern of urban residential land use. University of Chicago Press.

Pace, R. K., & Gilley, O. W. (1997). Using the spatial configuration of the data to improve estimation. Journal of Real Estate Finance and Economics, 14(3), 333–340.

Páez, A., Farber, S., & Wheeler, D. (2011). A simulation-based study of geographically weighted regression as a method for investigating spatially varying relationships. Environment and Planning A, 43(12), 2992–3010. https://doi.org/10.1068/a44111

Rappaport, J. (2007). Moving to nice weather. Regional Science and Urban Economics, 37(3), 375–398. https://doi.org/10.1016/j.regsciurbeco.2006.11.004

Sisman, S., & Aydinoglu, A. C. (2022). A modelling approach with geographically weighted regression methods for determining geographic variation and influencing factors in housing price: A case in Istanbul. Land Use Policy, 119, https://doi.org/10.1016/j.landusepol.2022.106183

Turkstat. (2024a). Housing sales statistics (December 2024). Turkish Statistical Institute. https://data.tuik.gov.tr

Turkstat. (2024b). Address-based population registration system (ADNKS) 2024. Turkish Statistical Institute. https://data.tuik.gov.tr

Turkstat. (2024c). Internal migration statistics 2024. Turkish Statistical Institute. https://data.tuik.gov.tr

Turkstat. (2024d). Building construction statistics 2024. Turkish Statistical Institute. https://data.tuik.gov.tr

QoS-Aware Opportunistic Routing in Wireless Mesh Networks: An Integration-Centric Taxonomy and Mathematical Modeling Perspective

Noumedia Ouarab*, Samra Boulfekhar, Djamil Aissani

University of Bejaia, Faculty of Exact Sciences, LaMOS Research Unit (Modeling and Optimization of Systems), Bejaia 06000, Algeria
noumedia.ouarab@univ-bejaia.dz, samra.boulfekhar@univ-bejaia.dz, djamil.aissani@univ-bejaia.dz

Abstract

Opportunistic Routing (OR) can improve performance in wireless mesh networks (WMNs) by exploiting wireless broadcast and selecting packet forwarders from a set of candidate receivers. Integrating quality of service (QoS) involves balancing reliability, delay, throughput, and resource use while addressing congestion, mobility, security, and duplicate suppression. This paper presents a qualitative comparison of ten representative studies covering QoS-aware OR protocols, complementary routing mechanisms, and analytical models, with particular attention to their mathematical formulations and routing decisions. We propose a QoS-integration-centric taxonomy comprising seven categories: link and path performance; dynamic network state; network coding; flow-level QoS control; security and trust; mobility awareness; and analytical modeling and evaluation. The taxonomy distinguishes mechanisms supporting routing and resource control from complementary tools for performance evaluation. The comparison examines routing inputs, QoS metrics, target applications, mobility assumptions, forwarding coordination, duplicate suppression, and evaluation tools. The reviewed studies generally address selected QoS dimensions, while their joint optimization remains limited. These findings motivate integrated multi-objective decision models, adaptive candidate coordination, and evaluation under more realistic network and mobility conditions.

Keywords: Wireless mesh networks, Opportunistic Routing, Quality of Service, taxonomy, mathematical modeling, multi-objective optimization.

1. Introduction

Wireless mesh networks (WMNs) provide flexible and low-cost multi-hop connectivity, but link instability, interference, congestion, packet loss, and limited bandwidth make quality of service (QoS) difficult to guarantee (Calado et al., 2015). These limitations are especially important for multimedia, Internet of Things (IoT), and real-time applications. Recent work also stresses the need for multi-objective optimization because WMN routing decisions must balance several conflicting performance objectives (Amir et al., 2026).

Opportunistic Routing (OR) exploits the broadcast nature of wireless links: instead of committing to one fixed next hop, a sender transmits toward a candidate set and the highest-priority successful receiver forwards the packet. This can improve reliability and throughput, but creates additional problems in candidate selection, prioritization, coordination, and duplicate suppression. Related studies in VANETs and other wireless environments confirm the importance of graph-based, security-aware, and reliability-oriented modeling for OR decisions (Ouarab et al., 2025; Ryu & Kim, 2025; Xu & Wang, 2024).

QoS-aware OR approaches in WMNs exploit different information sources and mechanisms, including link and path performance, dynamic network state, network coding, resource control, trust, and mobility.

* *Corresponding Author*

This review examines how these elements support routing decisions and address QoS requirements. The main contributions are as follows:

i. We propose a QoS-integration-centric taxonomy that groups the reviewed approaches according to the information and mechanisms they exploit. We clarify their relationships with routing decision stages and distinguish OR protocols from complementary routing schemes and analytical models.
ii. We provide a qualitative comparison of the reviewed approaches in terms of QoS metrics and parameters, forwarding coordination, mobility assumptions, and evaluation settings.
iii. We examine the mathematical modeling principles underlying these approaches and identify research gaps concerning joint QoS optimization, adaptive candidate coordination, and realistic evaluation.

2. Background on QoS-Aware Opportunistic Routing

QoS-aware OR can be viewed as a three-stage decision process. Candidate selection first determines which neighboring nodes are eligible to relay a packet using information such as link quality, distance, delivery probability, energy, buffer occupancy, or trust. Candidate prioritization then ranks the selected forwarders so that the most suitable node transmits first. Forwarding coordination finally suppresses redundant transmissions through timers, acknowledgments, priority scheduling, relay suppression, or coding. These stages jointly determine path diversity, reliability, overhead, and delay.

QoS integration extends this decision process by embedding performance and resource requirements into selection, prioritization, coordination, or flow control. Depending on the protocol, the decision variables may include reliability, delay, throughput, energy, congestion, mobility, security, buffer state, bandwidth, and duplicate suppression. Therefore, QoS-aware OR should be characterized not only by the metrics used, but also by he information and mechanisms used, as well as the routing stages they affect.

3. Review of Existing Approaches

3.1. Review Methodology

This study presents a structured qualitative review of ten representative primary research studies whose publication years range from 2015 to 2023. The corpus comprises seven journal articles published in IEEE Access, Wireless Networks, EURASIP Journal on Wireless Communications and Networking, and IEEE Transactions on Vehicular Technology, together with three conference papers published in IEEE, ACM, and SCITEPRESS proceedings. This temporal interval describes the comparative corpus. Additional references provide background and contextual discussion.

Inclusion criteria. Studies are eligible for comparison when they: (i) address wireless mesh networks, including Bluetooth Mesh and IoT-oriented mesh environments; (ii) investigate QoS-related routing, opportunistic forwarding, resource control, or OR performance modeling; and (iii) provide sufficient methodological detail and analytical or simulation-based evaluation. Complementary mesh-routing schemes are included when they provide relevant insights into learning-based route selection, security, or mobility, and are explicitly distinguished from OR protocols.

Exclusion criteria. Duplicate copies or versions of the same publication are counted once. Studies unrelated to QoS-aware mesh routing or OR performance analysis, and publications lacking sufficient methodological or evaluation detail, fall outside the comparative corpus. Surveys and general background references are considered separately from the ten primary studies.

Assessment and synthesis. The analysis examines the abstracts and methodological and evaluation sections of each study. Extracted information includes routing inputs, QoS objectives and performance outcomes, candidate selection and prioritization, forwarding coordination, mathematical formulations, network technologies, mobility assumptions, evaluation settings, and reported limitations, where available. Studies are mapped to the seven categories presented in Section IV, allowing overlapping assignments. Their findings are compared qualitatively, taking account of differences in forwarding assumptions, network scenarios, and evaluation conditions.

3.2. Reviewed Approaches

This section provides a review of representative studies relevant to QoS-aware OR in WMNs. Studies were selected based on their relevance to this topic and their description of routing mechanisms, QoS metrics, and evaluation conditions. Complementary routing schemes and analytical models were also included when they helped explain QoS support or OR performance. Each study was examined in terms of the information and mechanisms used, QoS metrics and parameters, relay selection and prioritization, forwarding coordination, mobility assumptions, and evaluation settings. These dimensions provide the basis for the taxonomy and comparative analysis. Because the reviewed studies use different scenarios and evaluation conditions, the comparison is qualitative.

Performance- and resource-oriented schemes include the LSTM-based two-hop routing approach (Eyobu & Edwinah, 2023), evaluated in terms of PDR, throughput, delay, and jitter; EMOR (Khah et al., 2023), which jointly adapts transmission rate and power to reduce energy cost; OBOR (Bordier et al., 2021), which combines link throughput and buffer occupancy to avoid congested paths; and Fang et al. (2019), which couples opportunistic forwarding, network coding, and multi-rate selection to minimize expected transmission time. These approaches emphasize different QoS dimensions, making their operational assumptions and evaluation conditions important to the comparison.

Security- and mobility-oriented studies broaden the decision space. The trust-based protocol of Zhao and Srivastava (2022) selects relays using direct and indirect trust and social similarity, while MAMΔ (Paulon et al., 2021) supports data collection toward a mobile sink in Bluetooth Mesh. RTS (Haseeb et al., 2020) selects a next hop before transmission using link-cost information and establishes a routing path through RREQ/ACK exchanges. RSA-based cryptography provides data protection. RTS is retained as a complementary routing scheme for comparing security and mobility mechanisms in WMNs and is explicitly distinguished from candidate-set OR protocols.

Flow-level and analytical approaches address complementary aspects. Calado et al. (2015) use admission control and bandwidth reservation over a forwarder set; Darehshoorzadeh et al. (2016) model OR performance through a discrete-time Markov chain (DTMC) and derive delivery probability, expected transmissions, and hop-count measures; and QADC-MORE (Abdolahi et al., 2015) uses dynamic credit scheduling for multi-flow fairness and service differentiation. Coding-oriented work by Wan and Cheng (2026) provides additional context for the use of network coding to reduce redundant wireless retransmissions. Together, these studies motivate a taxonomy based on the information and mechanisms used to support QoS, complemented by analytical methods for performance evaluation.

4. Proposed QoS-Integration-Centric Taxonomy

The proposed taxonomy groups the reviewed approaches according to the information and mechanisms used to address QoS requirements. Seven categories are distinguished: (1) Link and path performance, using measured or estimated link and path performance indicators; (2) Dynamic network state, using link and node conditions, such as buffer occupancy, congestion, and load; (3) Network coding, exploiting coded forwarding to limit redundant transmissions; (4) Flow-level QoS control, addressing

admission control, bandwidth reservation, service differentiation, scheduling, and fairness; (5) Security and trust, considering relay trustworthiness and data protection; (6) Mobility awareness, accounting for mobile sinks or clients and route adaptation; and (7) Analytical modeling and evaluation, providing tools for modeling and assessing OR performance.

These categories have complementary roles. Link and path performance and Dynamic network state primarily support candidate selection and prioritization. Network coding supports forwarding and coordination, while Flow-level QoS control addresses resource allocation and scheduling. Security and trust supports relay selection and data protection, and Mobility awareness supports relay and route adaptation. Analytical modeling and evaluation provides complementary tools, including discrete-time Markov chain models, to estimate delivery probability and expected transmissions.

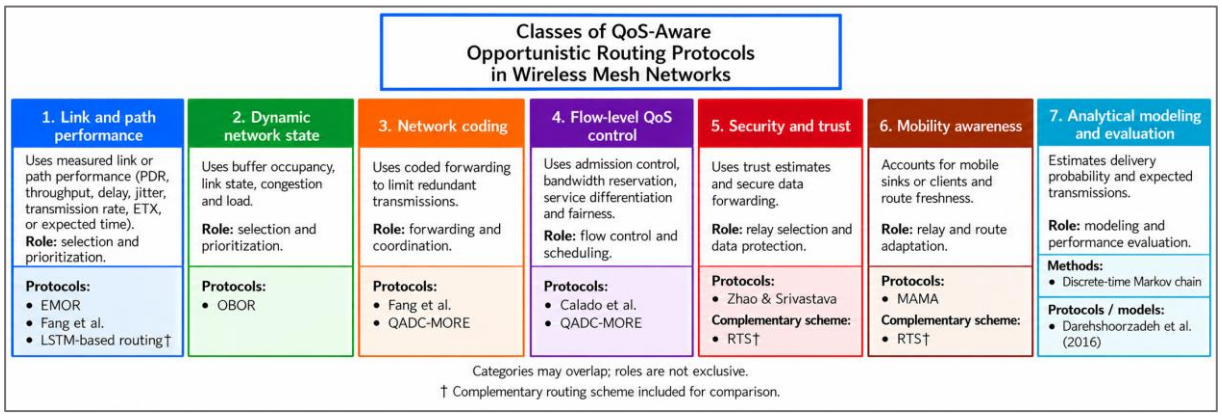


Figure 1. QoS-integration-centric classification of Opportunistic Routing approaches in wireless mesh networks

Categories may overlap when an approach combines several information sources or mechanisms, and their roles are non-exclusive. Figure 1 summarizes the categories, their roles, and representative protocols or studies. Complementary routing schemes, such as RTS, are explicitly distinguished from OR protocols.

The classification highlights that QoS support relies on complementary information sources and mechanisms whose joint optimization remains limited across the reviewed studies. This gap motivates multi-objective OR frameworks that integrate link and path performance, dynamic network state, coding decisions, flow-level resource control, security, mobility, and forwarding coordination according to application requirements.

5. Comparative Analysis and Open Issues

Table 1 compares the reviewed approaches using QoS metrics and parameters, target application, offered QoS, anti-duplication mechanism, mobility assumption, and simulation or optimization tool. Because the studies use different topologies, traffic models, network sizes, and evaluation platforms, the table is intended as a qualitative comparison of design choices rather than a direct numerical ranking.

5.1. Key Insights and Comparative Analysis

The comparison shows a progression from reliability-oriented forwarding toward resource-, security-, and context-aware mechanisms. EMOR and Fang et al. (2019) optimize transmission efficiency through power/rate adaptation, reception probability, and coding opportunities; OBOR and QADC-MORE incorporate buffer load, delay, flow progress, and scheduling; trust-based routing and RTS emphasize secure forwarding; and Calado et al. operate primarily at the admission/resource-reservation level. Across these categories, delay, PDR, throughput, packet loss, and energy are the most common QoS

measures, whereas jitter, fairness, congestion stability, mobility, and security are less consistently combined.

Coordination and duplication handling also vary substantially. Ordered forwarder sets and priority timers reduce duplicate forwarding in EMOR, MAMΔ uses relay-cache and route-control mechanisms, and coding-based approaches such as Fang et al. and QADC-MORE reduce redundancy indirectly through coded forwarding. Other approaches focus on security, analytical evaluation, or admission control and therefore do not define explicit packet-level duplicate suppression. Mobility remains limited as well: most evaluations assume static or low-mobility WMNs, while only a few consider mobile sinks or clients. Methodologically, the literature spans NS-2/NS-3, OMNeT++, MATLAB, shortest-path variants, DTMCs, coding, and credit scheduling, which further limits direct cross-study comparison.

Table 1. Qualitative comparison of the reviewed approaches

(a) Performance metrics, routing or modeling inputs, and QoS focus

Approach/study (year)	Performance metrics	Routing/modeling inputs	QoS focus
LSTM-based routing† (2023)	PDR; throughput	Sent and received packets; PDR; PLR; throughput; delay; jitter	Reliability; throughput
EMOR (2023)	PDR; delay; energy consumption	Link delivery probabilities; transmission rate and power; energy cost	Reliability; delay; energy efficiency
Zhao and Srivastava (2022)	PDR; overhead; packet loss; throughput; delay	Direct and indirect trust; social similarity	Reliable and trustworthy forwarding
OBOR (2021)	Capacity; delay; delivery ratio; energy consumption	Buffer occupancy; link state; achievable throughput	Delay reduction; load balancing
MAMΔ (2021)	PDR; delay; energy consumption	Hop count; discovery information; route-expiry parameter Δ	Data delivery; delay; energy efficiency
RTS† (2020)	Throughput; PLR; latency; overhead; energy efficiency	Link cost; packet loss information; node position; RSA keys	Reliability; data protection
Fang et al. (2019)	Expected coded transmission time	Reception probabilities; transmission rate; coding opportunities	Transmission-time reduction; coding gain
Darehshoorzadeh et al.‡ (2016)	Delivery probability; ExNT; expected hop count	Link delivery probabilities; retransmission limit	Analytical performance evaluation
Calado et al. (2015)	Admission success rate; reserved bandwidth	Available bandwidth; hard and soft QoS limits; ETX	Admission control; bandwidth reservation
QADC-MORE (2015)	Throughput; delivery delay	Batch delay; route length; service priority; forwarding credits; ETX	Fairness; service differentiation

Notes. † Complementary routing approach. ‡ Analytical performance model.

Abbreviations. QoS: quality of service; WMN: wireless mesh network; OR: Opportunistic Routing; PDR: packet delivery ratio; PLR: packet loss ratio; ETX: expected transmission count; ExNT: expected number of transmissions; DTMC: discrete-time Markov chain; RSA: Rivest–Shamir–Adleman cryptography; IoT: Internet of Things.

Table 1. Qualitative comparison of the reviewed approaches (continued)

(b) Applications, forwarding mechanisms, mobility, and evaluation

Approach/study	Target application	Duplicate control	Nodes mobility	Methods / evaluation
LSTM-based routing†	Broadband / multimedia	Not explicitly specified	Static	LSTM learning; NS-3; Deep Learning Studio
EMOR	Energy-efficient WMN routing	Priority-based reliable anycast	Static	Bellman–Ford-based optimization; NS-3
Zhao and Srivastava	Trust-aware mesh forwarding	Limited-copy forwarding	Mobile; random waypoint	Trust modeling; MATLAB
OBOR	Multimedia mesh traffic	Not explicitly specified	Static	Dijkstra-inspired routing; discrete-event simulation
MAMΔ	Data collection toward a mobile sink	Cache-based duplicate filtering for discovery messages	One mobile sink; fixed mesh nodes	OMNeT++; INET
RTS†	Secure IoT-oriented mobile WMNs	Not explicitly specified	Mobile	RSA cryptography; NS-3
Fang et al.	Multi-rate mesh communication	Not explicitly specified	Low mobility	State-graph optimization; network coding; NS-2
Darehshoorzadeh et al.‡	OR performance analysis	Perfect coordination assumed; timers tested in simulation	Static	DTMC; R; NS-2
Calado et al.	QoS-enabled opportunistic flows	Backoff-based aggregation of reservation requests	Static	Admission-control modeling; OMNeT++
QADC-MORE	Multiple concurrent mesh flows	Network coding; forwarding-credit control	Static	Dynamic credit scheduling; OMNeT++

Approach labels. LSTM: long short-term memory; EMOR: energy-efficient multi-rate Opportunistic Routing; OBOR: buffer occupancy and link state Opportunistic Routing; RTS: robust and trusted scheme; QADC-MORE: QoS-aware dynamic credit MORE; MORE: MAC-independent Opportunistic Routing and encoding; MAC: medium access control. MAMΔ denotes the reactive least-hop variant for a monitored arboretum mesh, with Δ controlling route expiry.

5.2. Mathematical Modeling Perspective

From a modeling perspective, the reviewed approaches represent routing decisions at different mathematical levels. EMOR (Khah et al., 2023) formulates energy-efficient forwarding through a distributed shortest-path-oriented optimization in which transmission rate, power, reception probability, and energy cost influence the forwarding decision. OBOR (Bordier et al., 2021) uses a delay-oriented cost that combines link throughput and buffer occupancy, thereby embedding dynamic network state into path selection. Fang et al. (2019) define an expected opportunistically coded transmission-time metric and use it to search for a forwarding scheme that jointly accounts for coding opportunities and

transmission rate. These formulations show that link-level and state-aware QoS can be expressed through cost functions whose variables describe both transmission conditions and resource availability. Analytical modeling introduces a different representation. The model of Darehshoorzadeh et al. (2016) describes packet forwarding as transitions in a Discrete-Time Markov Chain, with states determined by the current forwarding node and retransmission process. This makes it possible to derive delivery probability, expected transmissions, transmission distributions, and expected hop count. At the flow level, Calado et al. (2015) formulate admission decisions using bandwidth availability and QoS limits, while QADC-MORE (Abdolahi et al., 2015) incorporates batch delay, route length, flow progress, service priority, and dynamic credit scheduling. Thus, the literature ranges from deterministic cost-based optimization to stochastic performance models and resource-control mechanisms.

A common limitation is that these models generally optimize or analyze only a restricted subset of the QoS state. Link reliability, energy, congestion, buffer occupancy, bandwidth, security, mobility, and coordination are rarely represented within the same decision framework. This observation is consistent with the broader need for multi-objective optimization in WMNs (Amir et al., 2026). A more complete mathematical perspective should therefore connect candidate selection, prioritization, and coordination with the network state and the QoS objectives being optimized. Such integration would also make protocol assumptions and trade-offs more explicit and would provide a clearer basis for comparing solutions evaluated under heterogeneous simulation settings.

5.3. Open Issues

Three open issues emerge. First, no reviewed framework jointly integrates link quality, congestion, buffer occupancy, energy, security, and mobility. Second, candidate selection and route optimization receive more attention than the QoS impact of candidate coordination. Third, simplified static scenarios remain common, limiting generalization to dense, heterogeneous, interference-prone, and mobile environments.

Future OR designs should therefore combine multi-objective QoS optimization with adaptive candidate coordination and realistic mobility-aware evaluation. Learning-based methods such as reinforcement learning can support adaptation in dynamic environments (Krishnan et al., 2026), but they should be coupled with lightweight mathematical models so that computational and communication overhead do not offset QoS gains.

6. Conclusion

This paper reviewed QoS-aware OR approaches in WMNs and introduced a QoS-integration-centric taxonomy spanning link-level, state-aware, coding-aware, flow-level, security/trust-aware, mobility-aware, and analytical-modeling approaches. The comparative analysis shows that existing protocols usually optimize only a limited subset of QoS objectives and employ heterogeneous coordination, mobility, and evaluation assumptions.

The main implication is that future WMN routing should move from isolated QoS mechanisms toward adaptive multi-objective frameworks that jointly account for link quality, traffic state, resource availability, security, mobility, and duplicate suppression. Mathematical modeling can provide the structure needed to formalize these trade-offs, while realistic evaluation is required to assess their effectiveness under heterogeneous and dynamic mesh conditions.

References

Abdolahi, M., Eshghi, F., Kelarestaghi, M., & Bag-Mohammadi, M. (2015). QADC-MORE: A New QoS-Aware Dynamic Credit MORE Protocol for Wireless Mesh Networks. In *2015 IEEE Symposium on Computers and Communication (ISCC)* (pp. 883–888). IEEE. https://doi.org/10.1109/ISCC.2015.7405625

Amir, R., Naeem, H., Ali, A., & Gulzar, M. (2026). MultiObjective Optimization in Wireless Mesh Networks – A Survey. *ACM Computing Surveys, 58*(11), Article 294, 1–36. https://doi.org/10.1145/3800685

Bordier, J.-B., Merlhe, C., Fabian, P., Baey, S., Garnaud, D., Bussereau, K., Livolant, E., & Gueguen, C. (2021). Buffer Occupancy and Link State Opportunistic Routing for Wireless Mesh Networks. *Wireless Networks, 27*(6), 4133–4150. https://doi.org/10.1007/s11276-021-02736-6

Calado, I., Luiz, S. O. D., Soares, G., Almeida, H., & Perkusich, A. (2015). An Admission Control Mechanism for Dynamic QoS-Enabled Opportunistic Routing Protocols. *EURASIP Journal on Wireless Communications and Networking, 2015*, Article 224. https://doi.org/10.1186/s13638-015-0454-7

Darehshoorzadeh, A., De Grande, R. E., & Boukerche, A. (2016). Toward a Comprehensive Model for Performance Analysis of Opportunistic Routing in Wireless Mesh Networks. *IEEE Transactions on Vehicular Technology, 65*(7), 5424–5438. https://doi.org/10.1109/TVT.2015.2457680

Eyobu, O. S., & Edwinah, K. (2023). A Deep Learning-Based Routing Approach for Wireless Mesh Backbone Networks. *IEEE Access, 11*, 49509–49518. https://doi.org/10.1109/ACCESS.2023.3277431

Fang, A., Cui, L., Zhang, Z., Sheng, Z., Zhu, M., & Zhang, X. (2019). An Opportunistic Routing Strategy Based on Network Coding in Multi-Speed Processing Environment. In *Proceedings of the 2019 International Conference on Artificial Intelligence and Advanced Manufacturing (AIAM)* (pp. 1–6). Association for Computing Machinery. https://doi.org/10.1145/3358331.3358406

Haseeb, K., Din, I. U., Almogren, A., Islam, N., & Altameem, A. (2020). RTS: A Robust and Trusted Scheme for IoT-Based Mobile Wireless Mesh Networks. *IEEE Access, 8*, 68379–68390. https://doi.org/10.1109/ACCESS.2020.2985851

Khah, M. A., Moghim, N., Gholami, N., & Shetty, S. (2023). Energy-Efficient Multi-Rate Opportunistic Routing in Wireless Mesh Networks. *IEEE Access, 11*, 97466–97477. https://doi.org/10.1109/ACCESS.2023.3313096

Krishnan, S., Gu, Z., Park, J., Oh, S.-M., & Choi, J. (2026). Reinforcement Learning for Opportunistic Routing in Software-Defined LEO–Terrestrial Systems. *IEEE Wireless Communications Letters, 15*, 1817–1821. https://doi.org/10.1109/LWC.2026.3663306

Ouarab, N., Boulfekhar, S., Aissani, D., & Boumzaid, Y. (2025). The Contribution of Graph Theory to Opportunistic Routing in VANETs. In *Proceedings of the International Conference on Mathematics and Computers with Applications (MCWA 2025)* (pp. 480–488).

Paulon J. V., M., Olivieri de Souza, B. J., & Endler, M. (2021). Opportunistic Routing towards Mobile Sink Nodes in Bluetooth Mesh Networks. In *Proceedings of the 18th International Conference on Wireless Networks and Mobile Systems (WINSYS)* (pp. 67–75). SciTePress. https://doi.org/10.5220/0010557000670075

Ryu, J., & Kim, S. (2025). Mitigating Jamming Attacks in Underwater Sensor Networks Using M-Qubed-Based Opportunistic Routing Protocol. *ETRI Journal, 47*(3), 559–571. https://doi.org/10.4218/etrij.2023-0526

Wan, L., & Cheng, W. (2026). A Normative Algorithm for Wireless Multimedia Broadcast Retransmission Using Generative Adversarial Network Coding. *Discover Applied Sciences, 8*, Article 209. https://doi.org/10.1007/s42452-025-08214-4

Xu, H., & Wang, Y. (2024). SROR: A Secure and Reliable Opportunistic Routing for VANETs. *Vehicles, 6*(4), 1730–1751. https://doi.org/10.3390/vehicles6040084

Zhao, Y., & Srivastava, G. (2022). A Wireless Mesh Opportunistic Network Routing Algorithm Based on Trust Relationships. *IEEE Access, 10*, 4786–4793. https://doi.org/10.1109/ACCESS.2021.3138370

Cardinality-Constrained Risk Parity on a Sharpe-Filtered Subset of the BIST-100 Index

Çağrı Latifoğlu*

Consultkitapp LTD., Ankara, Turkiye
Industrial Engineering Department, Antalya Bilim University, Antalya, Turkiye
cagrilatifoglu@consultkit.app

Abstract

Risk parity allocates capital so that each asset contributes equally to portfolio risk, delivering diversification without expected-return estimates. In noisy universes such as emerging markets, however, the sample covariance matrix is unstable, which makes risk-parity weights unreliable. We study two remedies, a Sharpe-ratio screen that drops assets with poor historical risk-adjusted characteristics, and a cardinality constraint that limits the number of held securities, and evaluate five allocation strategies: equal weight on the full universe; risk parity on the full and on the Sharpe-filtered asset space; and cardinality-constrained risk parity on the full and on the Sharpe-filtered asset space. The strategies are implemented as conic and mixed-integer conic programs and tested on the BIST-100 index under a walk-forward protocol with a 126-day estimation window, a 21-day hold, monthly rebalancing, and a 40% annual risk-free rate. Preliminary out-of-sample results over 17 months show that the Sharpe filter improves performance in every universe examined, and that, on the 30-stock universe, cardinality-constrained risk parity on the filtered space is the best-performing strategy and the only one to deliver a positive excess return.

Keywords: Risk parity, cardinality constraints, mixed-integer conic programming

1. Introduction

Risk parity allocates capital so that each asset contributes equally to portfolio risk (Qian et al., 2005; Maillard et al., 2010). Because the allocation is driven by the covariance structure rather than by expected returns, it provides diversification without expected-return estimates, which are notoriously difficult to estimate reliably. A practical implementation of risk parity is the generalized (conic) formulation of Costa and Kwon (2020), in which the equal-risk-contribution objective is expressed with rotated-quadratic and exponential cones and solved with a conic solver. In noisy universes, emerging markets first among them, the sample covariance matrix is unstable, and the resulting risk-parity weights are unreliable. We examine two remedies:

- Sharpe screen: drop assets with poor historical risk-adjusted characteristics, reducing the covariance-estimation noise that enters the allocation;
- Cardinality constraint: limit the number of held securities, curbing both estimation error and turnover (Anis & Kwon, 2022).

We test five treatments, equal weight (T1), risk parity on the full universe (T2) and on the Sharpe-filtered subset (T3), and cardinality-constrained risk parity (CC-parity) on the full universe (T4) and on the Sharpe-filtered subset (T5), in two walk-forward experiments on the BIST-100 index (Borsa İstanbul's benchmark equity index): a 30-stock universe (Experiment 1) and a 96-ticker universe (Experiment 2). All optimisation-based treatments are solved as conic or mixed-integer conic programs, so performance differences reflect the remedies rather than solver artefacts.

* *Corresponding Author*

2. Data and Backtesting Protocol

We use BIST-100 daily adjusted closes (BIST-100 is Borsa İstanbul's benchmark large-cap equity index; BIST30 is its 30-stock large-cap subset). The full universe comprises 96 out of 102 tickers; the BIST30 subset comprises 30 large caps. The sample spans roughly six years of training, with the out-of-sample (OOS) period covering the last 17 months (March 2025–July 2026). The estimation window is 126 trading days; the hold period is 21 trading days; rebalancing is monthly with the decision taken at month-end. Transaction costs are not considered. The protocol yields 53 training windows and 17 OOS windows. The risk-free rate is $r_f = 40\%$ per annum, the Turkish policy rate over the window. The conic formulations are solved with MOSEK (MOSEK ApS, 2025). At each decision date, the annualised Sharpe ratio of every asset is computed over the 126-day lookback as the ratio of the mean to the standard deviation of daily excess returns, scaled by $\sqrt{252}$. The filtered asset space is

$$\mathcal{M} = \{\, i : \mathrm{Sharpe}_i \geq 0.75 \,\} \tag{1}$$

A guard clause applies: if fewer than four assets pass the screen, the top-10 assets by Sharpe are taken instead. The screen is static within a decision window: the asset space is fixed at the decision date and used over the 21-day hold. Performance is summarised by four statistics: the mean OOS Sharpe ratio (the average, across the 17 OOS windows, of each window's annualised Sharpe ratio of realised excess returns); the compound annual growth rate (CAGR) of the OOS wealth curve; the maximum drawdown (Max DD), i.e., the largest peak-to-trough decline of the cumulative wealth curve; and the final net asset value (NAV) of a strategy started with unit wealth. Pairwise performance differences are assessed with Wilcoxon signed-rank tests applied across the 17 OOS months. Table 1 summarises the five treatments evaluated in the two experiments; in T4 and T5 the cardinality bound is $K = \min(10, \lfloor n/2 \rfloor)$, with a lower bound of 2, where n is the size of the asset space.

Table 1. Treatments evaluated in the two experiments

Treatment	Model	Asset space
T1	equal weight	full
T2	risk parity	full
T3	risk parity	filtered
T4	CC-parity ($K = \min(10, \lfloor n/2 \rfloor)$)	full
T5	CC-parity ($K = \min(10, \lfloor n/2 \rfloor)$)	filtered

CC-parity: cardinality-constrained risk parity.

3. Models

Throughout this section, $\Sigma \in \mathbb{R}^{n \times n}$ denotes the sample covariance matrix of daily returns estimated over the 126-day lookback window, and $G \in \mathbb{R}^{n \times n}$ a matrix factor with $\Sigma = GG^\top$ (e.g., the Cholesky factor).

3.1. Model 1: Equal Weight (T1)

The equal-weight portfolio assigns

$$x_i = 1/n, \; i = 1, \ldots, n \tag{2}$$

where n is the size of the asset space. It is the naive diversification benchmark (DeMiguel et al., 2009): no estimation and no optimisation are involved, making it the reference point for all other treatments. The asset space is the full universe.

3.2. Model 2: Risk Parity (T2 / T3)

The risk-parity allocation is the generalized conic program of Costa and Kwon (2020):

$$\min_{x,t,r} \; r - c\, b^{\top} t \tag{3}$$

s.t.

$$(1, r, G^{\top} x) \in \mathcal{K}_r \tag{4}$$

$$(x_i, 1, t_i) \in \mathcal{K}_{\exp}, \;\; \forall i \in \{1, \dots, n\} \tag{5}$$

$$x > 0 \tag{6}$$

where $x \in \mathbb{R}^n$ are the (unnormalised) portfolio weights, kept strictly positive by (6); $\mathcal{K}_r = \{(u, v, w) \in \mathbb{R} \times \mathbb{R} \times \mathbb{R}^k : 2uv \geq \| w \|_2^2, \; u \geq 0, \; v \geq 0\}$ is the rotated quadratic cone; and $\mathcal{K}_{\exp} = \{(u, v, w) \in \mathbb{R}^3 : u \geq v e^{w/v}, \; u \geq 0, \; v > 0\}$ is the exponential cone, so that (5) is equivalent to $x_i \geq e^{t_i}$, i.e., $t_i \leq \ln x_i$, with $t \in \mathbb{R}^n$ collecting these logarithmic-barrier variables. Constraint (4) enforces $r \geq 1/2 \, \| G^{\top} x \|_2^2 = 1/2 \, x^{\top} \Sigma x$, so r is an epigraph variable for half the portfolio variance (not the standard deviation). Minimising (3) is therefore equivalent to minimising the convex log-barrier function $1/2 \, x^{\top} \Sigma x - c \sum_i b_i \ln x_i$, whose optimality conditions give $x_i (\Sigma x)_i = c \, b_i$ for every asset: asset i contributes the fraction b_i of the total portfolio variance. Here $b \in \mathbb{R}^n$ is the risk-budget vector and $c = 1 > 0$ a scaling constant; the solution is rescaled to unit total weight after solving, which leaves the equal-risk-contribution property unchanged. The budget is uniform over the asset space $\mathcal{A} \subseteq \{1, \dots, n\}$:

$$b_i = 1/|\mathcal{A}| \tag{7}$$

Treatment T2 uses the full universe ($\mathcal{A}$ of size n); treatment T3 uses the Sharpe-filtered subset ($\mathcal{A} = \mathcal{M}$, of size $n_x = |\mathcal{M}|$).

3.3. Model 3: Cardinality-constrained Risk Parity (T4 / T5)

The log-barrier program (3)-(6) cannot be combined directly with binary asset selection: the barrier terms $t_i \leq \ln x_i$ and the strict positivity requirement (6) are defined only for strictly positive weights, whereas cardinality selection forces $x_i = 0$ for every excluded asset. Following Anis and Kwon (2022), we therefore replace the logarithmic barrier with an explicit penalty on the deviation of the selected assets' risk contributions from a common target level. Schematically, the model is

$$\min_{x,y} \; D(x, y) \tag{8}$$

s.t.

$$\sum_{i=1}^{n} x_i = 1, \;\; x \geq 0 \tag{9}$$

$$\sum_{i=1}^{n} y_i = K, \;\; y_i \geq x_i \;\; \forall i, \;\; y_i \in \{0,1\} \tag{10}$$

where $y \in \{0,1\}^n$ is the vector of binary selection variables, exactly K assets are selected, and the linking constraint $y_i \geq x_i$ (well defined since $0 \leq x_i \leq 1$) forces $y_i = 1$ whenever asset i receives positive weight, so at most K assets are held. $D(x, y)$ measures the total deviation, across the selected assets, of the risk contributions $x_i (\Sigma x)_i$ from their target; it is finite whenever $x \geq 0$, so zero weights for excluded assets are admissible.

The formulation implemented in the experiments is the conic mixed-integer program of Anis and Kwon (2022), which instantiates (8)-(10):

$$\min_{x,y,d,w,\theta_l,\theta_a,z,r,dd} \; dd + \alpha\,\theta_a \tag{11}$$

subject to:

$$z = \Sigma x \tag{12}$$

$$(0.5\,z_i, x_i, \theta_{l,i}) \in \mathcal{K}_r,\ \forall i \in \{1,\dots,n\} \tag{13}$$

$$w_i \geq |\theta_a - \theta_{l,i}|,\ \forall i \in \{1,\dots,n\} \tag{14}$$

$$d_i \geq w_i - M(1-y_i),\ \forall i \in \{1,\dots,n\} \tag{15}$$

$$(r, G^\top x) \in \mathcal{K}_q,\ \sqrt{K}\,\theta_a \geq r \tag{16}$$

$$(0.5, dd, d) \in \mathcal{K}_r \tag{17}$$

$$y_i \geq x_i,\ \forall i \in \{1,\dots,n\} \tag{18}$$

$$\sum_{i=1}^{n} x_i = 1,\ \sum_{i=1}^{n} y_i = K \tag{19}$$

where $\mathcal{K}_q = \{(s,v) \in \mathbb{R} \times \mathbb{R}^k : s \geq \| v \|_2\}$ is the standard quadratic cone and $\mathcal{K}_r$ is the rotated quadratic cone of Section 3.2. The variables are: x $\in \mathbb{R}^n$, the nonnegative portfolio weights ($x_i \in [0,1]$ follows from (19), and $x \geq 0$ is enforced by the cone constraints (13)); y $\in \{0,1\}^n$, the binary selection variables, with (18)-(19) selecting exactly K assets and forcing $y_i = 1$ whenever $x_i > 0$; z $= \Sigma x \in \mathbb{R}^n$, whose i-th entry is asset i's marginal contribution to portfolio variance, so that $x_i z_i$ is asset i's contribution to total variance ($\sum_i x_i\, z_i = x^\top \Sigma x = r^2$ at an optimal solution); $\theta_{l,i}$, a lower bound on the risk contribution of asset i; θ_a, the common target contribution; w and d, intermediate deviation variables; r, in this model the portfolio standard deviation, $r \geq \| G^\top x \|_2 = \sqrt{x^\top \Sigma x}$ (unlike in (4), where the same symbol epigraphs half the variance); and dd, the total squared deviation.

Constraint (13) enforces $x_i z_i \geq \theta_{l,i}^2$ (the cone also forces $z_i \geq 0$), i.e., $\theta_{l,i} \leq \sqrt{x_i z_i}$, the geometric mean of the weight x_i and the marginal contribution z_i; (14) bounds the deviation of asset i's risk contribution from the target θ_a; (15) counts this deviation only for the selected assets ($y_i = 1$), the big-M constant (here $M = 1000$) deactivating it for the excluded assets ($y_i = 0$); (16) ties the target to total risk, with K assets in exact parity each contributes r^2/K to the variance, so the target level is $\theta_a = r/\sqrt{K}$, whose lower bound $\theta_a \geq r/\sqrt{K}$ is enforced by (16); and (17) is equivalent to $dd \geq \| d \|_2^2$.

The objective (11) minimises the total parity deviation dd plus $\alpha\,\theta_a$, where $\alpha = 0.01$ is a fixed weight on the target term, which through (16) also penalises total risk. When the deviation can be driven to zero, every selected asset satisfies $x_i(\Sigma x)_i = r^2/K$, i.e., exact risk parity over the selected assets; in general the model is a convex mixed-integer approximation of risk parity over the support. The resulting mixed-integer conic program (MICP) is solved with MOSEK. The cardinality bound is $K = \min(10, \lfloor n/2 \rfloor)$, with a lower bound of 2, where n is the size of the asset space. Treatment T4 uses the full universe; treatment T5 uses the Sharpe-filtered subset.

4. Results and Discussion

4.1. Experiment 1: BIST30

The universe is the 30 large-cap BIST-100 constituents, and all five treatments (T1–T5) are evaluated. All treatments are deterministic given the input data. The protocol is as in Section 2: 126-day window, 21-day hold, 17 OOS months, $r_f = 40\%$. Table 2 reports the OOS performance of the five treatments.

Table 2. Experiment 1 (BIST30, $n = 30$): preliminary OOS results, $r_f = 40\%$

Treatment	Mean OOS Sharpe	CAGR	Max DD	Final NAV
T1 equal weight (full)	−0.53	23.5%	−16.0%	1.33
T2 risk parity (full)	−0.43	27.0%	−15.0%	1.38
T3 risk parity (filtered)	−0.19	33.8%	−14.3%	1.46
T4 CC-parity (full)	−0.21	36.0%	−13.9%	1.52
T5 CC-parity (filtered)	0.37	59.4%	−13.0%	1.90

Only T5 delivers a positive excess return at the 40% risk-free rate, and T5 significantly outperforms every other treatment (Wilcoxon signed-rank, p = 0.002). Within this experiment, cardinality plus filtering dominate: both cardinality treatments improve on their non-cardinality counterparts (T4 over T2 on the full space; T5 over T3 on the filtered space), and T5 (CC-parity on the filtered space) is the best treatment. In this small, noisy universe, parsimony wins.

4.2. Experiment 2: BIST100

The universe is the 96 tickers of BIST-100; the cardinality treatments T4/T5 are excluded by design, so the Sharpe screen is evaluated on the larger universe. The protocol is identical: 126-day window, 21-day hold, 17 OOS months, rf = 40%. Table 3 reports the OOS performance of the three treatments.

Table 3. Experiment 2 (BIST-100, $n = 96$): preliminary OOS results, $r_f = 40\%$

Treatment	Mean OOS Sharpe	CAGR	Max DD	Final NAV
T1 equal weight (full)	−0.50	28.3%	−12.7%	1.43
T2 risk parity (full)	−0.32	33.7%	−12.9%	1.51
T3 risk parity (filtered)	0.30	55.8%	−13.4%	1.88

Only the filtered-space treatment T3 delivers a positive excess return at $r_f = 40\%$. The Sharpe filter is the dominant effect: T3 vs. T2, +0.62 Sharpe ($p = 0.005$). Because the cardinality treatments are not evaluated in this experiment, the comparison isolates the effect of the filter, and no cardinality effect can be identified on the 96-stock universe; among the treatments considered, filtered parity (T3) is the best.

4.3. Synthesis

Two observations emerge across the two experiments. First, the Sharpe filter improves performance in every universe examined. Second, within the 30-stock experiment, cardinality improves on both asset spaces (T4 over T2, T5 over T3), and the best treatment overall is CC-parity on the filtered space (T5). On the 96-stock universe, where the cardinality treatments were not evaluated, the Sharpe filter alone drives the improvement and plain filtered parity (T3) is the best of the treatments considered. Because cardinality was not tested on the 96-stock universe, our results do not establish whether the cardinality benefit depends on universe size; this is left for future work. Table 4 summarises the best treatment by experiment.

Table 4. Best-performing treatment by experiment (preliminary)

Experiment	Universe (size)	Filtered subset size (range)	Treatments evaluated	Best treatment
1	BIST30 ($n = 30$)	4–10	T1–T5	CC-parity on the filtered space (T5)

2	BIST-100 ($n = 96$)	15–53	T1–T3	Risk parity on the filtered space (T3)

Note: the cardinality-constrained treatments (T4, T5) were not evaluated in Experiment 2, so no cardinality effect can be identified on the 96-stock universe.

5. Conclusion

Sharpe screening substantially improves risk-parity performance on the BIST-100 in both experiments, net of a 40% risk-free rate. On the 30-stock universe, cardinality-constrained risk parity on the Sharpe-filtered subset is the best-performing treatment and the only one to deliver a positive excess return; on the 96-stock universe, where the cardinality-constrained variants were not evaluated, the Sharpe filter alone drives the improvement. Since cardinality was not tested on the larger universe, no conclusion about the role of universe size is warranted; evaluating cardinality-constrained risk parity on the full BIST-100 is a natural next step. These preliminary results suggest that, in noisy emerging-market settings, parsimony, screening and, where tested, cardinality, is an effective remedy for the instability of risk-parity weights.

Acknowledgements

Declaration of generative AI and AI-assisted technologies in the manuscript preparation process is as follows. During the preparation of this work, the author used: Google Gemini AI and locally hosted various LLMs for research brainstorming, coding, LaTeX syntax correction, results tabulation, text summarization and synthesis. After using these tools/services, the author reviewed and edited the content as needed and takes full responsibility for the content of the published article.

References

Anis, H. T., & Kwon, R. H. (2022). Cardinality-constrained risk parity portfolios. European Journal of Operational Research, 302(1), 392–402.

Costa, G., & Kwon, R. H. (2020). Generalized risk parity portfolio optimization: An ADMM approach. Journal of Global Optimization, 78(1), 207–238.

DeMiguel, V., Garlappi, L., & Uppal, R. (2009). Optimal versus naive diversification: How inefficient is the 1/N portfolio strategy? Review of Financial Studies, 22(5), 1915–1953.

Maillard, S., Roncalli, T., & Teïletche, J. (2010). The properties of equally weighted risk contribution portfolios. Journal of Portfolio Management, 36(4), 60–83.

MOSEK ApS. (2025). MOSEK Portfolio Optimization Cookbook (Version 1.6.0).

Qian, E., Sorel, A., & Getzmann, A. (2005). Risk parity portfolios: Efficient portfolios through true diversification. Panagora Asset Management, 1(1), 1–10.

Mixed Sumudu–Adomian Method for Two-Dimensional Nonlinear Fuzzy Integral Equations

Artan F. Alidema[1*], Frederik Dara[2]

[1] *University of Prishtina, Department of Mathematics, Faculty of Mathematical and Natural Science, Prishtina, Kosovo*
[2] *University of Tirana, Department of Applied Mathematics, Faculty of Natural Science, Tirana, Albania*
artan.alidema@uni-pr.edu, frederik.dara@fshn.edu.al

Abstract

A numerical method is proposed for solving two-dimensional nonlinear Volterra–Fredholm fuzzy integral equations (2D-NVFFIEs) of the second kind. First, using the α-cut representation, the fuzzy integral equation is transformed into a system of crisp nonlinear Volterra–Fredholm integral equations. The Sumudu transform is then combined with the Adomian Decomposition Method to construct a direct analytical–numerical scheme through successive approximations. Furthermore, the existence and uniqueness of the fuzzy solution are established, and the conditional convergence of the proposed MSADM scheme is theoretically analysed.

Keywords: Fuzzy integral equations, Sumudu transform, mixed Sumudu–Adomian decomposition method

1. Introduction

Fuzzy differential and integral equations constitute an important area of fuzzy analysis, with applications in mathematical modeling, numerical analysis, and control theory. The fundamental concepts of fuzzy calculus and fuzzy differential equations have been developed through several important approaches (Dubois & Prade, 1982a, 1982b,1982c; Goetschel & Voxman, 1986; Kaleva, 1987; Seikkala, 1987). The theory of fuzzy integral equations has subsequently received considerable attention, including questions concerning existence, uniqueness, boundedness, and numerical approximation (Mordeson & Newman, 1995). Several numerical and semi-analytical methods have been proposed for solving fuzzy integral equations. Among them, the Adomian Decomposition Method (ADM) is particularly useful for nonlinear problems because it represents the unknown function as a series and decomposes nonlinear terms into Adomian polynomials (Adomian, 1988, 1994). The convergence of ADM for nonlinear integral equations has also been investigated (El-Kalla, 2008). In the fuzzy setting, ADM has been applied to Fredholm integral equations and other classes of fuzzy integral equations (Abbasbandy & Allahviranloo, 2006; Babolian et al., 2005). Its application has subsequently been extended to two-dimensional nonlinear fuzzy Volterra and Volterra–Fredholm integral equations (Alidema & Georgieva, 2018; Georgieva, 2018). Other approaches, including homotopy perturbation methods, have also been investigated for multidimensional fuzzy integral equations (Alidema & Georgieva, 2019). Integral transforms provide another effective framework for the treatment of differential and integral equations. In particular, the Sumudu transform has useful operational properties for constructing semi-analytical solutions. Its fuzzy extension has been applied to fuzzy fractional differential equations and fuzzy Volterra integral equations (Abdul Rahman & Ahmad, 2017a, 2017b), while Jafari and Razvarz (2018)

* *Corresponding Author*

investigated its application to fuzzy differential equations. Sumudu-based decomposition techniques have also been employed for nonlinear Volterra–Fredholm fractional integro-differential equations and nonlinear systems involving Fredholm and Volterra operators (Amer et al., 2018; Al-Khaled & Yousef, 2019).

For two-dimensional fuzzy problems, the double fuzzy Sumudu transform provides a natural extension of the transform technique. Its application to fuzzy Volterra integral equations was investigated by Alidema and Georgieva (2019), while Alidema (2022) combined the double fuzzy Sumudu transform with ADM for two-dimensional fuzzy Volterra integral equations.

In this paper, we develop a Mixed Sumudu Transform–Adomian Decomposition Method (MSADM) for solving two-dimensional nonlinear fuzzy Volterra–Fredholm integral equations of the second kind (2D-NVFFIEs). The proposed method combines the Sumudu transform with the Adomian decomposition procedure, while preserving the mixed structure of the Fredholm, Volterra, and Volterra–Fredholm operators. The nonlinear terms are represented by Adomian polynomials, and a recursive sequence of approximate fuzzy-valued solutions is constructed. A numerical example is presented to demonstrate the applicability and effectiveness of the proposed method.

$$u(s,t) = g(s,t) \oplus (FR)\int_a^b k_1(s,t,x) \odot G_1(u(x,t))\,dx \oplus (FR)\int_c^t k_2(s,t,y) \odot G_2(u(s,y))\,dy \oplus (FR)\int_c^t (FR)\int_a^b k_3(s,t,x,y) \odot G_3(u(x,y))\,dx\,dy, \quad (1)$$

where $g,u: A = [a,b] \times [c,d] \to E^1$ are continuous fuzzy-number valued functions, $k_1: A \times [a,b] \to \mathbb{R}^+$, $k_2: A \times [c,d] \to \mathbb{R}^+$, $k_3: A \times A \to \mathbb{R}^+$and $G_1, G_2, G_3: E^1 \to E^1$are continuous functions. The set E^1 is the set of all fuzzy numbers.

2. Preliminaries

In this section, we briefly review the essential definitions and preliminary results on fuzzy numbers and fuzzy-number-valued functions that will be used throughout the paper.

Definition 1(R. Goetschel, W. Voxman, 1986). A fuzzy number is a function $u: \mathbb{R} \to [0,1]$satisfying the following properties: u is upper semi-continuous on $\mathbb{R}$, $u(x) = 0$ outside of some interval $[c,d]$, there are the real numbers a and b with $c \le a \le b \le d$, such that u is increasing on $[c,a]$, decreasing on $[b,d]$ and $u(x) = 1$ for each $x \in [a,b]$. u is fuzzy convex set i.e. $u(\lambda x + (1-\lambda)y) \ge minu(x), u(y)$ for all $x, y \in \mathbb{R}$ and $\lambda \in [0,1]$.

The set of all fuzzy numbers is denoted by E^1. Any real number $a \in \mathbb{R}$ can be interpreted as a fuzzy number $\tilde{a} = \chi[a]$ and therefore $\mathbb{R} \subset E^1$.

According to Wu and Gong (2001) for any $0 < r \le 1$ we denote the r-level set $[u]r = x \in \mathbb{R}: u(x) \ge r$ that is a closed interval and $[u]r = [u - r, u + r]$ for all $r \in [0,1]$. These lead to the usual parametric representation of a fuzzy number, by an ordered pair of functions $(u - r, u + r)$, which satisfies the following properties: $u - r$ is bounded left continuous non-decreasing function over $[0,1], u + r$ is bounded left continuous non-increasing function over $[0,1]$ and $u - r \le u + r$.

For $u, v \in E^1$, $k \in \mathbb{R}$, the addition and the scalar multiplication are defined by:

- $[u \oplus v]^r = [u]^r + [v]^r = [u_-^r + v_-^r, u_+^r + v_+^r]$
- $[k \odot u]^r = k \cdot [u]^r = [ku_-^r, ku_+^r]$ (if $k \ge 0$) or $[ku_+^r, ku_-^r]$ (if $k < 0$) for all $r \in [0,1]$.

The neutral element respect to in E^1 denoted by $\mathfrak{0} = \chi[0]$.
As a distance between fuzzy numbers, we use the Hausdorff metric defined by $D(u,v) = \sup_{r\in[0,1]} \max\{|u_-^r - v_-^r|, |u_+^r - v_+^r|\}$ for any $u, v \in E^1$.

Definition 2 (Wu & Wu, 1997). A fuzzy-number-valued function $f: A \to E^1$ is said to be continuous at $(s_0, t_0) \in A$ if for each $\varepsilon > 0$ there is $\delta > 0$ such that $D\big(f(s,t), f(s_0,t_0)\big) < \varepsilon$ whenever $((s-s_0)^2 + (t-t_0)^2)^{\frac{1}{2}} < \delta$. If f is continuous at each $(s,t) \in A$, then we say that f is continuous on A. On the set $C(A, E^1) = \{f: A \to E^1;\ f \text{ is continuous}\}$, there is defined the metric
$D^*(f,g) = \max_{(s,t)\in A} D\big(f(s,t), g(s,t)\big)$, for all $f, g \in C(A, E^1)$.
We see that $(C(A, E^1), D^*)$ is a complete metric space.

Definition 3 (Wu & Gong, 2001). Let $f: A \to E^1$, for $\Delta_x^n: a = x_0 < x_1 < \cdots < x_n = b$ and $\Delta_y^n: c = y_0 < y_1 < \cdots < y_n = d$, be two partitions of the intervals $[a,b]$ and $[c,d]$, respectively. Let one consider the intermediate points $\xi_i \in [x_{i-1}, x_i]$, $\eta_j \in \big[y_{j-1}, y_j\big]$, $i = 1, \dots, n$; $j = 1, \dots, n$, and $\delta: [a,b] \to \mathbb{R}^+$, $\sigma: [c,d] \to \mathbb{R}^+$. The divisions $P_x = ([x_{i-1}, x_i]; \xi_i)$, $i = 1, \dots, n$, and $P_y = \big(\big[y_{j-1}, y_j\big]; \eta_j\big)$, $j = 1, \dots, n$, are said to be δ-fine and σ-fine, respectively, if $[x_{i-1}, x_i] \subseteq \big(\xi_i - \delta(\xi_i), \xi_i + \delta(\xi_i)\big)$ and $\big[y_{j-1}, y_j\big] \subseteq \big(\eta_j - \sigma(\eta_j), \eta_j + \sigma(\eta_j)\big)$.

The function f is said to be two-dimensional Henstock integrable to $I \in E^1$ if for every $\varepsilon > 0$ there are functions $\delta: [a,b] \to \mathbb{R}^+$, $\sigma: [c,d] \to \mathbb{R}^+$ such that for any δ-fine and σ-fine divisions we have

$$D\left(\sum_{j=1}^{n}\sum_{i=1}^{n}(x_i - x_{i-1})\,(y_j - y_{j-1}) f(\xi_i, \eta_j),\ I\right) < \varepsilon,$$

where $\sum$ denotes the fuzzy summation.

3. Mixed Sumudu–Adomian Decomposition Method (MSADM)

In this section, we introduce the parametric formulation of integral equation (1) and develop the Mixed Sumudu–Adomian Decomposition Method (MSADM). We first describe the endpoint formulation for continuous nonlinearities and kernels of arbitrary sign. For the recurrence relations derived below, we then restrict our attention to nonnegative kernels and nondecreasing nonlinear functions on the relevant fuzzy intervals.

Let $A = [a,b] \times [c,d]$ and let $u, g: A \to E^1$ be fuzzy-number-valued functions with r-level sets

$$[u(s,t)]^r = \big[\underline{u}(s,t,r), \overline{u}(s,t,r)\big], \qquad [g(s,t)]^r = \big[\underline{g}(s,t,r), \overline{g}(s,t,r)\big], \qquad 0 \le r \le 1.$$

Assume that $G_i: \mathbb{R} \to \mathbb{R}$ $(i = 1,2,3)$ are continuous on the relevant intervals. For $\underline{u} \le \overline{u}$, define

$$H_i(\underline{u}, \overline{u}) = \min_{\underline{u}\le\beta\le\overline{u}} G_i(\beta), \qquad F_i(\underline{u}, \overline{u}) = \max_{\underline{u}\le\beta\le\overline{u}} G_i(\beta).$$

Continuity ensures that these extrema exist, and the extension principle yields

$$[G_i(u)]^r = \big[H_i(\underline{u}, \overline{u}), F_i(\underline{u}, \overline{u})\big].$$

For a real-valued kernel k_i, the endpoints of the product $k_i G_i(u)$ are

$$\underline{\left(k_i G_i(u)\right)} = \begin{cases} k_i H_i\left(\underline{u}, \overline{u}\right), & k_i \geq 0, \\ k_i F_i\left(\underline{u}, \overline{u}\right), & k_i < 0, \end{cases}$$
$$\overline{\left(k_i G_i(u)\right)} = \begin{cases} k_i F_i\left(\underline{u}, \overline{u}\right), & k_i \geq 0, \\ k_i H_i\left(\underline{u}, \overline{u}\right), & k_i < 0. \end{cases}$$

Thus, nonmonotone nonlinearities and sign-changing kernels require the corresponding interval bounds. In the sequel we assume $k_i \geq 0$ and G_i nondecreasing, so that $H_i = G_i\left(\underline{u}\right)$ and $F_i = G_i(\overline{u})$. Under these assumptions, the parametric form of (1) is

$$\begin{aligned} \underline{u}(s,t,r) = \quad & \underline{g}(s,t,r) + \int_a^b k_1(s,t,x) G_1\left(\underline{u}(x,t,r)\right) dx \\ & + \int_c^t k_2(s,t,y) G_2\left(\underline{u}(s,y,r)\right) dy \\ & + \int_c^t \int_a^b k_3(s,t,x,y) G_3\left(\underline{u}(x,y,r)\right) dx\, dy, \end{aligned} \tag{2}$$

$$\begin{aligned} \overline{u}(s,t,r) = \quad & \overline{g}(s,t,r) + \int_a^b k_1(s,t,x) G_1\left(\overline{u}(x,t,r)\right) dx \\ & + \int_c^t k_2(s,t,y) G_2\left(\overline{u}(s,y,r)\right) dy \\ & + \int_c^t \int_a^b k_3(s,t,x,y) G_3\left(\overline{u}(x,y,r)\right) dx\, dy. \end{aligned} \tag{3}$$

3.1. Double Sumudu Transform

For a suitable scalar function f on $[0,\infty)^2$, the double Sumudu transform is defined by

$$\mathcal{S}_2[f](p,q) = \int_0^\infty \int_0^\infty e^{-(x+y)} f(px, qy)\, dx\, dy, \qquad p,q > 0,$$

provided the integral exists. Equivalently,

$$\mathcal{S}_2[f](p,q) = \frac{1}{pq} \int_0^\infty \int_0^\infty e^{-s/p - t/q} f(s,t)\, ds\, dt.$$

On a function class where the inverse exists, $\mathcal{S}_2^{-1}\left[\mathcal{S}_2[f]\right] = f$. The transform acts componentwise on the fuzzy endpoints:

$$\mathcal{S}_2[u] = \left(\mathcal{S}_2\left[\underline{u}\right], \mathcal{S}_2[\overline{u}]\right).$$

Domain convention. For the transform presentation, assume $0 \leq a < b$ and $0 \leq c < d$. Every scalar function defined on A to which $\mathcal{S}_2$ is applied (including each complete integral contribution) is extended by zero to $[0,\infty)^2$; inversion is understood on this extended function, followed by restriction to A. The endpoint functions and all transformed expressions are assumed to belong to a class for which the

transform and its inverse are valid. This convention is an algebraic transform–inverse representation and does not assert a convolution theorem for general mixed kernels. For other endpoints a, c, a coordinate shift and corresponding transformed operators must be specified.

3.2. Adomian Decomposition Method

The lower and upper endpoint solutions are formally expanded as

$$\underline{u}(s,t,r) = \sum_{n=0}^{\infty} \underline{u}_n(s,t,r), \qquad \overline{u}(s,t,r) = \sum_{n=0}^{\infty} \overline{u}_n(s,t,r).$$

For a sufficiently differentiable scalar nonlinear map G_i, the associated Adomian polynomials are

$$A_{i,n} = \frac{1}{n!}\frac{d^n}{d\lambda^n} G_i\left(\sum_{j=0}^{\infty} \lambda^j u_j\right)\Bigg|_{\lambda=0}, \qquad i = 1,2,3.$$

For example, if $G_i(z) = z^2$, then

$$A_{i,0} = u_0^2, \quad A_{i,1} = 2u_0u_1, \quad A_{i,2} = u_1^2 + 2u_0u_2, \quad A_{i,3} = 2u_0u_3 + 2u_1u_2.$$

Here the square map is nondecreasing on $[0,\infty)$, but not on the whole real line. In the fuzzy parametric system, the lower and upper Adomian polynomials must correspond to the actual endpoint nonlinearities. If the G_i are nonmonotone, the min–max endpoint maps defined in Section 3 replace the direct evaluations, provided the relevant differentiability conditions hold.

3.3. MSADM Recurrence Relations

Apply $\mathcal{S}_2$ to equations (2) – (3), expand the endpoint nonlinearities in Adomian polynomials, and apply $\mathcal{S}_2^{-1}$. Set

$$\underline{u}_0 = \underline{g}, \quad \overline{u}_0 = \overline{g}, \qquad \underline{U}_0 = \mathcal{S}_2\left[\underline{g}\right], \quad \overline{U}_0 = \mathcal{S}_2[\overline{g}].$$

For $i = 1,2,3$ and $n \geq 0$, define the endpoint polynomials under the present monotonicity assumption by

$$\underline{A}_{i,n} = \frac{1}{n!}\frac{d^n}{d\lambda^n} G_i\left(\sum_{j=0}^{\infty} \lambda^j \underline{u}_j\right)\Bigg|_{\lambda=0},$$

$$\overline{A}_{i,n} = \frac{1}{n!}\frac{d^n}{d\lambda^n} G_i\left(\sum_{j=0}^{\infty} \lambda^j \overline{u}_j\right)\Bigg|_{\lambda=0}.$$

Their arguments (s,t,r) are suppressed when unambiguous. The three transformed contributions for the lower endpoint are

$$\underline{S}_{1,n}(p,q,r) = \mathcal{S}_2\left[\int_a^b k_1(s,t,x)\underline{A}_{1,n}(x,t,r)\,dx\right](p,q),$$

$$\underline{S}_{2,n}(p,q,r) = \mathcal{S}_2\left[\int_c^t k_2(s,t,y)\underline{A}_{2,n}(s,y,r)\,dy\right](p,q),$$

$$\underline{S}_{3,n}(p,q,r) = \mathcal{S}_2\left[\int_c^t \int_a^b k_3(s,t,x,y)\underline{A}_{3,n}(x,y,r)\,dx\,dy\right](p,q).$$

For the upper endpoint, similarly,

$$\overline{S}_{1,n}(p,q,r) = \mathcal{S}_2\left[\int_a^b k_1(s,t,x)\overline{A}_{1,n}(x,t,r)\,dx\right](p,q),$$
$$\overline{S}_{2,n}(p,q,r) = \mathcal{S}_2\left[\int_c^t k_2(s,t,y)\overline{A}_{2,n}(s,y,r)\,dy\right](p,q),$$
$$\overline{S}_{3,n}(p,q,r) = \mathcal{S}_2\left[\int_c^t \int_a^b k_3(s,t,x,y)\overline{A}_{3,n}(x,y,r)\,dx\,dy\right](p,q).$$

Therefore, the transformed and inverse-transform recurrence relations are

$$\underline{U}_{n+1} = \underline{S}_{1,n} + \underline{S}_{2,n} + \underline{S}_{3,n}, \qquad \underline{u}_{n+1} = \mathcal{S}_2^{-1}\left[\underline{U}_{n+1}\right],$$
$$\overline{U}_{n+1} = \overline{S}_{1,n} + \overline{S}_{2,n} + \overline{S}_{3,n}, \qquad \overline{u}_{n+1} = \mathcal{S}_2^{-1}\left[\overline{U}_{n+1}\right].$$

All equalities involving $\mathcal{S}_2^{-1}$ are understood after the domain convention in Section 3.1. In particular, inversion recovers the three original integral contributions; no general product or convolution rule is being assumed for the mixed kernels.
Using the recurrence relations above, the first two correction terms for each endpoint are

$$\underline{u}_1 = \mathcal{S}_2^{-1}\left[\underline{S}_{1,0} + \underline{S}_{2,0} + \underline{S}_{3,0}\right], \qquad \overline{u}_1 = \mathcal{S}_2^{-1}\left[\overline{S}_{1,0} + \overline{S}_{2,0} + \overline{S}_{3,0}\right],$$
$$\underline{u}_2 = \mathcal{S}_2^{-1}\left[\underline{S}_{1,1} + \underline{S}_{2,1} + \underline{S}_{3,1}\right], \qquad \overline{u}_2 = \mathcal{S}_2^{-1}\left[\overline{S}_{1,1} + \overline{S}_{2,1} + \overline{S}_{3,1}\right].$$

The Nth partial-sum approximation is written as the endpoint pair

$$u^{(N)}(s,t,r) = \left(\sum_{n=0}^{N} \underline{u}_n(s,t,r),\ \sum_{n=0}^{N} \overline{u}_n(s,t,r)\right).$$

4. Existence, Uniqueness, and Convergence Analysis

Let $A = [a,b] \times [c,d]$, let E^1 denote the space of fuzzy numbers equipped with complete metric D, and define $X = C(A, E^1)$, with $D^*(u,v) = \sup_{(s,t)\in A} D\big(u(s,t), v(s,t)\big)$.
Here, $T: X \to X$ represents the integral operator associated with equation (1).

Theorem 1 (Existence and Uniqueness). *Assume $g \in X$, the kernels k_i are continuous, nonnegative, and bounded by M_i, and the operators $G_i: E^1 \to E^1$ satisfy Lipschitz conditions with constants L_i ($i = 1,2,3$). If $q = M_1L_1(b-a) + M_2L_2(d-c) + M_3L_3(b-a)(d-c) < 1$, then the two-dimensional nonlinear fuzzy Volterra–Fredholm integral equation has a unique solution in X.*

Proof. The continuity assumptions ensure that T maps X into itself. Using the Lipschitz conditions, the bounds on the nonnegative kernels, and the standard fuzzy integral metric inequality, we obtain

$D^*(Tu, Tv) \leq qD^*(u, v), \qquad u, v \in X.$

Since $q < 1$, T is a contraction on the complete metric space X. Banach's fixed-point theorem therefore yields a unique fixed point $u^* \in X$, which is the required solution. □

Theorem 2 (Convergence of MSADM). *Under the assumptions of Theorem 1, suppose that the MSADM partial sums* $s_m = \sum_{i=0}^{m} u_i$ *belong to* X *and, for some* $0 \leq \rho < 1$, *satisfy* $D^*(s_{n+1}, s_n) \leq \rho^n D^*(s_1, s_0), n \geq 0$. *Assume also that the MSADM approximations are asymptotically consistent with the integral equation:* $\lim_{m\to\infty} D^*(s_m, Ts_m) = 0$. *Then the MSADM partial sums converge uniformly in the fuzzy metric to the unique solution* u^*.

Proof. For $n > m$, the triangle inequality gives

$$\begin{aligned} D^*(s_n, s_m) &\leq \sum_{j=m}^{n-1} D^*\left(s_{j+1}, s_j\right) \\ &\leq \sum_{j=m}^{n-1} \rho^j D^*(s_1, s_0) \\ &\leq \frac{\rho^m}{1-\rho} D^*(s_1, s_0) \to 0 \qquad (m \to \infty). \end{aligned}$$

Thus (s_m) is Cauchy in the complete space X and converges to some $s \in X$. As T is Lipschitz continuous,
$D^*(s, Ts) \leq D^*(s, s_m) + D^*(s_m, Ts_m) + D^*(Ts_m, Ts) \to 0.$

Therefore $s = Ts$, and uniqueness in Theorem 1 implies $s = u^*$. □

Theorem 3 (Truncation Error Estimate of MSADM). *Under the assumptions of Theorem 2, the truncation error of the MSADM approximation* s_m *satisfies* $D^*(u^*, s_m) \leq \frac{\rho^m}{1-\rho} D^*(s_1, s_0)$.

Proof. For $n > m$, Theorem 2 gives
$D^*(s_n, s_m) \leq \frac{\rho^m}{1-\rho} D^*(s_1, s_0).$

Taking $n \to \infty$ and using $s_n \to u^*$ yields the claimed bound. Because $0 \leq \rho < 1$, the upper bound tends to zero as $m \to \infty$.

Example. Consider equation fuzzy Volterra–Fredholm in $A = [0,1] \times [0,1]$:

$$u(s,t) = g(s,t) \oplus (FR)\int_0^t (FR)\int_0^1 k\,(s,t,x,y) \odot u^2(x,y)\,dx\,dy$$
$$k(s,t,x,y) = stxy, r \in [0,1]$$
$$g(s,t;r) = \left(st(2+r) - \frac{1}{16}st^5(2+r)^2,\ st(4-r) - \frac{1}{16}st^5(4-r)^2\right)$$
$$u_{\text{exact}}(s,t;r) = \left(st(2+r),\ st(4-r)\right)$$

Applying the double Sumudu transform to the parametric form of the integral equation and using the Adomian decomposition, the successive approximations are obtained through the recurrence relations defined in Section 3. The inverse double Sumudu transform is then applied to recover the approximate solutions in the original domain. Table 1 presents the numerical approximations and corresponding absolute errors at (s=0.2), (t=0.7), and (r=0.5). The first two approximation terms are obtained as follows:

$$\underline{u}_0(s,t,r) = (2+r)st - \frac{(2+r)^2}{16}st^5,$$

$$\overline{u}_0(s,t,r) = (4-r)st - \frac{(4-r)^2}{16}st^5,$$

$$\underline{u}_1(s,t,r) = st\left[\frac{(2+r)^2t^4}{16} - \frac{(2+r)^3t^8}{256} + \frac{(2+r)^4t^{12}}{12288}\right],$$

$$\overline{u}_1(s,t,r) = st\left[\frac{(4-r)^2t^4}{16} - \frac{(4-r)^3t^8}{256} + \frac{(4-r)^4t^{12}}{12288}\right].$$

The first-order MSADM approximation is therefore given by

$$u^{(1)}(s,t,r) = \left[\underline{u}_0(s,t,r) + \underline{u}_1(s,t,r), \overline{u}_0(s,t,r) + \overline{u}_1(s,t,r)\right].$$

Table 1. Comparison of the approximate solutions with the exact solution and absolute errors at s = 0.2, t = 0.7, and r = 0.5.

Iteration (m)	Lower approximation	Upper approximation	Lower absolute error	Upper absolute error
0	0.33686953	0.46426428	0.01313047	0.02573572
1	0.34951356	0.48867198	0.00048644	0.00132802
2	0.34998198	0.48993147	0.00001802	0.00006853
3	0.34999933	0.48999646	0.00000067	0.00000354
Exact solution	0.35000000	0.49000000	0.00000000	0.00000000

Acknowledgements
We would like to thank the University of Tirana and the University of Prishtina for their support.

References

Abbasbandy, S., & Allahviranloo, T. (2006). The Adomian decomposition method applied to the fuzzy system of Fredholm integral equations of the second kind. International Journal of Uncertainty, Fuzziness and Knowledge-Based Systems, 14(1), 101–110. https://doi.org/10.1142/S0218488506003868

Abdul Rahman, N. A., & Ahmad, M. Z. (2017a). Solving fuzzy fractional differential equations using fuzzy Sumudu transform. Journal of Nonlinear Sciences and Applications, 10(5), 2620–2632. https://doi.org/10.22436/jnsa.010.05.28

Abdul Rahman, N. A., & Ahmad, M. Z. (2017b). Solving fuzzy Volterra integral equations via fuzzy Sumudu transform. Applied Mathematics and Computational Intelligence, 6, 19–28.

Adomian, G. (1988). A review of the decomposition method in applied mathematics. Journal of Mathematical Analysis and Applications, 135, 501–544.

Adomian, G. (1994). Solving frontier problems of physics: The decomposition method. Kluwer Academic Publishers.

Al-Khaled, K., & Yousef, M. H. (2019). Sumudu decomposition method for solving higher-order nonlinear Volterra–Fredholm fractional integro-differential equations. Nonlinear Dynamics and Systems Theory, 19(3), 348–361.

Alidema, A. (2022). Applications of double fuzzy Sumudu Adomian decomposition method for two-dimensional fuzzy Volterra integral equations. European Journal of Pure and Applied Mathematics, 15(3), 1363–1375.

Alidema, A., & Georgieva, A. (2018). Adomian decomposition method for solving two-dimensional nonlinear Volterra fuzzy integral equations. AIP Conference Proceedings, 2048, 050009.

Alidema, A., & Georgieva, A. (2019). Applications of the double fuzzy Sumudu transform for solving Volterra fuzzy integral equations. AIP Conference Proceedings, 2172, 060006. https://doi.org/10.1063/1.5133534

Amer, Y. A., Mahdy, A. M. S., & Namoos, H. A. R. (2018). Application of Sumudu decomposition method to solve nonlinear system Fredholm and Volterra integro-differential equations. International Journal of Applied Engineering Research, 13(11), 9588–9595.

Babolian, E., Goghary, H. S., & Abbasbandy, S. (2005). Numerical solution of linear Fredholm fuzzy integral equations of the second kind by Adomian method. Applied Mathematics and Computation, 161, 733–744.

Dubois, D., & Prade, H. (1982a). Towards fuzzy differential calculus. Part 1: Integration of fuzzy mappings. Fuzzy Sets and Systems, 8(1), 1–17. https://doi.org/10.1016/0165-0114(82)90025-2

Dubois, D., & Prade, H. (1982b). Towards fuzzy differential calculus. Part 2: Integration on fuzzy intervals. Fuzzy Sets and Systems, 8(2), 105–116.

Dubois, D., & Prade, H. (1982c). Towards fuzzy differential calculus. Part 3: Differentiation. Fuzzy Sets and Systems, 8(3), 225–233. https://doi.org/10.1016/S0165-0114(82)80001-8

El-Kalla, I. L. (2008). Convergence of the Adomian method applied to a class of nonlinear integral equations. Applied Mathematics Letters, 21(4), 372–376. https://doi.org/10.1016/j.aml.2007.05.008

Georgieva, A. (2018). Solving two-dimensional nonlinear Volterra–Fredholm fuzzy integral equations by using Adomian decomposition method. Dynamic Systems and Applications, 27(4), 819–835. https://doi.org/10.12732/dsa.v27i4.9

Georgieva, A., & Alidema, A. (2019). Convergence of homotopy perturbation method for solving of two-dimensional fuzzy Volterra functional integral equations. In Advanced computing in industrial mathematics (Studies in Computational Intelligence, Vol. 793, pp. 129–145). Springer. https://doi.org/10.1007/978-3-319-97277-0_11

Goetschel, R., & Voxman, W. (1986). Elementary fuzzy calculus. Fuzzy Sets and Systems, 18, 31–43.

Jafari, R., & Razvarz, S. (2018). Solution of fuzzy differential equations using fuzzy Sumudu transforms. Mathematical and Computational Applications, 23, Article 5.

Kaleva, O. (1987). Fuzzy differential equations. Fuzzy Sets and Systems, 24, 301–317.

Mordeson, J., & Newman, W. (1995). Fuzzy integral equations. Information Sciences, 87, 215–229.

Seikkala, S. (1987). On the fuzzy initial value problem. Fuzzy Sets and Systems, 24, 319–330.

Wu, C., & Gong, Z. (2001). On Henstock integral of fuzzy-number-valued functions (I). Fuzzy Sets and Systems, 120, 523–532.

Wu, C., & Wu, C. (1997). The supremum and infimum of the set of fuzzy numbers and its applications. Journal of Mathematical Analysis and Applications, 210, 499–511.

Genetic Algorithm and Particle Swarm Optimization for Mass Minimization of a Composite Cylindrical Skirt under Buckling and Strength Constraints

Ekin Oktay*, Halit Süleyman Türkmen

Istanbul Technical University, Faculty of Aeronautics and Astronautics, Department of Aeronautical and Astronautical Engineering, Istanbul, Türkiye
oktaye19@itu.edu.tr

Abstract

A genetic algorithm (GA) and particle swarm optimization (PSO) minimize the mass of a composite cylindrical skirt under buckling and strength constraints. A MATLAB model combines Classical Lamination Theory (CLT), Tsai–Wu failure and analytical buckling, using the configuration of Liang and Chen (2003). Winding angle and two group thicknesses share common bounds and fitness. Thirty runs per method yield mean masses of 5.3727 and 5.2396 kg, with sample standard deviations of 0.0914 and 0.0015 kg. PSO reduces mean mass by 2.48%; mean runtime rises from 10.07 to 17.52 s. These findings are conditional on the archived model; axial scaling and physical validation remain unresolved.

Keywords: Composite cylindrical skirt; genetic algorithm; particle swarm optimization; buckling; CLT; Tsai–Wu criterion

1. Introduction

Fiber orientation and thickness tailor composite stiffness and strength, creating a nonlinear design space. GA (Holland, 1975; Goldberg, 1989) and PSO (Kennedy & Eberhart, 1995) offer derivative-free searches for composite optimization (Le Riche & Haftka, 1993; Suresh et al., 2007; Fakoor et al., 2017). Using Liang and Chen's (2003) skirt configuration, thirty runs compare GA and PSO with common bounds, structural routines and fitness. The published design provides a descriptive benchmark; physical model agreement has not been established.

2. Problem Definition

2.1. Geometry and Loading

The cylindrical skirt has length $L = 0.5$ m and mid-surface radius $R = 0.3$ m, with axial compression $F = 70$ kN and torque $T = 70$ kN·m (Liang & Chen, 2003).

The symmetric architecture has outer $0°/90°$ groups of total thickness h_c and inner $\pm\theta$ groups of total thickness h_θ, with $h_{total} = h_c + h_\theta$.

2.2. Material Properties

Both groups use UD carbon/epoxy, $\rho = 1600$ kg/m³ (Tables 1–2). X/Y indicate longitudinal/transverse strengths, T/C tension/compression, and S in-plane shear strength.

Table 1. Elastic properties of UD carbon/epoxy

E_1 (MPa)	E_2 (MPa)	G_{12} (MPa)	ν_{12}
137000	8170	4750	0.316

* *Corresponding Author*

Table 2. Strengths of UD carbon/epoxy

X_T (MPa)	Y_T (MPa)	X_C (MPa)	Y_C (MPa)	S (MPa)
1470.0	39.2	980.0	78.4	78.4

2.3. Design Variables, Objective and Constraints

The design vector is $X = [\theta, h_c, h_\theta]$, with $1° \leq \theta \leq 89°$ and 0.1–15 mm for each thickness. The mass objective is

$$Minimize\ M = 2\pi\rho RLh_{total} \tag{1}$$

Lengths in Eq. (1) are in metres and density is in kg/m³, giving mass in kilograms. Feasibility requires

$$FI_{max} \leq 1, \quad \lambda \geq 1, \quad h_{total} \leq h_{max} = R/10 \tag{2}$$

Here λ is the combined buckling factor. The 30 mm limit is redundant under the two 15 mm bounds: equality occurs only at their common upper corner. Both methods minimize

$$f_s(X) = \begin{cases} M_{kg} - 0.01\, b_s, & feasible \\ M_{kg} + 10^6 + 10^4 P(X), & otherwise \end{cases} \tag{3}$$

Here M_{kg} is the mass from Eq. (1) in kilograms, and the squared violation penalty is

$$P(X) = [max(0, FI_{max} - 1)]^2 + [max(0, 1 - \lambda)]^2 + [max(0, \frac{h_{total} - h_{max}}{h_{max}})]^2 \tag{4}$$

Both methods use $b_s = \lambda$ and $h_{max} = 30$ mm; the thickness guard is retained.

3. Analysis and Optimization Method

3.1. Structural Analysis

With $B = 0$ by symmetry, $N = [-\frac{F}{2\pi R}, 0, \frac{T}{2\pi R^2}]^T$. Let $\bar{Q}(\varphi)$ denote transformed lamina stiffness. The group matrices are

$$\bar{Q}_c = \bar{Q}(0°) + \bar{Q}(90°), \quad \bar{Q}_\theta = \frac{\bar{Q}(\theta) + \bar{Q}(-\theta)}{2} \tag{5}$$

The cross-ply sum follows Appendix A of Liang and Chen (2003) and equals twice the normalized equal-thickness mixture stiffness. Both A and D retain this source-specific convention; ±θ averaging cancels the 16 and 26 terms.

$$A = h_c\bar{Q}_c + h_\theta\bar{Q}_\theta, \quad B = 0$$
$$D = \frac{{h_\theta}^3}{12}\bar{Q}_\theta + \frac{h^3 - {h_\theta}^3}{12}\bar{Q}_c, \quad h = h_c + h_\theta \tag{6}$$
$$\varepsilon^0 = A^{-1}N, \quad {\sigma_{local}}^{(k)} = T^{(k)}\bar{Q}^{(k)}\varepsilon^0 \tag{7}$$

$T^{(k)}$ transforms stresses to material axes. Over $k = 0°, 90°, +\theta, -\theta$, the Tsai–Wu index is

$$FI_{max} = \max_k [F_1\sigma_1 + F_2\sigma_2 + F_{11}{\sigma_1}^2 + F_{22}{\sigma_2}^2 + F_{66}{\tau_{12}}^2 + 2F_{12}\sigma_1\sigma_2] \tag{8}$$

The strength coefficients are

$$F_1 = \frac{1}{X_T} - \frac{1}{X_C}, \quad F_2 = \frac{1}{Y_T} - \frac{1}{Y_C}$$
$$F_{11} = \frac{1}{X_T X_C}, \quad F_{22} = \frac{1}{Y_T Y_C}, \quad F_{66} = \frac{1}{S^2}, \quad F_{12} = -0.5\sqrt{F_{11}F_{22}}$$

For the simply supported shell, $\alpha = \frac{m\pi}{L}$, $\beta = \frac{n}{R}$; C is symmetric and C_2 its upper-left 2 × 2 block:

$$C_{11} = A_{11}\alpha^2 + A_{66}\beta^2, \quad C_{22} = A_{22}\beta^2 + A_{66}\alpha^2$$
$$C_{12} = (A_{12} + A_{66})\alpha\beta, \quad C_{13} = \frac{A_{12}\alpha}{R}, \quad C_{23} = \frac{A_{22}\beta}{R}$$
$$C_{33} = D_{11}\alpha^4 + 2(D_{12} + 2D_{66})\alpha^2\beta^2 + D_{22}\beta^4 + \frac{A_{22}}{R^2}$$

In SI units, the axial kernel minimizes positive values over $1 \le m \le 20$ and $0 \le n \le 20$:

$$\lambda_a{}^{code} = \min_{m,n}\left[\frac{2R}{\pi F}\left(\frac{L}{\alpha}\right)^2 \frac{det\ C}{det\ C_2}\right] \tag{9}$$

The reference's Eq. (11) uses $\left(\frac{L}{m}\right)^2$ in this prefactor. The archived difference remains explicit and requires verification. Torsional buckling and the combined interaction rule are

$$\lambda_T = \frac{21.75}{T} D_{22}{}^{5/8}\left(\frac{A_{11}A_{22} - A_{12}{}^2}{A_{22}}\right)^{3/8} \frac{R^{5/4}}{L^{1/2}}, \quad \lambda = \left(\frac{1}{\lambda_a{}^{code}} + \frac{1}{\lambda_T}\right)^{-1} \tag{10}$$

The torsional approximation follows the reference's Eq. (15). The archived model has not been independently validated.

3.2. Genetic Algorithm

GA initializes 100 real-valued chromosomes uniformly. Fitness in Eq. (3) ranks candidates; 10 elites survive. Three-candidate tournaments select parents, and arithmetic crossover creates 90 offspring as random convex parent combinations.

Mutation acts independently on thicknesses and angle, each with probability 0.1. Perturbations are uniform within ±2.5 mm per thickness and ±15° for the angle; offspring are clipped to bounds.

3.3. Particle Swarm Optimization

PSO uses 100 uniformly sampled particles with zero initial velocities. Personal best p_i and swarm best g are updated when fitness improves (Kennedy & Eberhart, 1995). Updates in dimension d are

$$v_{i,d}^{t+1} = w^t v_{i,d}^t + c_1 r_{1,d}(p_{i,d} - x_{i,d}^t) + c_2 r_{2,d}(g_d - x_{i,d}^t) \tag{11}$$
$$x_{i,d}^{t+1} = x_{i,d}^t + v_{i,d}^{t+1} \tag{12}$$

The two random values are independent and uniform on [0, 1]; $c_1 = c_2 = 1.5$. Inertia decreases linearly as

$$w^t = w_{max} - (w_{max} - w_{min})\frac{t}{t_{max}} \tag{13}$$

Here $w_{max} = 0.9$, $w_{min} = 0.4$ and $t_{max} = 200$. Velocity is limited to 10% of each bound range. Positions crossing a bound are clipped, with velocity reversed and multiplied by 0.5.

3.4. Termination Criteria

Both methods stop at 200 evaluated populations or 25 consecutive steps without a best-fitness improvement exceeding 0.001. Every improvement updates the best design; only improvements above the tolerance reset stagnation.

4. Results and Discussion

4.1. Comparison Over Thirty Runs

One function evaluation comprises one candidate analysis and fitness calculation. GA reevaluates 100 chromosomes, including elites: NFE $= 100G$ for G evaluated populations. Dense histories give 2600–10400 evaluations/run (mean 5533.3; sample SD 2051.6). Sparse PSO histories omit terminal steps, preventing exact counts. The thirty-run experiment uses common stopping rules, without a fixed evaluation budget.

Table 3. Final mass and runtime over 30 runs per algorithm

Metric	GA	PSO
Minimum mass (kg)	5.2578	5.2378
Mean mass (kg)	5.3727	5.2396
Median mass (kg)	5.3594	5.2393
Mass standard deviation (kg)	0.0914	0.0015
Maximum mass (kg)	5.6893	5.2449
Mean elapsed time (s)	10.07	17.52
Time standard deviation (s)	3.72	3.90

PSO reduces mean mass by 2.48% and sample variability by a factor of approximately 62; its heaviest result is lighter than the lightest GA result. The best-mass difference is 0.38%, while PSO's mean runtime is 74.0% longer. Timings include implementation overhead and console output.

4.2. Lightest Recorded Designs and Buckling Constraints

Table 4 compares GA run 4 and PSO run 15 with the published geometry. PSO reaches $h_{total} = 3.4734$ mm and $\lambda = 1.000004$. Re-evaluation reproduces all sixty archived combined factors within 2×10^{-15}; all satisfy $\lambda \geq 1$.

Table 4. Lightest recorded designs and the literature benchmark

Quantity	GA Run 4	PSO Run 15	Liang and Chen (2003)
Winding angle θ (°)	43.67	43.61	42.50
Cross-ply thickness h_c (mm)	1.2163	1.4781	1.877
Angle-ply thickness h_θ (mm)	2.2704	1.9953	1.807
Total thickness (mm)	3.4867	3.4734	3.684
Mass from Eq. (1) (kg)	5.2578	5.2378	5.5553
Axial buckling factor	1.2046	1.1814	1.1778
Torsional buckling factor	5.9853	6.5140	6.6951
Combined buckling factor λ	1.002757	1.000004	1.0016
FI_{max} (postprocessed)	0.090923	0.100593	0.105866

The reference reports 5.57 kg; Eq. (1) gives 5.5553 kg with $\rho = 1600$ kg/m³ and $h = 3.684$ mm, a 0.263% difference not assigned to rounding. Table 4 uses Eq. (1) masses and literature-reported benchmark buckling factors. FI_{max} is recomputed from saved geometries with the supplied routine, not archived callback outputs; the source's strength factor of 0.00030 is not reproduced. No physical improvement over the benchmark is claimed.

4.3. Convergence and Distribution of Final Designs

Figure 1 shows median best-fitness mass and interquartile ranges. Missing PSO values are forward-filled and terminal values extended to 104 steps for plotting only, adding no evaluations. Stopping steps remain unknown. The buckling reward permits slight mass increases despite improving fitness.

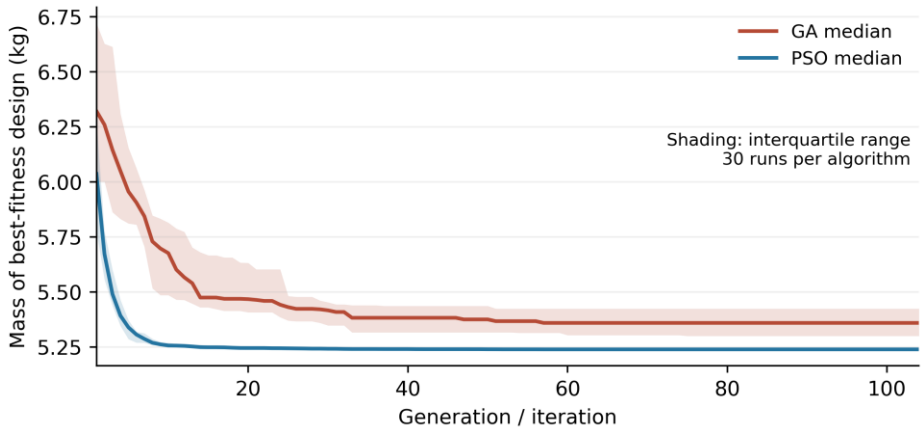


Figure 1. Median best-fitness mass and interquartile range over 30 runs; missing and terminal values are carried forward

PSO enters the final mass region earlier in the recorded histories. Figure 2 shows mass and runtime; evaluation efficiency cannot be inferred.

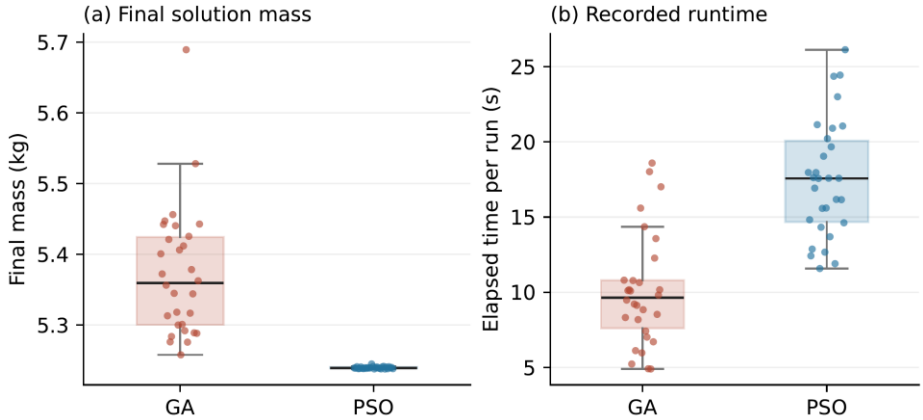


Figure 2. Final mass (a) and elapsed time (b): individual runs, median lines and interquartile boxes

Figure 3 shows PSO angles of 42.52–45.71° and h_{total} of 3.4734–3.4781 mm, compared with GA's 43.00–45.12° and 3.4867–3.7729 mm. Thickness allocations compensate for similar masses; uniqueness and global optimality are not established.

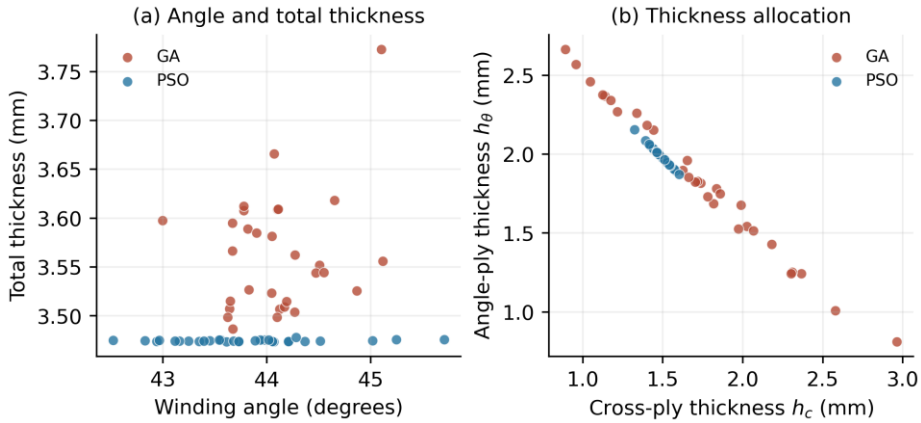


Figure 3. Final angle versus total thickness (a) and cross-ply versus angle-ply thickness (b); 30 runs per algorithm

5. Conclusion

PSO produces lower and more consistent masses over thirty runs under this shared implementation: mean masses are 5.2396 kg for PSO and 5.3727 kg for GA. Its lightest design is 5.2378 kg at 43.61°; GA has a shorter mean runtime. These conditional findings require independent verification of axial scaling and stiffness normalization before physical design conclusions. Future work includes Abaqus comparisons, scaled loads, and archiving seeds, evaluation counts and complete strength and convergence histories.

References

Fakoor, M., Mohammadzade, P., & Jafari, E. (2017). Optimization of composite stiffened cylindrical shell using PSO algorithm. *Journal of Aerospace Science and Technology, 11*(2), 43–51.

Goldberg, D. E. (1989). *Genetic algorithms in search, optimization, and machine learning*. Addison-Wesley.

Holland, J. H. (1975). *Adaptation in natural and artificial systems*. University of Michigan Press.

Kennedy, J., & Eberhart, R. (1995). Particle swarm optimization. In *Proceedings of ICNN'95 – International Conference on Neural Networks* (Vol. 4, pp. 1942–1948). IEEE. https://doi.org/10.1109/ICNN.1995.488968

Le Riche, R., & Haftka, R. T. (1993). Optimization of laminate stacking sequence for buckling load maximization by genetic algorithm. *AIAA Journal, 31*(5), 951–956. https://doi.org/10.2514/3.11710

Liang, C.-C., & Chen, H.-W. (2003). Optimum design of fiber-reinforced composite cylindrical skirts for solid rocket cases subjected to buckling and overstressing constraints. *Composites Part B: Engineering, 34*(3), 273–284. https://doi.org/10.1016/S1359-8368(02)00104-X

Suresh, S., Sujit, P. B., & Rao, A. K. (2007). Particle swarm optimization approach for multi-objective composite box-beam design. *Composite Structures, 81*(4), 598–605. https://doi.org/10.1016/j.compstruct.2006.10.008

Author Index

Artan F. Alidema, 84
Ayse Nur Altunkaya, 41
Çağrı Latifoğlu, 78
Djamil Aissani, 70
Ekin Oktay, 93
Frederik Dara, 84
Halit Süleyman Türkmen, 93
Hanefi Gezer, 34
Ibrahim Kucukkoc, 26
Ioannis D. Sfikas, 14
İbrahim Arık, 34, 63
İlhan Usta, 34, 63
Noumedia Ouarab, 70
Samra Boulfekhar, 70
Seda Ermiş, 56
Selçuk Alp, 20
Selçuk Han Aydın, 49
Sena Şaylıg, 26
Seza Dinibutun, 8
Ulviye Savaş, 20
Vildan Özkır, 20
Yeliz Mert Kantar, 34, 63

4th International Conference on Applied Mathematics in Engineering

September 2-4, 2026 – Cunda Island, Ayvalık-Balikesir, Türkiye

ISBN:
XXX-XXX-XXXXX-X-X

ICAMΣ'26

The 4th International Conference on Applied Mathematics in Engineering

Cunda Island, Ayvalık-Balıkesir, Türkiye